

WALL-MODELED LES OF 3-D TURBULENT BOUNDARY LAYER WITH EMPHASIS ON
GRID INDEPENDENCY

Xiaohan Hu

A DISSERTATION

in

Mechanical Engineering and Applied Mechanics

Presented to the Faculties of the University of Pennsylvania

in

Partial Fulfillment of the Requirements for the

Degree of Doctor of Philosophy

2023

Supervisor of Dissertation

George Ilhwan Park, Assistant Professor of Mechanical Engineering and Applied Mechanics

Graduate Group Chairperson

Prashant Purohit, Professor of Mechanical Engineering and Applied Mechanics

Dissertation Committee

George Ilhwan Park, Assistant Professor of Mechanical Engineering and Applied Mechanics

Howard Hu, Professor of Mechanical Engineering and Applied Mechanics

Paulo Arratia, Professor of Mechanical Engineering and Applied Mechanics

WALL-MODELED LES OF 3-D TURBULENT BOUNDARY LAYER WITH EMPHASIS
ON GRID INDEPENDENCY

COPYRIGHT

2023

Xiaohan Hu

ACKNOWLEDGEMENTS

This work was sponsored by NASA's Transformational Tools and Technologies Project of the Transformative Aeronautics Concepts Program under the Aeronautics Research Mission Directorate (Grant 80NSSC18M0155), and by the Office of Naval Research (ONR) (Grant N000141712310). Computational resources supporting this work were provided by the NASA High-End Computing Program through the NASA Advanced Supercomputing Division at Ames Research Center.

I would like to thank my advisor Prof. George Park for his guidance during my PhD. I can not achieve this without his support. I am the first PhD student in Prof. Park's group. He has always been patient in teaching and advising me to acquire the skills required for a solid research. I would also want to thank my committee members, Prof. Howard Hu and Prof. Paulo Arratia for their meaningful suggestions on my research.

I then want to thank my family for their love and encouragement during my PhD. Five years PhD study and research is a long and tough journey. Their support empowered me to overcome all the difficulties I encountered in life and research. I have not been able to travel back to see them during the last few years due to the COVID pandemic. I hope to meet with them in the near future and share with them my happiness of accomplishing this milestone in my life.

Lastly, my thank you would be given to my friends at UPENN and all the group members in Park Lab. I'm really grateful to study and work with them during the last few years. This kind and friendly environment makes me really enjoy the life at Philly and UPENN. I would keep all these moments in my memory.

ABSTRACT

WALL-MODELED LES OF 3-D TURBULENT BOUNDARY LAYER WITH EMPHASIS ON GRID INDEPENDENCY

Xiaohan Hu

George Ilhwan Park

While wall-modeled large-eddy simulation (WMLES) has become an indispensable numerical tool for scale-resolving simulations and shows its superiority compared to other computational fluid dynamics tools in high Reynolds-number wall-bounded turbulent flows, there are still several challenges remaining to be resolved. The first challenge is the assessment of wall models' capabilities in nonequilibrium turbulent boundary layers with pressure gradient and mean-flow three-dimensionality. WMLES of a pressure-driven three-dimensional turbulent boundary layer (3DTBL) developing on the floor of a bent square duct is conducted to investigate the predictive capabilities of three widely used wall models, namely, a simple equilibrium stress model, an integral nonequilibrium model, and a PDE nonequilibrium model. While the wall-stress magnitudes predicted by the three wall models are comparable, the PDE nonequilibrium wall model produces a substantially more accurate prediction of the wall-stress direction. The wall-stress direction from the wall models is shown to have separable contributions from the equilibrium stress part and the integrated nonequilibrium effects, where how the latter is modeled differs among the wall models. Another challenge is to demonstrate the invariance of the WMLES results with respect to the mesh resolution. It is proposed that the extent of the wall-modeled region controls the convergence trajectory. Specifically, the onset of convergence is expected to occur at coarser grid resolutions when larger extents of the wall-modeled region are employed. The proposition is examined in both channel flow and a 3DTBL. The obtained results provide compelling evidence supporting the idea. Lastly, why dynamic model in LES works is still not well understood. In the present work, it is postulated that the principal directions of the resolved rate-of-strain tensor play an important role in the dynamic model. Specifically, it is found that minimization of the GIE along only the three principal directions, in lieu of its nine components

in its original formulation, produces equally comparable results as the original model, suggesting that there might be dynamically more important directions for modeling the subgrid dynamics.

TABLE OF CONTENTS

ACKNOWLEDGEMENTS	iii
ABSTRACT	iv
LIST OF TABLES	viii
LIST OF ILLUSTRATIONS	ix
CHAPTER 1 : INTRODUCTION	1
1.1 Motivation and background	1
1.2 Literature review	4
1.2.1 Wall-modeled large-eddy simulation	4
1.2.2 Three dimensional turbulent boundary layer	8
1.2.3 Grid convergence	11
1.2.4 Dynamic modeling	14
1.3 Accomplishments	15
CHAPTER 2 : WMLES OF A 3DTBL IN A BENT SQUARE DUCT	17
2.1 Flow configuration	17
2.2 Inflow characterization and boundary conditions	20
2.3 Flow solver and subgrid scale (SGS) / near-wall modeling	22
2.4 Flow statistics	26
2.4.1 Grid convergence	27
2.4.2 Instantaneous flow field	28
2.4.3 Mean-flow statistics	30
2.4.4 Reynolds stress	35
2.5 Lumley triangle: anisotropy invariant map	39
2.6 Triangular plot	41

2.7	Quantification of the nonequilibrium contributions to the wall shear stress direction	43
2.8	Effects of the SGS modeling	49
2.9	Effects of the matching height	51
2.10	Modifications to the original integral NEQWM	53
CHAPTER 3 : ON THE GRID CONVERGENCE OF WALL-MODELED LARGE-EDDY		
	SIMULATION	56
3.1	Convergence in WMLES: Background	56
3.2	A proposition on the grid convergence in WMLES	59
3.3	Numerical details and wall modeling	62
3.4	Flow configuration	63
3.5	Results and discussion	64
	3.5.1 Grid convergence of skin friction	64
	3.5.2 Grid convergence of mean velocity and Reynolds stress	66
CHAPTER 4 : A HIDDEN MECHANISM OF DYNAMIC LES MODELS		75
4.1	Reduction of dynamic procedures along the principal directions of \bar{S}_{ij}	75
4.2	Flow configuration	77
4.3	Results and discussion	78
	4.3.1 Turbulent channel flow at $Re_\tau = 395$ and $Re_\tau = 1000$	78
	4.3.2 Three-dimensional turbulent boundary layer	82
	4.3.3 Flow over periodic hills	83
4.4	Application to dynamic tensor coefficient Smagorinsky model	84
CHAPTER 5 : CONCLUSION		87
APPENDIX A : DERIVATION FOR SWH FORMULA		92
BIBLIOGRAPHY		94

LIST OF TABLES

TABLE 1.1 List of papers with the comparison of different wall models. Numbers in the parentheses in the last column in the form of (C, d) denote the number of non-zero mean velocity components (C) in (U, V, W) and the number of spatial dimensions (d) they depend upon. **It should be noted that the flow considered in the present study corresponds to $(C, d) = (3, 3)$, where all mean velocity components are non zero, they vary in all spatial coordinates, without any direction of periodicity/homogeneity.** 9

TABLE 3.1 Isotropic grid resolutions (in wall units) and the matching heights used in the WMLES of the turbulent channel flow at $Re_\tau = 1000$ 64

LIST OF ILLUSTRATIONS

FIGURE 1.1	Sketch of the wall-stress modeling procedure (reproduction from figure 1 of Park and Moin (2016a)). Wall shear stress (τ_w) and heat flux (q_w) are solved from the wall model equations on a separate near-wall mesh. Wall models are driven by the LES states imposed at their top boundaries while the no-slip condition is applied at the wall.	5
FIGURE 2.1	A Schematic of the floor of the duct with a 30° bend (reproduction from figure 1 of Schwarz and Bradshaw (1994)). The measurement locations in the experiment are marked as numbers 0-21 along the duct centerline. Two coordinate systems are employed. (x, y, z) is a fixed coordinate system with the origin located at the inlet. (x', y', z') is a curvilinear coordinate system aligned with the local duct centerline (measurements in mm).	18
FIGURE 2.2	(a) Near-wall grid spacing distributions in wall units (based on the local skin friction) along the duct centerline. (b) Near-wall grid spacing distributions (normalized by duct height D) along the duct centerline. Solid lines, wall-parallel grid spacing ($\Delta x = \Delta z$); dashed lines, wall-normal grid spacing (Δy). Black, coarse mesh; blue, fine mesh.	19
FIGURE 2.3	Centerline distributions of (a) boundary layer thickness and (b) momentum thickness (coarse mesh). Symbols, experiment; red dash-dotted line, equilibrium wall model; blue solid line, PDE nonequilibrium wall model; green dashed line, integral nonequilibrium wall model. Black vertical dashed lines denote the start and end of the bend region.	21
FIGURE 2.4	(a) Mean velocity profile at the first measurement station in the experiment (station 0: $x' = 826$ mm). Black squares are from the experiment. Black dots, WRLES by Schlatter et al. (2010) at the same Reynolds number ($Re_\theta = 4100$); red, equilibrium wall model; blue, PDE nonequilibrium wall model; green, integral nonequilibrium wall model (solid lines represent coarse mesh results; dashed lines represent fine mesh results). Black dashed lines denote the law of the wall (viscous sublayer: $u^+ = y^+$; log-law: $u^+ = \frac{1}{0.41} \log y^+ + 5.2$). (b) Reynolds stress profiles at the first measurement location (station 0: $x' = 826$ mm). Big symbols are from the experiment : circles, $\overline{u'u'}$; stars, $\overline{v'v'}$; triangles, $\overline{w'w'}$; squares, $\overline{u'v'}$. Different lines and dots have the same denotations as in (a).	22
FIGURE 2.5	Grid convergence of the EQWM LES. (a) Blue, mean-flow direction vs. distance from the wall; red, mean velocity magnitude profile, (b) Centerline distribution of the skin-friction coefficient, and (c) Reynolds-stress profiles. Red, $\overline{u'u'}$; blue, $-\overline{u'v'}$; green, $\overline{v'w'}$. Solid lines, coarse grid; dashed line, fine grid. Profiles in (a) and (c) are at $x' = 1875$ mm (station 8). Black vertical dashed lines in (b) denote the start and end of the bend region.	27

FIGURE 2.6	Visualization of the near-wall vortical structures using the isosurfaces of Q ($Q = Q_{rms}$, where Q is the second invariant of the velocity gradient tensor), colored by the distance from the floor of the duct. Flow is from the bottom left to the top right. Surface oil visualization from the experiment (Schwarz and Bradshaw, 1994) is shown in the inset (figure reprinted with permission from Schwarz and Bradshaw (1994)).	29
FIGURE 2.7	Variation of the wall-pressure coefficient from coarse EQWM simulation (results from the other wall models and resolutions are almost identical). Symbols are from the experiment. Colors denote different spanwise locations corresponding to the inset figure. $z' : 0 \text{ mm}, \pm 127 \text{ mm}, \pm 254 \text{ mm}, \pm 368 \text{ mm}$	30
FIGURE 2.8	Centerline distribution of the skin-friction coefficient (C_f). (a) C_f vs. Re_θ upstream of the bend. (b) C_f vs. axial location. Squares, experiment; red dash-dotted line, EQWM; blue solid line, PDE NEQWM; green dashed line, integral NEQWM. In (a): Black dotted line, ZPGFPBL empirical correlation (Eq. (9) in Fernholz and Finley (1996)); black dashed line, WRLES of ZPGFPBL (Eitel-Amor et al., 2014).	32
FIGURE 2.9	(a) Centerline distribution of the surface flow turning angles with respect to the freestream ($\gamma_w = \tan^{-1}(\tau_{w,z}/\tau_{w,x})$ is the wall shear stress direction, $\gamma_\infty = \tan^{-1}(W_e/U_e)$ is the freestream direction). (b) streamlines of wall shear stress. Squares, experiment; red line, equilibrium wall model; blue line, PDE nonequilibrium wall model; green line, integral nonequilibrium wall model. Solid and dashed lines are for coarse and fine grids, respectively.	33
FIGURE 2.10	Profiles of the mean-velocity magnitude at 5 measurement locations (stations 4, 8, 12, 16, and 20, from left to right). Station 4 is upstream of the bend; station 8 is within the bend; stations 12, 16 and 20 are downstream of the bend. Red dash-dotted line, EQWM; blue solid line, PDE NEQWM; green dashed line, integral NEQWM; magenta dotted line, no-slip LES; black circle, experiment. Profiles are shifted along the abscissa by 1.	34
FIGURE 2.11	Mean-flow direction relative to the local freestream as a function of wall distance. Red dash-dotted line, EQWM; blue solid line, PDE NEQWM; green dashed line, integral NEQWM; magenta dotted line, no-slip LES; black solid line, experiment. Symbols are used to differentiate stations along the duct floor centerline only (Square, station 0; triangle, station 6; diamond, station 10). Lines with the same symbols denote the results at the same stations.	35
FIGURE 2.12	Reynolds normal stress profiles at the same five measurement stations as the mean velocity profiles in Fig. 2.10. Red dash-dotted line, EQWM; blue solid line, PDE NEQWM; green dashed line, integral NEQWM; magenta dotted line, no-slip LES; black circle, experiment. Profiles are shifted along the abscissa by multiples of 10, 2 and 4 for $\overline{u'u'}$, $\overline{v'v'}$ and $\overline{w'w'}$, respectively.	37
FIGURE 2.13	Reynolds shear stress profiles at the same five locations as the mean velocity profiles in Fig. 2.10. Red dash-dotted line, EQWM; blue solid line, PDE NEQWM; green dashed line, integral NEQWM; magenta dotted line, no-slip LES; black circle, experiment. Profiles are shifted along the abscissa by multiples of 1.5, 2 and 1 for $-\overline{u'v'}$, $-\overline{u'w'}$ and $\overline{v'w'}$, respectively.	38

FIGURE 2.14	Directions (relative to the local freestream) of the mean velocity gradient vector and the Reynolds shear stress vector. (a) station 10; (b) station 17. Red, EQWM; blue, PDE NEQWM; green, integral NEQWM; black, experiment. Circle, angle between the Reynolds shear stress vector γ_τ and the local freestream; cross, angle between the mean velocity gradient vector γ_g and the local freestream.	39
FIGURE 2.15	Lumley triangle of the WMLES results along the wall-normal direction. (a) station 4. (b) station 10. (c) station 12. (d) station 18. Colored dots, fine grid PDE NEQWM result (all the wall models give almost identical results, and thus only PDE-NEQWM is shown here); black dash-dotted line, canonical 2D channel flow at $Re_\tau = 2003$ (Hoyas and Jimenez, 2006); red solid line, shear-driven 3DTBL from transient channel at $Re_\tau = 546$ at $t^+ = 192$ (Lozano-Durán et al., 2020). Colorbar denotes the wall distance normalized by the local boundary layer thickness.	40
FIGURE 2.16	Johnston triangular plot (a) WMLES of the bent square duct (all the wall models give almost identical results, and thus only PDE-NEQWM is shown here): square, station 0; circle, station 4; triangle, station 6; cross, station 8; diamond, station 10; star, station 12. (b) DNS of the shear-driven 3DTBL from the transient channel flow at $Re_\tau = 546$ at $t^+ = 192$ (Lozano-Durán et al., 2020). Red straight line, the SWH formula Eq. (2.16). Colorbar denotes the wall distance normalized by the local boundary layer thickness.	42
FIGURE 2.17	Johnston triangular plot of LES and wall-model solutions. (a) Crossflow developing stage: square, station 0; circle, station 4; triangle, station 6; cross, station 8; diamond, station 10; star, station 12. (b) Crossflow decaying stage: square, station 12; circle, station 14; triangle, station 16; cross, station 18; diamond, station 20; star, station 21. Red solid straight line, relation given by the SWH formula (Eq. (2.16)); red dash-dotted line, EQWM; blue solid line, PDE NEQWM; green dashed line, integral NEQWM. Lines with symbols represent the WMLES solution similar to Fig. 2.16(a). Colorbar denotes the wall distance normalized by the local boundary layer thickness.	43
FIGURE 2.18	Centerline distribution of the nonequilibrium contributions (from PDE NEQWM). Red solid line, U_{LES}/U_{ref} ; red dashed line, W_{LES}/U_{ref} ; black solid line, $-I_x/U_{ref}$; black dashed line, $-I_z/U_{ref}$	46
FIGURE 2.19	Centerline distribution of the nonequilibrium contribution to the flow direction. Solid line, I_x/U_{LES} ; dashed line, $-I_z/W_{LES}$; dotted line, total nonequilibrium correction. Blue, NEQWM; green, integral NEQWM. Black vertical dashed lines, start and end of the bend region.	48
FIGURE 2.20	Centerline distribution of the surface flow turning angles with respect to the freestream (γ_w is the wall shear stress direction, γ_∞ is the freestream direction). (a) including all nonequilibrium effects, (b) including diffusion only, (c) including pressure gradient only, (d) including advection only. Red dash-dotted line, EQWM; blue dashed line, PDE NEQWM; blue solid line with circles, reconstruction with nonequilibrium contributions; black squares, experiment; black vertical dashed line, start and end of the bend region.	50

FIGURE 2.21	(a) Centerline distribution of the surface flow turning angles with respect to the freestream ($\gamma_w = \tan^{-1}(\tau_{w,z}/\tau_{w,x})$ is the wall shear stress direction, $\gamma_\infty = \tan^{-1}(W_e/U_e)$ is the freestream direction). Squares, experiment; red solid line, EQWM with Vreman model; red dashed line, EQWM with DSM. (b) Mean-flow direction relative to the local freestream as a function of wall distance. Red solid line, EQWM with Vreman model; red dashed line, EQWM with DSM; black solid line, experiment. Symbols are used to differentiate stations along the duct floor centerline only (Square, station 0; triangle, station 6; diamond, station 10). Lines with the same symbols denote the results at the same stations.	51
FIGURE 2.22	(a) Centerline distribution of the surface flow turning angles with respect to the freestream ($\gamma_w = \tan^{-1}(\tau_{w,z}/\tau_{w,x})$ is the wall shear stress direction, $\gamma_\infty = \tan^{-1}(W_e/U_e)$ is the freestream direction). Squares, experiment; red solid line, EQWM with Vreman model; blue dashed line, EQWM with DTCSM. (b) Mean-flow direction relative to the local freestream as a function of wall distance. Red solid line, EQWM with Vreman model; blue dashed line, EQWM with DTCSM; black solid line, experiment. Symbols are used to differentiate stations along the duct floor centerline only (Square, station 0; triangle, station 6; diamond, station 10). Lines with the same symbols denote the results at the same stations.	52
FIGURE 2.23	(a) Centerline distribution of the surface flow turning angles with respect to the freestream ($\gamma_w = \tan^{-1}(\tau_{w,z}/\tau_{w,x})$ is the wall shear stress direction, $\gamma_\infty = \tan^{-1}(W_e/U_e)$ is the freestream direction). Squares, experiment; red line, EQWM; blue line, PDE NEQWM; green line, integral NEQWM. Dashed lines denote calculations run with double the matching height. Solid lines denote the baseline calculations as in Fig. 2.9. (b) Mean-flow direction relative to the local freestream as a function of wall distance. Red solid line, EQWM with the original matching height; red dashed line, EQWM with double the matching height; black solid line, experiment. Symbols are used to differentiate stations along the duct floor centerline only (Square, station 0; triangle, station 6; diamond, station 10). Lines with the same symbols denote the results at the same stations.	54
FIGURE 3.1	A schematic of the grid convergence concept in WMLES. The axes with different colors denote grid spacing in inner viscous scale (blue, Δ^+) or outer scale (red, Δ/δ). Wall modeling is called for when the near-wall grid spacings in LES are large (say, $O(10^2)$ or larger) in viscous wall units. At the same time, convergence of WMLES should be ideally demonstrable with $\Delta/\delta = O(10^{-2}) \sim O(10^{-1})$ before reaching the resolved LES limit. The friction Reynolds number is assumed to be $O(10^4)$ or higher.	57
FIGURE 3.2	A schematic of the grid convergence trend (error vs. grid resolution) for three different wall model matching heights ($h_{wm,1} > h_{wm,2} > h_{wm,3}$) as described in the proposition.	62

FIGURE 3.3	Grid convergence of the skin friction (τ_w) in turbulent channel flow at $Re_\tau = 1000$. (a) Grid spacing is normalized by the half channel height δ ; (b) Grid spacing is normalized by the wall model matching height (h_{wm}). Blue, $h_{wm} = 0.2\delta$; red, $h_{wm} = 0.1\delta$	64
FIGURE 3.4	Grid convergence of the skin friction (τ_w) in 3DTBL. (a) Grid spacing is normalized by the boundary layer thickness δ ; (b) Grid spacing is normalized by the wall model matching height (h_{wm}). Blue, $h_{wm} = 0.15\delta$; black, $h_{wm} = 0.1\delta$; red, $h_{wm} = 0.05\delta$	66
FIGURE 3.5	Mean velocity gradient profile in turbulent channel flow at $Re_\tau = 1000$. The mean velocity gradient is calculated from the mean momentum balance equation. Different colors denote different LES grid resolutions with $h_{wm} = 0.2\delta$ in Table 3.1. The black dashed line denotes DNS result (Li et al., 2008; Perlman et al., 2007). The vertical black dotted line denotes the wall model matching location.	68
FIGURE 3.6	Grid convergence of mean velocity in turbulent channel flow at $Re_\tau = 1000$. (a) Error of mean velocity as a function of the grid resolution normalized by the half channel height δ ; (b) Error of mean velocity as a function of the grid resolution normalized by the matching height h_{wm} . Blue, $h_{wm} = 0.2\delta$; red, $h_{wm} = 0.1\delta$	68
FIGURE 3.7	Grid convergence of rms intensity u_{rms} in turbulent channel flow at $Re_\tau = 1000$. (a) Error of u_{rms} as a function of the grid resolution normalized by the half channel height δ ; (b) Error of u_{rms} as a function of the grid resolution normalized by the matching height h_{wm} . Blue, $h_{wm} = 0.2\delta$; red, $h_{wm} = 0.1\delta$	69
FIGURE 3.8	Grid convergence of mean flow direction $\gamma = \arctan(W/U)$ in 3DTBL. (a) Error of γ as a function of the grid resolution normalized by the boundary layer thickness δ ; (b) Error of γ as a function of the grid resolution normalized by the matching height h_{wm} . Blue, $h_{wm} = 0.15\delta$; black, $h_{wm} = 0.1\delta$, red, $h_{wm} = 0.05\delta$	69
FIGURE 3.9	Grid convergence of rms intensity u_{rms} in 3DTBL. (a) Error of u_{rms} as a function of the grid resolution normalized by the boundary layer thickness δ ; (b) Error of u_{rms} as a function of the grid resolution normalized by the matching height h_{wm} . Blue, $h_{wm} = 0.15\delta$; black, $h_{wm} = 0.1\delta$, red, $h_{wm} = 0.05\delta$	71
FIGURE 3.10	Grid convergence of the spectral energy contributed by different types of eddies in WMLES of turbulent channel flow at $Re_\tau = 1000$ (matching height $h_{wm} = 0.2\delta$). The energy from different types of eddies is calculated by integrating over corresponding length scale ranges according to Parseval's theorem. The length scales of the attached eddies are defined as given in Eq. (3.12). In the current channel flow, the definition is valid in the wall normal range $100 \leq y^+ \leq 350$. (a) Grid convergence of the energy of small-scale eddies; (b) grid convergence of the energy of attached eddies. Line types are for different cases as described in Table 1. Dotted lines: case 3; dashed lines: case 4; solid lines, case 5.	73

FIGURE 3.11	(a) Proportion of the spectral energy (streamwise velocity) as a function of length scales (λ_x^+ , streamwise wavelength) and wall distance (y^+). The result is computed from the DNS data Li et al. (2008); Perlman et al. (2007). The color denotes the percentage of the energy contained in eddies of scales larger than certain wavelength. Three colored solid lines in the small-scale (SE) eddy zone denote the minimum length scales to be resolved for representing 70% (red), 80%(blue) and 90%(black) of the energy contained in the small-scale eddies. The triangular region formed by the three black dashed lines denotes the scales of the attached eddies as given in Eq. (3.12). (b) Fraction of the small-scale eddies' energy being resolved in WMLES ($h_{wm} = 0.2\delta$) at different wall-normal locations. Black dotted line, case 3; black dashed line, case 4; black solid line, case 5.	74
FIGURE 4.1	Profiles of flow statistics in wall units in turbulent channel flow at $Re_\tau = 395$. (a) Mean streamwise velocity; (b) Turbulence intensities (u_{rms} , v_{rms} and w_{rms}). Black squares, DNS (Moser et al., 1999); green solid line, LES with DSM; red dashed line, LES with PDL2; blue dash-dotted line, LES with PDWL2.	79
FIGURE 4.2	Mean velocity profiles of channel flow at $Re_\tau = 395$. Squares, DNS (Moser et al., 1999); green solid line, LES with DSM; red dashed line, LES with PDL2; blue dash-dotted line, LES with PDWL2; magenta dotted line, LES with non-principal components model, PDOFF; olive green dashed line, LES with PDMAX; cyan solid line, no SGS model.	80
FIGURE 4.3	Average SGS eddy viscosity from LES of channel flow at $Re_\tau = 395$. SGS eddy viscosity is normalized by kinematic viscosity. (a) Linear scale. (b) Log scale. Green solid line, LES with DSM; red dashed line, LES with PDL2; blue dash-dotted line, LES with PDWL2. In (b), black solid/dashed lines are y^3/y^2 reference lines, respectively.	81
FIGURE 4.4	Profile of J (the L2 norm of the GIE tensor) along the wall-normal direction in channel flow at $Re_\tau = 1000$. (a) J is not normalized; (b) J is normalized by a combination of mean velocity gradient dU/dy and Reynolds stress $\langle u'u' \rangle$. Green solid line, LES with DSM; red dashed line, LES with PDL2; blue dash-dotted line, LES with PDWL2.	82
FIGURE 4.5	Mean velocity in the 3DTBL. (a) Mean velocity magnitude; (b) Mean flow direction $\gamma = \arctan(W/U)$. Squares, DNS (Spalart, 1989); green solid line, LES with DSM; red dashed line, LES with PDL2; blue dash-dotted line, LES with PDWL2.	83
FIGURE 4.6	Streamwise mean velocity profiles in the flow over periodic hills ($Re = 10595$) from $x/h = 0.05, 1.00, 2.00, 4.00, 8.00$. Profiles are shifted along the abscissa by 1.2. Black squares, experiment (Rapp and Manhart, 2011); green solid line, LES with DSM; red dashed line, LES with PDL2; blue dash-dotted line, LES with PDWL2.	84
FIGURE 4.7	Mean velocity in the 3DTBL. (a) Mean velocity magnitude; (b) Mean flow direction $\gamma = \arctan(W/U)$. Black squares, DNS; green solid line, LES with DSM; red dashed line, LES with DTCSM; blue dash-dotted line, LES with DTCSM-PD.	86

CHAPTER 1

INTRODUCTION

1.1. Motivation and background

The capability to predict high Reynolds number turbulent flows is essential for many natural and engineering flows such as external aerodynamics of wind turbines and aircraft wings, flow over the hull of marine vehicles, atmospheric boundary-layer flow over complex landscapes and cityscapes, to name a few. However, due to extreme disparity of scales present in high Reynolds number wall-bounded turbulent flows, any attempt to simulate these flows directly on a computational grid without resorting to modeling of some sort results in prohibitively large computational cost.

Direct numerical simulation (DNS) is considered as the highest-fidelity numerical tool in computational fluid dynamics (CFD) since it requires no modeling necessity other than the continuum hypothesis and the constitutive equations. However, as a consequence, it needs to resolve all the scales of turbulent motions including the smallest dissipative eddies. Such resolution requirement leads to a total number of grid points scaling as $O(Re_L^{37/14})$ (Choi and Moin, 2012) for a spatially developing turbulent boundary layer, where Re_L is the characteristic Reynolds number. The application of DNS is therefore limited to low Reynolds number turbulent flows. The widely-used tool in the commercial CFD software is the Reynolds-averaged Navier-Stokes equations (RANS) approach. As the name suggests, RANS solves time-averaged or ensemble-averaged Navier-Stokes equations and aims to capture the mean-flow field only. The effects of all the scales of turbulence motions on the mean flow need to be modeled. It is therefore hard to have an universal RANS model that generally works well for different cases. However, RANS is computationally much cheaper than DNS, which is why it is popular in the industry. RANS only requires to have fine grid resolution in the wall-normal direction to resolve the sharp velocity gradient. It can have very coarse wall-parallel grid resolution since it doesn't need to resolve the small-scale fluctuating motions.

Large-eddy simulation (LES) is another cost-effective alternative to DNS. However, instead of modeling all the fluctuations as what is done in RANS, LES still aims to capture the large (stress-

carrying) eddies. In practice, LES solves the governing equations on a computational grid which is too coarse to represent the smallest physical scales but fine enough to resolve the energy-containing scales of motions (low-frequency modes in space). The unresolved scales of motions are modeled as subgrid-scale stress (SGS) terms in the governing equations. The physics of these unsolved small eddies are more universal than that of the large eddies. Therefore the SGS models tend to be more generally applicable to different flow scenarios than RANS models and LES is considered as a more reliable and accurate numerical tool compared to RANS.

The requirement to directly capture the most energetic scales of motions is not always easy to fulfill. In wall-bounded turbulent flows, the length scales of energy-containing eddies get progressively smaller toward the wall. High Reynolds number is another challenge for LES since the characteristic length scales of turbulence-production events decrease as Reynolds number increases. LES which resolves all the near-wall energy-containing eddies is called wall-resolved LES (WRLES). The grid point requirement of WRLES for a spatially developing turbulent boundary layer scales as $O(Re_L^{13/7})$ (Choi and Moin, 2012). Although it reduces substantially compared to DNS ($O(Re_L^{37/14})$), this level of computational cost is still unaffordable when the Reynolds number is high. A recent study by Yang and Griffin (2021) also shows that the total computational cost for WRLES is actually approaching DNS when the time step effect is incorporated into the cost consideration. The total computational cost for WRLES and DNS scales as $Re_L^{2.72}$ and $Re_L^{2.91}$ respectively. In order to alleviate this problem, the key task is to develop a model for the computationally demanding inner-layer dynamics. With this inner-layer model, the cost of LES is dictated solely by the resolution of the energetic eddies in the outer portion of the boundary layer, which makes LES affordable without sacrificing its superior predictive capability. This is the concept of wall-modeled LES (WMLES) in which the outer layer is resolved using a coarse LES while the effect of momentum and heat transfer from the inner layer to the outer layer is modeled. The cost scaling changes from $O(Re_L^{13/7})$ to $O(Re_L)$ (Choi and Moin, 2012) in terms of required number of grid points. When the time step effect is taken into consideration, the total computational cost scaling reduced from $O(Re_L^{2.72})$ to $O(Re_L^{1.14})$ (Yang and Griffin, 2021).

With the superiority in fidelity and cost, WMLES and hybrid RANS/LES are identified as the only feasible ways of predicting high Reynolds number wall-bounded turbulent flows in external aerodynamics according to NASA CFD vision 2030 report (Slotnick et al., 2014). However, there are still several challenges remaining to be addressed for the successful and extensive applications of WMLES in the practical aerospace engineering problems. First, comprehensive assessment of wall-model performance in turbulent boundary layers experiencing pressure gradient and exhibiting mean-flow three-dimensionality is still needed. Many modeling assumptions built on two-dimensional canonical turbulent boundary layers are challenged in flows with pressure gradient and skewed mean-velocity profiles which are more the rule than the exception in the engineering applications such as the swept wings deployed in the aircraft. Second, few WMLES studies have thoroughly discussed about the invariance of the statistics with respect to the grid resolution. The current practice is to establish the grid convergence through a series of numerical simulations with successively refined mesh. However, this practice could be extremely expensive in complex geometry, high Reynolds-number flows in which the mesh generation process and running the simulation are both time-consuming. Therefore, a proper notion of grid convergence in WMLES should be established. The last unresolved question is generally related to LES. The success of LES is inseparable from the invention of the dynamic SGS model in which the modeling coefficients can be dynamically computed instead of being tuned a priori. However, the underlying mechanism of dynamic model is just vaguely understood (Meneveau and Katz, 2000; Pope, 2004) and requires more investigation.

The objective of this work is to investigate the above challenges remained for the WMLES community. Resolving these problems will help us to know the capabilities and limitations of different wall models in nonequilibrium turbulent boundary layers. Therefore, wall models with different levels of complexity can be properly chosen in different flow scenarios and numerical predictions can be efficient and accurate. A guidance for obtaining grid-converged WMLES results will be built so that reliable numerical simulations can be conducted without incurring significant cost overhead.

1.2. Literature review

1.2.1. Wall-modeled large-eddy simulation

WMLES can be broadly categorized as hybrid RANS/LES and wall-stress modeling approaches. In hybrid RANS/LES framework, RANS equations are solved near the wall and interface to an LES away from the solid boundary. In wall-stress modeling formulation, LES equations are valid in the whole domain whereas the wall boundary conditions are augmented to account for the effect of the unresolved inner portion of the boundary layer. In the current study, the focus is only on the wall-stress modeling strategy.

Wall-stress modeling is inspired by the role played by the wall stress in the mean momentum balance across the boundary layer. The momentum integral analysis of the boundary layer equations reveals that the total stress at any given point in the boundary layer is determined by the wall stress and pressure gradient (Bose and Park, 2018). In WMLES, LES equations are solved on a coarse mesh, where the stress-carrying eddies in the near-wall region are mostly unresolved. The LES mesh alone cannot represent the sharp velocity gradients and the momentum transport near the wall. This causes SGS models to produce insufficient levels of modeled stresses. Wall modeling aims to compensate for such numerical and modeling errors in the underresolved near-wall region of LES, by augmenting the total stresses directly through the imposition of the modeled stress boundary condition at the wall in lieu of the no-slip condition. In the present work, wall models solve simplified, vertically integrated, or full RANS equations on a separate near wall mesh. The grid for wall models have fine resolution in the wall-normal direction (with the exception of the integral nonequilibrium wall model, which does not require a wall-normal grid), but the wall-parallel grid resolution (if any) is identical to or coarser than the LES grid. All wall models in this study are driven by the LES states imposed at their top boundaries, which are taken at a specified matching height in the LES grid. At each time step, wall stress and heat flux obtained from the wall model are used as the Neumann wall boundary condition for the LES. Figure 1.1 shows a schematic of the wall modeled LES procedure employed in the present work.

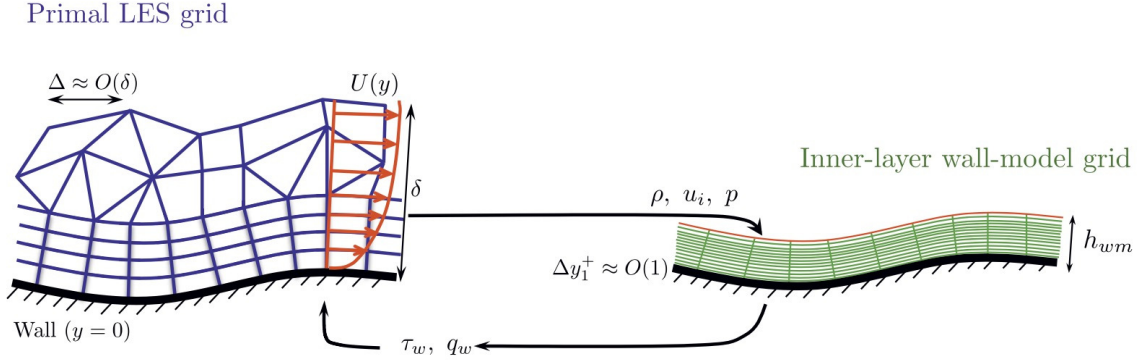


Figure 1.1: Sketch of the wall-stress modeling procedure (reproduction from figure 1 of Park and Moin (2016a)). Wall shear stress (τ_w) and heat flux (q_w) are solved from the wall model equations on a separate near-wall mesh. Wall models are driven by the LES states imposed at their top boundaries while the no-slip condition is applied at the wall.

To date, several wall models have been proposed, most of which are based on some form of the law-of-the-wall or solving a set of simplified or full Reynolds-averaged Navier-Stokes (RANS) equations. Deardorff (1970) and Schumann (1975) were the first to recognize the need for wall modeling to perform LES of high Reynolds number plane channels and annuli to overcome lack of computing resources in the 1970s. Grötzbach (1987) later improved the model by removing the necessity of a priori knowledge of the mean wall shear stress. The geometry of the near-wall eddies was incorporated in the work of Piomelli et al. (1989) to account for the inclination of the vortical structures in the streamwise/wall-normal plane. Wang and Moin (2002) proposed an ordinary differential equations (ODE) based wall model derived from the equilibrium assumption (Degraaff and Eaton, 2000), which later on was extended to compressible flows (Kawai and Larsson, 2012; Bodart and Larsson, 2011). The ODE equilibrium wall model excludes the nonequilibrium effects such as pressure gradient, and considers the wall-normal diffusion only. Nonequilibrium wall models based on full 3D RANS equations were investigated by Balaras et al. (1996), Wang and Moin (2002), Cabot and Moin (2000), Kawai and Larsson (2013), and Park and Moin (2014, 2016a). Yang et al. (2015) introduced the integral nonequilibrium wall model based on the integrated boundary layer equations and assumed velocity profiles, which can be considered as a compromise between the aforementioned two classes of wall models. Several efforts have also been directed toward for-

mulating wall models which are not based on RANS. Bose and Moin (2014) and Bae et al. (2019) proposed a differential filter-based wall model which introduced a slip-velocity applied in the form of Robin boundary condition at the wall. Chung and Pullin (2009) proposed a virtual wall model with a slip velocity boundary condition specified on the lifted virtual wall. Gao et al. (2019) extended this virtual wall model in a generalized curvilinear coordinate. Advances on WMLES were reviewed by Piomelli and Balaras (2002), and more recently by Larsson et al. (2016) and Bose and Park (2018). With the development of novel wall models and increase in the computing capacity, WMLES is becoming an indispensable tool for predictive but affordable scale-resolving simulation of practical engineering flows at high Reynolds numbers. Recent applications to external aerodynamics applications include simulation of a wing-body junction flow (Lozano-Durán et al., 2021) and flow over a realistic aircraft model in landing configuration deploying high-lift devices (Goc et al., 2021).

Although WMLES is now gaining popularity as a high-fidelity tool balancing the computational cost and the accuracy, with the potential to be used for design and optimization in practical engineering applications because of its reasonable turnaround times, comprehensive benchmark studies on the comparison of different wall models in complex flows are lacking. There have been a number of comparative studies of WMLES with different wall models or subgrid scale (SGS) models. Wang et al. (2020), Yang and Bose (2017) have done comparative studies of three wall models (including equilibrium wall model, slip wall model and integral nonequilibrium wall model) in turbulent channel flow. Rezaeiravesh et al. (2019) has done a systematic study of accuracy of WMLES using algebraic wall model. The sensitivities of the choice of SGS models, matching height, grid resolution and law of the wall parameters are investigated. However, it should be noted that the nonequilibrium terms that are added to the more complicated wall models are essentially zero in canonical flows like turbulent channel flow. This fact limits the full understanding of the performance of more complicated wall models. Therefore, comparative studies of WMLES with different wall models in more realistic turbulent flows with nonequilibrium effects such pressure gradient and mean-flow three-dimensionality are highly needed for the guidance of the applicability of different wall models in different scenarios.

Park (2017) compared the performance of ODE equilibrium wall model and PDE nonequilibrium wall model in a separating and reattaching flow over the NASA wall-mounted hump. Whitmore et al. (2021) investigated the flow over Gaussian bump with equilibrium and slip wall models. Lozano-Durán et al. (2020) tested three RANS based wall models (ODE equilibrium wall model, integral nonequilibrium wall model and PDE nonequilibrium wall model) in a three-dimensional transient channel flow. For the latter study, it is worth noting that the three wall models were not tested using the same LES code. The lack of a like-for-like comparison of different wall models, especially in flows with nonequilibrium effects such as mean-flow three-dimensionality and pressure gradient, warrants a systematic study of various wall models under the identical settings of the same solver and the same flow conditions. This will facilitate a clear assessment of the differences in the performance of different wall models, both in terms of the accuracy and the computational cost. Foregoing in view, in the present work, we test three wall models in a three-dimensional turbulent boundary layer flow: an ODE equilibrium wall model (EQWM), an integral nonequilibrium wall model (integral NEQWM), and a PDE nonequilibrium wall model (PDE NEQWM). These three models respectively represent increasing model complexity with correspondingly increasing physical fidelity for predicting 3DTBLs. The equilibrium wall model assumes that the velocity profile is unidirectional and neglects all nonequilibrium effects, while the latter two are capable of representing skewed velocity profiles and incorporate some or all nonequilibrium effects, albeit in an averaged sense.

Before describing the 3DTBL in more detail, a few remarks are in order regarding the suitability of the current choice of 3DTBL flow to conduct the comparative study of wall models with different physical fidelity. Historically, much of the research on wall turbulence has focused on statistically two-dimensional (2D) equilibrium turbulence in simple geometries (e.g., channel, pipe and flat plate). Different wall models perform equally well therein, making it hard to justify the use of more complex models. Furthermore, many practical flows of interest, such as those found on the swept wings of aircraft, wing/body juncture, bow/stern regions of ships and turbomachinery, are strongly affected by the mean-flow three-dimensionality. Such 3DTBLs challenge the validity of the theories and models established from the canonical 2D wall turbulence and thus provide a good stage to

exhibit the distinctive capabilities of different wall models. Therefore, the current study of turbulent boundary layer with mean-flow three-dimensionality is well suited to test different wall models, and to explain the physical origins of the differences in the results of these models. We also compiled all pertinent published papers on the comparison of wall models in Table 1.1. Most of the comparisons are done in canonical flows like doubly periodic channel flow, with a few considering a variant of doubly periodic channel with mean-flow three-dimensionality introduced by the sudden imposition of the spanwise pressure gradient. Only Wang and Moin (2002), Kawai and Asada (2013) and Park (2017) have done comparative studies on different wall models in realistic turbulent boundary layers with nonequilibrium effects. All works deployed at least one homogeneous spatial direction along which the periodic boundary condition was applied. On the contrary, in the present study, all mean velocity components are non zero, where they vary in all spatial coordinates without any direction of periodicity/homogeneity. It is fair to say that our work is the first one for the comparative study of three wall models in a realistic and challenging situation involving pressure-driven 3DTBL. It is our opinion that comparison or validation of wall models in canonical flows provides only limited perspectives to what the models can and should do. Our study is unique in that it clearly goes beyond this barrier by considering a flow with complex three dimensional mean flow, and our work is important in that it provides a novel physics-based insights on wall-model performance in 3DTBL for the first time.

1.2.2. Three dimensional turbulent boundary layer

The 3DTBLs can be classified as pressure-driven (also termed skew-induced (Bradshaw, 1987) or inviscid-induced (Lozano-Durán et al., 2020)), or shear-driven (also termed viscous-induced (Lozano-Durán et al., 2020)) ones, according to the mechanisms by which the mean three dimensionality is introduced into the flow. For the pressure-driven 3DTBLs, the crossflow is induced by the imposition of spanwise pressure gradient. More specifically, the mean three-dimensionality is produced by reorienting (tilting) the existing mean spanwise vorticity to generate non-zero streamwise vorticity. This process is often referred to as “inviscid skewing” due to its quasi-inviscid nature, and streamwise variation in the imposed spanwise pressure gradient often facilitates this vorticity tilting

List of comparative study of WMLES		
Authors	Wall models	Cases
Wang and Moin (2002)	EQWM and NEQWM	Spanwise-periodic asymmetric trailing edge (2,2)
Park (2017)	EQWM and NEQWM	Spanwise-periodic wall-mounted hump (2,2)
Kawai and Asada (2013)	EQWM and NEQWM	Spanwise-periodic airfoil (2,2)
Lozano-Durán et al. (2020)	EQWM, NEQWM and integral NEQWM	Doubly periodic channel (transient) (2,1)
Wang et al. (2020)	EQWM, integral NEQWM and slip wall model	Doubly periodic channel (1,1)
Yang and Bose (2017)	EQWM, integral NEQWM and slip wall model	Doubly periodic channel (1,1)
Bae et al. (2019)	EQWM and slip wall model	Doubly periodic channel (1,1), Doubly periodic channel (transient) (2,1), Spanwise-periodic flat-plate boundary layer (2,2)
Fowler et al. (2022)	EQWM and Lagrangian relaxation towards equilibrium wall model	Doubly periodic channel (1,1), Doubly periodic channel (transient) (2,1)

Table 1.1: List of papers with the comparison of different wall models. Numbers in the parentheses in the last column in the form of (C, d) denote the number of non-zero mean velocity components (C) in (U, V, W) and the number of spatial dimensions (d) they depend upon. **It should be noted that the flow considered in the present study corresponds to $(C, d) = (3, 3)$, where all mean velocity components are non zero, they vary in all spatial coordinates, without any direction of periodicity/homogeneity.**

(Coleman et al., 2000). Examples of this type of 3DTBLs include flows in a square duct with a bend (Schwarz and Bradshaw, 1994; Flack and Johnston, 1994), in an S-shaped duct (Bruns et al., 1999), over wing-body junctures (Rumsey, 2018), over swept wings (Bradshaw and Pontikos, 1985), and over prolate spheroids (Chesnakas and Simpson, 1994). For the shear-driven 3DTBLs, the crossflow is induced by the viscous diffusion of mean spanwise shear from the wall. Examples of this class include flows within a spinning cylinder (Bissonnette and Mellor, 1974; Lohmann, 1976; Driver and Hebbbar, 1988), over a rotating disk (Littell and Eaton, 1993), over turbomachinery and in Ekman layers. In the present work, we are interested in the *skew-induced* cases which are more prevalent in external hydrodynamics or aerodynamics applications.

Over the past decades, studies on 3DTBL have unraveled its distinctive features which set it apart from the canonical 2D wall turbulence. First, the mean-flow direction in 3DTBL varies along the wall-normal direction, resulting in a skewed velocity profile. The law-of-the-wall, which is the characteristic of the canonical 2D wall turbulence, is therefore challenged in 3DTBL. Second, the Reynolds shear stress vector is not aligned with the mean velocity gradient vector in 3DTBLs. Thus the Reynolds shear stress response in 3DTBL can lag behind or lead that predicted by the isotropic eddy viscosity models which assume perfect alignment of the two. Third, a reduction in the structure parameter (the ratio of the total Reynolds shear stress magnitude to twice the turbulent kinetic energy) is often observed in 3DTBLs, whereas this parameter is nearly constant (roughly 0.15) in the outer layer of 2DTBL. The aforementioned features of 3DTBL pose a fundamental challenge to the validity of the underlying assumptions in many turbulence models (including wall models) that are based on 2DTBL, and therefore bring into question the reliability of these models when applied to practical flows.

The numerical studies of 3DTBLs using direct numerical simulation (DNS) and large-eddy simulation (LES) have mostly focused on deformed 2D wall turbulence. These studies include channel flow subject to sudden crossflow pressure gradients (Lozano-Durán et al., 2020; Sendstad, 1992), channel flow with spanwise wall motions, channel flow subject to mean strains (Coleman et al., 2000), TBL over an idealized infinite swept wing generated by a transpiration profile (Coleman et al., 2019),

TBL subject to streamwise-varying pressure gradient (Bentaleb and Leschziner, 2013), and TBL on a flat plate with a time-dependent freestream velocity vector (Spalart, 1989). These numerical studies are limited to relatively low Reynolds number and idealized 3DTBLs due to the large computational cost. The present study focuses on a realistic, spatially-developing, pressure-driven 3DTBL over the floor of a duct with a bend (Schwarz and Bradshaw, 1994), which is at a considerably higher Reynolds number than the past studies but still providing a good balance between the physical realism, the tractability of the underlying 3DTBL mechanisms, and the computational cost of the simulations.

1.2.3. Grid convergence

Demonstrating the invariance of the numerical solution with respect to grid spacing (particularly for high Reynolds number turbulent flows) is a fundamental requirement and a basic premise for the reliability of the CFD results. As pointed out in the NASA CFD 2030 Vision report (Slotnick et al., 2014), a key factor limiting the effectiveness of current and future turbulence models is the impact of grid resolution on both the accuracy and the convergence properties of the models. This applies to all the CFD techniques for turbulence including RANS, LES and DNS.

In LES, the large-scale, energy-containing eddies must be resolved, while the effect of the more isotropic and homogeneous small-scale eddies are modeled. Theoretically, the LES equations are solved for the filtered flow field, and the converged LES results in principle should be related closely to the filter width. In a finite difference framework, Ghosal (1996) showed that the numerical errors are quite large compared to the subgrid-scale (SGS) force. It has also been shown that the errors can be reduced by implementing LES with a filter width larger than the grid size. However, in most cases, the grid itself and the finite resolving power of discrete math operations (differentiation/interpolation/integration) are considered as an implicit filter. This implicitly-filtered LES accounts for the majority of the LES calculations performed, the results of which are by construction sensitive to the grid resolution. This aspect may be considered desirable in the sense that LES has a direct path to the first-principle based approach (fully converged LES approaches DNS). On the other hand, this renders numerical and modeling errors fundamentally inseparable, because reduc-

tion of the former by grid refinement leads to reduction of the model contribution. Albeit rarely attempted in practice, the explicitly filtered LES approaches aim at formal separation of numerical and modeling errors through a real mathematical filter (in lieu of implicit grid filter) at work in LES. Specifically, the grid refinement process while keeping the filter width constant (larger than the grid spacing) is known to produce grid-independent LES solution, where numerical error is suppressed in the presence of finite modeling error. Lund (2003) implemented two-dimensional explicit filters for a turbulent channel flow and showed that explicit filtering can improve the accuracy of LES. However, it was found that mesh refinement without explicit filtering can improve the computed statistics at a greater rate. Bose et al. (2010) discussed the grid-independent turbulent statistics and energy spectra in turbulent channel flow, showing that the errors of the grid-independent LES solution (with respect to the filtered DNS) can be attributed to the subfilter stress model in the explicitly filtered LES framework. Alternatively, Piomelli et al. (2015) proposed a different notion of grid-independent LES, showing that it can be conducted without the need to deploy explicit filters but by the use of a grid-independent integral length scale for modeling the subfilter motions. The grid convergence behavior of LES in general becomes subtler in the presence of walls. Meyers and Sagaut (2007) presented a non-monotonic convergence behavior of a coarse DNS at resolutions typical of LES, alluding to possibilities in practice where LES solution with incomplete convergence but showing good agreement with experiments/DNS can be erroneously taken as the terminal CFD prediction.

Since wall-resolved LES (WRLES) of wall-bounded flows becomes prohibitively expensive at high Reynolds numbers, wall-modeled LES (WMLES) is typically used to study these flows, where the energetic eddies are only resolved in the outer layer and the unresolved momentum transport near the wall is modeled. The notion of grid convergence is currently not well established in WMLES. Several unanswered questions of practical importance can be raised. What final converged state do we expect for WMLES to reach? What is the best practice for conducting grid refinements in WMLES? Is it possible to know if one has obtained a WMLES solution that would not respond to further grid refinements, without conducting full convergence study down to the WRLES limit? The high cost of a well-resolved solution of high Reynolds number wall-bounded turbulent flows has rendered

answering these questions difficult, but recent attempts are noteworthy. Lozano-Durán and Bae (2019) investigated the error scaling of flow statistics in a turbulent channel flow at a moderately high Reynolds number, with the exact mean wall stress imposed at the wall as a perfect wall model. Rezaeiravesh et al. (2019) studied turbulent channel flows to examine the effects of resolution and anisotropy of grid on WMLES together with the sensitivity to wall modeling parameters, wall model matching location, numerical convective scheme, and SGS modeling. While addressing a critical wall-modeling error (the log-layer mismatch) in their seminal work, Kawai and Larsson (2012) proposed a mechanism of the log-layer mismatch in flat-plate boundary layers that hinted at subtle interaction of modeling and numerical errors in the grid refinement process, the remedy of which (avoiding use of the wall-adjacent information for wall modeling) has become a widely accepted practice. In practical engineering applications involving complex geometries and high Reynolds-number flows, attempts are often made to demonstrate grid convergence through a sequence of simulation campaigns on successively finer meshes until the key quantities of interest no longer show significant changes with grid refinements. These refinement studies are typically not carried out down to the WRLES limit, because the cost is prohibitive (also note that doing so, even if possible, would defeat the purpose of wall modeling). Park (2017) conducted grid convergence study for the WMLES of flow over the NASA wall-mounted hump. Three grids with different refinement levels were used (11.7M, 12.9M and 36.3M). It was shown that LES with NEQWM had mostly converged on medium grid while LES with EQWM had a slower and less monotonic convergence. It was also mentioned that the mean flow from no-slip LES (without wall modeling) was only marginally worse than WMLES on medium and fine grids, indicating that these grids were approaching the wall-resolved LES resolutions. Similar grid convergence study was done by Iyer and Malik (2021) for the WMLES of flow over a Gaussian bump. The effect of grid resolution on pressure coefficient was small under the three grid resolutions used in the study, while some difference was evident in the skin friction results. Coarse grid (3.4M) result deviated significantly from DNS, but convergence was observed in medium and fine grids (16M and 25M). It should be noted that WMLES of some very high Reynolds number applications (notably, external aerodynamics) still require a very large number of grid points/cells. For instance, order of billion cells are expected for aircraft WMLES at

cruise conditions (Slotnick et al., 2014; Choi and Moin, 2012; Tamaki and Kawai, 2023). The usual practice of demonstrating grid independence through two to three refinement levels can be still very challenging to conduct due to the computational cost, especially when the flow at interest exhibits slow time scales (e.g., large separation bubble on stalled wings) (Goc et al., 2019, 2021, 2022; Tamaki and Kawai, 2023). In this situation, knowing when it is okay to stop the grid refinement and establishing confidence on the invariance of WMLES prediction become practically important questions.

In the present work, we propose a hypothesis that the convergence behavior of WMLES (conducted with wall-stress models) is controlled by the extent of the wall-modeled region, commonly referred to as the matching location. We study the grid convergence trend of WMLES in a canonical statistically one-dimensional (1D) turbulent channel flow, as well as a three-dimensional turbulent boundary layer (3DTBL). The relation between how convergence starts/ends and the wall model matching location is investigated. The quantities of interest include the mean wall-shear stress, mean velocity, and turbulence intensity.

1.2.4. Dynamic modeling

Dynamic closure of the subgrid-scale (SGS) stress is perhaps the most celebrated feature of large-eddy simulations (LES), which is absent in other lower-fidelity approaches for modeling turbulence. The class of dynamic SGS models allows for the determination of model coefficients purely from the resolved-scale information available in live LES calculations, eliminating the need for the ad-hoc practice of parameter calibration and therefore greatly promoting the predictive nature of the method. It was Germano et al. (1991) who first introduced the idea of the dynamic procedure, proposing the dynamic Smagorinsky model (DSM). This formulation was based on the Germano identity which is an algebraic relation between the SGS stresses at two different filter levels and the resolved turbulent stresses. Lilly (1992) proposed a modification by minimizing the Germano-identity error (GIE) which has become the most widely adopted practice.

Compared to the massive works that apply the DSM to the study of turbulent flows, the mechanism behind why the DSM is successful is much less understood. The explanation based on scale invari-

ance in the inertial subrange was initially adopted, but it was later challenged by Jiménez and Moser (2000) who claimed that the DSM’s success is thanks to the model’s robustness to errors in the physics. Pope (2004) brought another perspective that the dynamic procedure minimizes the dependence of relevant turbulence statistics (total Reynolds stresses) on filter levels. Toosi and Larsson (2021) complemented the understanding by showing the connection between the GIE and the residual of the LES governing equations.

Closely related to the interpretation of the GIE tensor, how one minimizes the GIE can make a difference in the SGS stress modeling. Ghosal et al. (1995) recast the solution procedure of the model coefficient in the context of a variational problem, generalizing the dynamic procedure to flows without homogeneous directions. Meneveau et al. (1996) introduced a Lagrangian dynamic procedure where the GIE is minimized along the flow pathlines, allowing for the application of the model to inhomogeneous flows in complex geometries. Morinishi and Vasilyev (2001) proposed a modification for the dynamic two-parameter mixed model to improve the model performance in wall-bounded turbulent flows. Park and Mahesh (2009) explored reduction in an ensemble-averaged GIE and proposed an efficient predictor-corrector-type method to find the optimal parameter. Denaro (2013) derived the integral-based Germano identity which showed much less sensitivity to the type of contraction than expected in the differential-based formulation. Agrawal et al. (2022) proposed a tensorial Smargorinsky coefficient in the DSM to overcome the invalid assumption of alignment between the filtered strain-rate tensor and the SGS stress.

The present study aims to provide an alternative explanation of the mechanism behind some dynamic SGS models rooted in the Germano identity. Specifically, we show that only a few directions matter for these models, namely, the principal directions of the filtered strain-rate tensor. The idea is demonstrated in turbulent channel flow, a three-dimensional turbulent boundary layer (3DTBL), and a separating flow over periodic hills.

1.3. Accomplishments

Key contributions of this study are listed below.

- Assess capabilities of wall models with increasing levels of model complexities in nonequilibrium turbulent boundary layers.
- Formal decomposition of equilibrium/nonequilibrium effects on near-wall mean flow three-dimensionality, applicable to arbitrary wall models.
- Propose a proper notion of grid convergence in the context of WMLES.
- Understand the mechanism and the role of Germano-identity error in the dynamic Smagorinsky SGS model.

CHAPTER 2

WMLES OF A 3DTBL IN A BENT SQUARE DUCT

This chapter is based on my work published in Hu et al. (2023).

2.1. Flow configuration

The reference configuration for the present study is the experimental setup of Schwarz and Bradshaw (1994). While numerous experimental studies have been reported on 3DTBLs (as discussed in Johnston and Flack (1996)), our choice of the reference experiment was motivated primarily by the following aspects of Schwarz and Bradshaw (1994) which we found to be favorable to the goals of this study: 1) the highest Reynolds number among the pressure-driven 3DTBLs experiments reported in Johnston and Flack (1996), 2) availability of the mean velocity and full Reynolds stress profiles, and of 3) the skin friction (magnitude and orientation) and pressure distribution along the wall. However, some remarks are also in order regarding limitations of the experiment. First, direct wall-stress data is not available, instead, a fit to the log law near $y^+ \approx 100$ was used for indirect stress measurement. Second, the description of the zero-pressure gradient region far upstream of the bend region for the purpose of CFD inflow generation is incomplete, therefore requiring an iterative procedure in the inflow generation to match the reported statistics at the first streamwise measurement station.

The experiment featured a spatially developing incompressible turbulent boundary layer, growing along the floor of a square duct with a 30° bend (see Fig. 2.1). It should be noted that the boundary layer on the floor was very thin compared to the duct height, with δ_{99}/D ranging between 0.026 and 0.07 throughout the test section, where D is the width (or height) of the square duct. The flow was far from being fully developed, and the secondary flow near the corner regions was expected to have negligible influence on the centerline region, which was the primary region of interest in the experiment.

Following Schwarz and Bradshaw (1994), two coordinate systems are employed here to facilitate

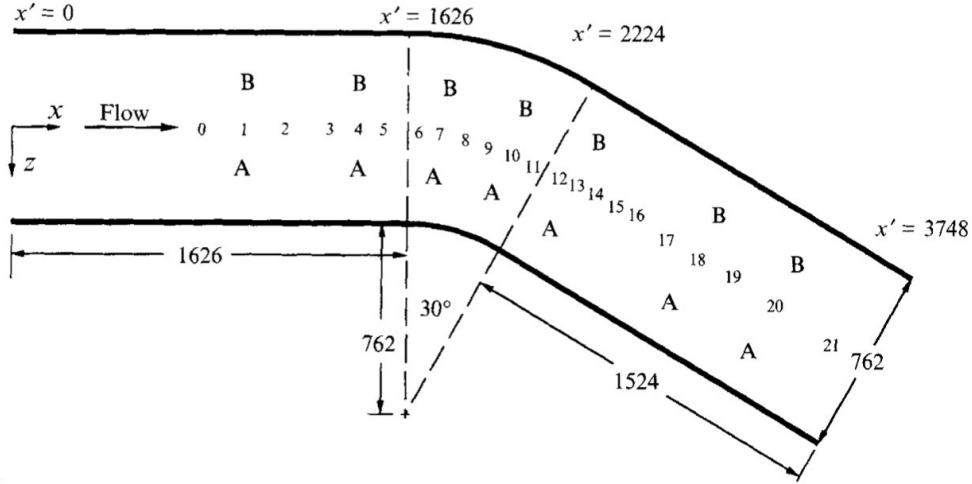


Figure 2.1: A Schematic of the floor of the duct with a 30° bend (reproduction from figure 1 of Schwarz and Bradshaw (1994)). The measurement locations in the experiment are marked as numbers 0-21 along the duct centerline. Two coordinate systems are employed. (x, y, z) is a fixed coordinate system with the origin located at the inlet. (x', y', z') is a curvilinear coordinate system aligned with the local duct centerline (measurements in mm).

the presentation of the results: (x, y, z) denotes the global Cartesian coordinate system; (x', y', z') denotes a curvilinear coordinate system aligned with the local duct centerline. $y = y'$ are the wall-normal coordinates (distance from the floor of the duct). In the experiment, the boundary layer on the floor was tripped using a trip wire at the duct inlet located at $x' = 0$, thus ensuring a turbulent boundary layer over the entire floor of the test section. Boundary layers on the other three walls of the duct were not tripped (Schwarz, private communication, 2019). Reynolds number is moderately high, with Re_θ ranging between 4100 and 8500 (or Re_τ roughly ranging between 1500 and 3900). The flow along the centerline upstream of the bend was reported to exhibit typical characteristics of the canonical 2D zero pressure gradient (ZPG) flat-plate boundary layer. Mean-flow three-dimensionality was generated in the bend region approximately between $x' = 1626$ mm and $x' = 2224$ mm due to the cross-stream pressure gradient induced by the bend. The surface streamlines were deflected by up to 22 degrees relative to the local duct centerline. Downstream of the bend, the 3DTBL gradually returned to a 2DTBL owing to the vanished spanwise pressure gradient. The experimental study focused on the boundary layer along the local centerline where the streamwise pressure gradient was found to be small.

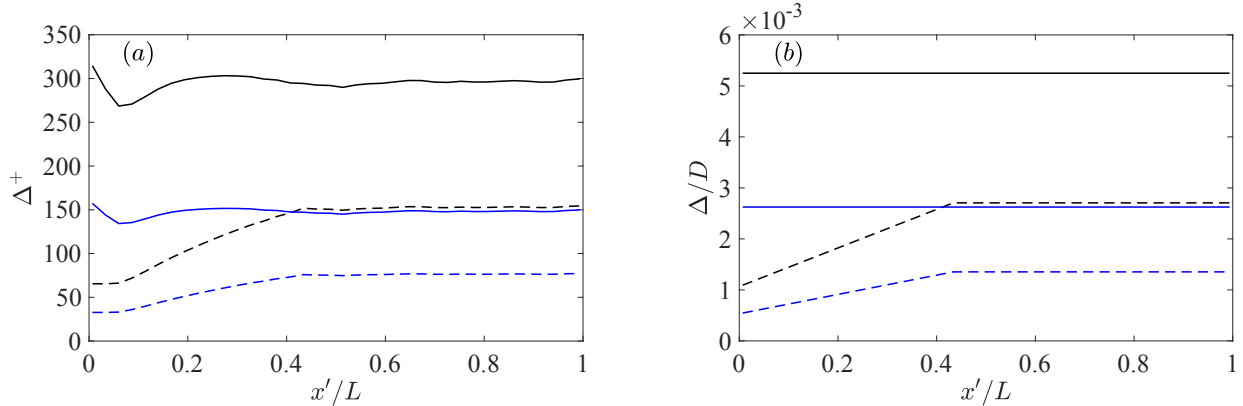


Figure 2.2: (a) Near-wall grid spacing distributions in wall units (based on the local skin friction) along the duct centerline. (b) Near-wall grid spacing distributions (normalized by duct height D) along the duct centerline. Solid lines, wall-parallel grid spacing ($\Delta x = \Delta z$); dashed lines, wall-normal grid spacing (Δy). Black, coarse mesh; blue, fine mesh.

The computational domain is identical to the test section in the experiment, which consisted of a square duct ($D \times D = 0.762\text{m} \times 0.762\text{m}$) with a total curved length of $L = 3.748\text{m}$, as shown in Fig. 2.1. Two grid resolutions are considered in the present study: a coarse mesh with 8 million control volumes and a fine mesh with 38 million control volumes. Figure 2.2 shows the near-wall grid spacing distributions along the duct centerline in the two meshes. The computational meshes are designed to maintain adequate wall-modeled LES grid resolution in the test section such that the local boundary layer contains approximately 16~23 and 32~45 cells across its thickness in the coarse and fine computational meshes, respectively. Local grid adaptations were applied in the near-wall region with the effect that the grid resolution transitions from the coarser isotropic-cell region in the freestream ($\Delta = 0.008$ m at $y/D > 0.1$) toward the finer near-wall region on the duct floor through anisotropic grid refinements. This resulted in wall-parallel grid resolutions ($\Delta x = \Delta z$) of 4 mm and 2 mm for the coarse and fine meshes, respectively. In the region upstream of the bend ($x'/L \leq 0.43$) where the boundary-layer was thin but grew fast, the wall-normal grid spacing were varied with x' to keep the number of boundary-layer resolving cells approximately constant, resulting in $\Delta y = 0.86$ mm~2.2 mm and $\Delta y = 0.43$ mm ~ 1.1 mm for the coarse and fine meshes, respectively. At $x'/L \geq 0.43$, Δy was fixed at their maximum values aforementioned. Compared to Cho et al. (2021) where WMLES of the same geometry using isotropic voronoi cells

was reported, the present study using anisotropic hexahedral cells deploys roughly the same wall-normal resolutions and about twice coarser wall-parallel resolutions in and downstream of the bend. Total cell counts are significantly reduced as a result, while maintaining higher numbers of cells across the thickness of the local boundary layer. The grid-resolution transition zones are located sufficiently away from the shear layer on the duct floor, so that the solution therein is not affected by the accuracy degrade associated with abrupt changes in grid resolution.

2.2. Inflow characterization and boundary conditions

Setting the appropriate boundary conditions in the simulation, particularly for the reproduction of flow characteristics upstream of the bend region where a typical equilibrium 2DTBL is expected, is crucial before attempting to compare the simulation results with the experimental results at any downstream location. However, the experiment reports flow statistics at the 22 locations shown in Fig. 2.1 along the duct centerline, with the first measurement location being far downstream of the test section inlet (at $x' = 826$ mm). In the absence of this critical flow information at $x' = 0$ mm, where the boundary layer on the floor was tripped in the experiment, we resort to a synthetic turbulence generation based on a digital filter approach (Klein et al., 2003) for approximating the inflow boundary condition, rather than trying to replicate the trip-wire transition in the experiment. This approach requires iterative guesses on the length of the development region (if any) to be appended upstream of the nominal trip location in the experiment ($x' = 0$ mm), and the state of the inflow to be prescribed at the new inlet location. It should be noted that the goal here is to reproduce the 2DTBL upstream of the bend reasonably well, which then acts as the inflow for the 3DTBL within the bend, rather than to exactly match the flow conditions at the test section inlet. After iterating on several inflow conditions and the inlet location, we found that prescribing a flat-plate turbulent boundary layer at $Re_\theta = 2560$ (Schlatter et al., 2010) at the nominal inlet ($x' = 0$ mm) reproduces the boundary layer statistics well at the first measurement location (station 0: $x' = 826$ mm). As shown in Fig. 2.3, the simulation agrees well with the experiment in terms of the distributions of the boundary layer and momentum thicknesses. In Fig. 2.4, it is observed that the profiles of the mean velocity and Reynolds stress components from the present calculation agree well with the experiment at the first measurement station (station 0: $x' = 826$ mm), as well as

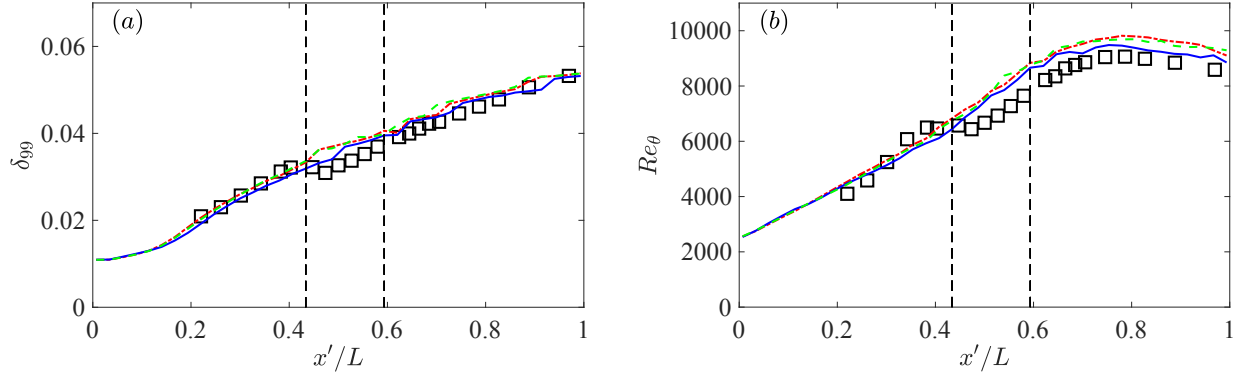


Figure 2.3: Centerline distributions of (a) boundary layer thickness and (b) momentum thickness (coarse mesh). Symbols, experiment; red dash-dotted line, equilibrium wall model; blue solid line, PDE nonequilibrium wall model; green dashed line, integral nonequilibrium wall model. Black vertical dashed lines denote the start and end of the bend region.

with a WRLES of a zero pressure gradient flat-plate boundary layer (ZPGFPBL) at a comparable Reynolds number ($Re_\theta = 4100$, Schlatter et al. (2010)).

The prescription of boundary conditions on the rest of the boundaries is relatively straightforward. A subsonic Navier-Stokes characteristic boundary condition (Poinsot and Lele, 1992) is imposed at the outlet of the duct. No attempt was made to resolve the boundary layers on the two side walls and the top wall which were not tripped in the experiment. The no-slip boundary condition is applied to each of these walls. The wall model is applied to the bottom wall, and the wall stress calculated from the wall-model solution is used as the Neumann boundary condition on this wall. All walls are assumed to be thermally adiabatic.

The computational time step was fixed at $\Delta t/(D/U_\infty) = 2.2 \times 10^{-4}$ in all calculations with the coarse mesh. All simulations were initialized with a uniform flow everywhere in the domain. After 10 flow-through times (L/U_∞), the flow was observed to be free from the initial transient and deemed fully developed. After this initial transient, the flow statistics were accumulated over additional 10 flow-through times.

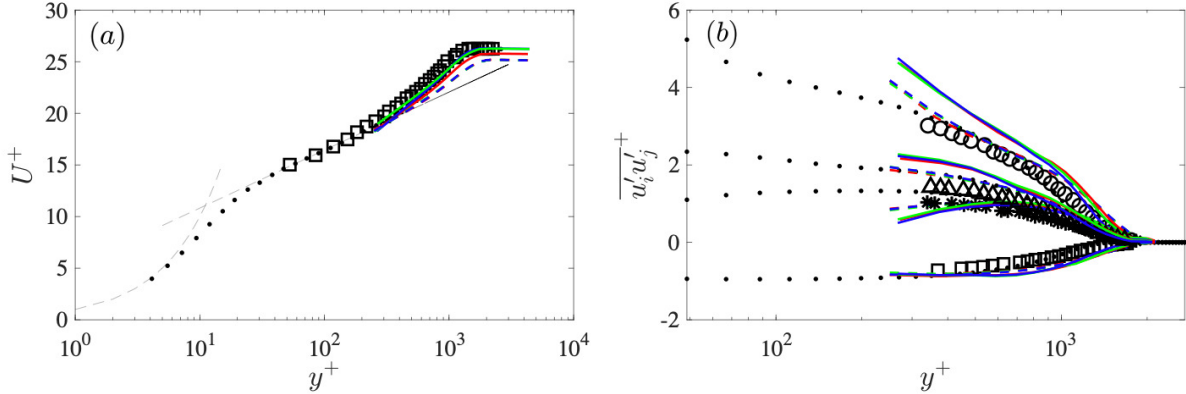


Figure 2.4: (a) Mean velocity profile at the first measurement station in the experiment (station 0: $x' = 826$ mm). Black squares are from the experiment. Black dots, WRLES by Schlatter et al. (2010) at the same Reynolds number ($Re_\theta = 4100$); red, equilibrium wall model; blue, PDE nonequilibrium wall model; green, integral nonequilibrium wall model (solid lines represent coarse mesh results; dashed lines represent fine mesh results). Black dashed lines denote the law of the wall (viscous sublayer: $u^+ = y^+$; log-law: $u^+ = \frac{1}{0.41} \log y^+ + 5.2$). (b) Reynolds stress profiles at the first measurement location (station 0: $x' = 826$ mm). Big symbols are from the experiment : circles, $\overline{u'u'}$; stars, $\overline{v'v'}$; triangles, $\overline{w'w'}$; squares, $\overline{u'v'}$. Different lines and dots have the same denotations as in (a).

2.3. Flow solver and subgrid scale (SGS) / near-wall modeling

The simulations were performed with CharLES, an unstructured cell-centered finite-volume compressible LES solver developed at Cascade Technologies, Inc. The solver employs an explicit third-order Runge-Kutta (RK3) scheme for time advancement and a second-order central scheme for spatial discretization. More details regarding the flow solver can be found in Khalighi et al. (2011) and Park and Moin (2016a). The Vreman model (Vreman, 2004) is used to close the SGS stress and heat flux. In the following section 2.8, the effect of SGS stress models is discussed along with the results obtained with the dynamic Smagorinsky model and dynamic tensor-coefficient Smagorinsky model (Moin et al., 1991; Lilly, 1992; Agrawal et al., 2022).

In the present work, the location at which the wall-models take input from the LES (matching height, denoted as $h_{wm}(x)$) is fixed across different grid resolutions by setting it to the centroids of the third off-wall cells or the top faces of the fifth off-wall cells in the coarse and fine meshes, respectively, corresponding to $10^3 h_{wm}/D = 3 \sim 7$ or $h_{wm}^+ = 175 \sim 375$ in inner units. This

has effect of fixing the wall-modeled regions in LES during grid refinements, so that improvement in LES prediction is not associated with the change in wall-modeling details, but it is attributed largely to the grid adaptation. This choice is also motivated by our experience with the flow solver, where restricting h_{wm} to the first off-wall cell or in the buffer layer produced nontrivial log-layer mismatch in channel flow calculations, even with the filtration of the wall-model input as suggested in Yang et al. (2017) for a structured pseudospectral/finite-difference code. Owen et al. (2020) reported a similar need for using the LES velocity further away from the wall in their finite-element based WMLES of channel and wall-mounted hump. Readers are referred to following section 2.9, where additional accounts on the matching height are provided along with numerical experiments to examine the effect of varying matching height on the prediction of mean three dimensionality.

The three wall models considered in the present study are: an equilibrium stress model (EQWM) in the form of ordinary differential equations, an integral nonequilibrium wall model (integral NEQWM) that solves the vertically-integrated Navier-Stokes equations, and a PDE nonequilibrium wall model (PDE NEQWM) that retains the complexity of the full Navier-Stokes equations. All three wall models parameterize the unresolved turbulence in the wall-model domain in a statistical sense using simple RANS models based on the mixing-length formulation. Note that the EQWM and PDE NEQWM have previously been implemented in CharLES, and they were tested extensively through various studies (Park and Moin, 2014, 2016a,b; Park, 2017; Bodart and Larsson, 2012). The integral NEQWM was recently integrated into CharLES, the implementation aspects of which will be discussed in a future article (Hayat and Park, 2021). A brief description of each of these models is given below.

The EQWM (Kawai and Larsson, 2012; Bodart and Larsson, 2011) solves the simplified boundary layer equations which account only for the wall-normal diffusion.

$$\frac{d}{d\eta} \left[(\mu + \mu_t) \frac{du_{||}}{d\eta} \right] = 0, \quad (2.1)$$

$$\frac{d}{d\eta} \left[(\mu + \mu_t) u_{||} \frac{du_{||}}{d\eta} + (\lambda + \lambda_t) \frac{dT}{d\eta} \right] = 0, \quad (2.2)$$

where η is the local wall-normal coordinate, $u_{||}$ is the wall-parallel velocity magnitude, T is the temperature, μ is the molecular viscosity, λ is the molecular thermal conductivity, and μ_t and λ_t are the turbulent eddy viscosity and conductivity, respectively. It should be noted that $\text{Ma} = 0.2$ in the simulations (the Mach number was not reported in the experiment, the authors of the experiment clearly assumed the flow was incompressible). Although the energy equation is solved, variations of thermodynamic variables are very small, and the energy equation does not play an important role in the present study. The velocity vector is assumed to be aligned with the LES velocity at the matching height. Owing to this intrinsic assumption, the equilibrium wall model is incapable of predicting skewed velocity profiles within the wall-modeled domain. Also, due to the unidirectionality and the condition $\mu + \mu_t > 0$, the EQWM can represent monotonic velocity profiles only, and it cannot predict velocity profiles with sign changes in the slope as found in the near-wall regions of separated shear layers. The wall-model eddy viscosity μ_t is based on the following mixing-length formula,

$$\mu_t = \kappa \rho y \sqrt{\frac{\tau_w}{\rho}} D, \quad D = [1 - \exp(-y^+/A^+)]^2. \quad (2.3)$$

On the other hand, the PDE NEQWM (Park and Moin, 2014, 2016a) solves the full 3D unsteady RANS equations,

$$\frac{\partial \rho}{\partial t} + \frac{\partial \rho u_j}{\partial x_j} = 0, \quad (2.4)$$

$$\frac{\partial \rho u_i}{\partial t} + \frac{\partial \rho u_i u_j}{\partial x_j} + \frac{\partial p}{\partial x_i} = \frac{\partial \tau_{ij}}{\partial x_j}, \quad (2.5)$$

$$\frac{\partial \rho E}{\partial t} + \frac{\partial (\rho E + p) u_j}{\partial x_j} = \frac{\partial \tau_{ij} u_i}{\partial x_j} - \frac{\partial q_j}{\partial x_j}, \quad (2.6)$$

where ρ is the density and u_i is the velocity component, p is pressure and $E = p/[\rho(\gamma - 1)] + u_k u_k/2$ is the total energy. The stress tensor and heat flux are given by, $\tau_{ij} = 2(\mu + \mu_t) S_{ij}^d$ and $q_j = -(\lambda + \lambda_t) \frac{\partial T}{\partial x_j}$. For the RANS closure, a novel mixing-length model is used, which dynamically accounts for the resolved Reynolds stresses carried by the wall model (Park and Moin, 2014). The wall-model mesh for the PDE NEQWM has the same wall-parallel grid content as in the coarse LES

mesh, but it is refined in the wall-normal direction to resolve the viscous sublayer.

Lastly, the integral NEQWM formulation solves a similar set of equations as the PDE NEQWM, albeit in a wall-normal integrated form. Currently, this formulation is limited to incompressible flows, and therefore the energy equation is not solved. For the sake of brevity, only the 2D formulation (the wall-normal and one wall-parallel velocity components) is presented below, and the reader is referred to Yang et al. (2015) for the details of full 3D formulation. The vertically integrated momentum equation is given by,

$$\frac{\partial}{\partial t} \int_0^{h_{wm}} u dy + \frac{\partial}{\partial x} \int_0^{h_{wm}} u^2 dy - U_{LES} \frac{\partial}{\partial x} \int_0^{h_{wm}} u dy = \frac{1}{\rho} \left[-\frac{\partial p}{\partial x} h_{wm} + \tau_{h_{wm}} - \tau_w \right], \quad (2.7)$$

where x and y represent the local wall-parallel and wall-normal coordinates, h_{wm} is the matching height, U_{LES} is the time-filtered velocity from the LES solution at the matching location. $\tau_w = \mu \frac{\partial u}{\partial y} \Big|_{y=0}$ and $\tau_{h_{wm}} = (\mu + \mu_t) \frac{\partial u}{\partial y} \Big|_{y=h_{wm}}$ are the shear stresses at the wall and at the matching location, respectively. The integral terms are evaluated by assuming an analytical composite profile for the velocity within the wall model, which has the form:

$$u = u_\tau \frac{y}{\delta_i} = \frac{u_\tau^2}{\nu} y, \quad 0 \leq y \leq \delta_i, \quad (2.8)$$

$$u = u_\tau \left[\frac{1}{\kappa} \log \frac{y}{h_{wm}} + C \right] + u_\tau A \frac{y}{h_{wm}}, \quad \delta_i < y \leq h_{wm}, \quad (2.9)$$

where the unknown parameters A , C , u_τ and δ_i are determined from the solution of equation (2.7) along with suitable matching and boundary conditions. For the full 3D formulation consisting of two wall-parallel velocity components, like the one employed for the present study, the composite profiles have a total of 11 unknown parameters. This approach attempts to model the effects of pressure gradient and advection through the last term in Eq. (2.9) representing linear departure from the log law.

It is worth mentioning here that in the original 3D formulation in Yang et al. (2015), the as-

sumed form of the viscous-sublayer velocity profiles in the two wall-parallel directions (Eq. (C5) in Yang et al. (2015)) resulted in inconsistent asymptotic behavior of velocity near the wall. This made the wall-stress predictions of the wall model highly sensitive to the choice of the local x/z coordinate axes. In our current integral NEQWM formulation, we modify the assumed viscous-sublayer profile to ensure consistent near-wall asymptotic behavior as given by the Taylor series expansion. The modified formulation is briefly described in the following section 2.10, and its details along with its implementation in an unstructured solver are presented in Hayat and Park (2021). A MATLAB implementation for the EQWM and the modified integral NEQWM is available on GitHub at <https://github.com/imranhayat29/Wall-Models-for-LES>.

A remark is in order regarding the overall cost of simulations with different wall models. The computational costs of the three wall models were compared by running the simulations on the fine LES mesh with 256 CPU cores for three convective flow-through times. When the cost of the simulation without any wall model (no-slip LES) is taken as the unity, the simulation costs are 1.27, 1.2, and 2.2 with the EQWM, the integral NEQWM, and the PDE NEQWM, respectively. The higher cost with the PDE NEQWM is due to the inversion of a large linear system required as a part of implicit time advancement.

2.4. Flow statistics

Results from the WMLES simulations are discussed in this section. Overall characteristics of the flow are first highlighted from the instantaneous flow field standpoint. Mean and turbulence statistics obtained with different wall models are then assessed against the experimental data. Furthermore, the three-dimensionality of the outer portion of the boundary layer is examined with the aid of Reynolds stress anisotropy and the Johnston triangular plot.

Some remarks are in order concerning the ways the main results are presented in this paper. The primary interest of the experiment was to examine the effect of the mean three dimensionality in the absence of strong streamwise pressure gradient. To this end, the experiment presented the key flow statistics along the floor centerline, where the axial pressure gradient was observed to be nearly zero. It should be noted, however, that the mean-flow trajectory near the wall deviates somewhat

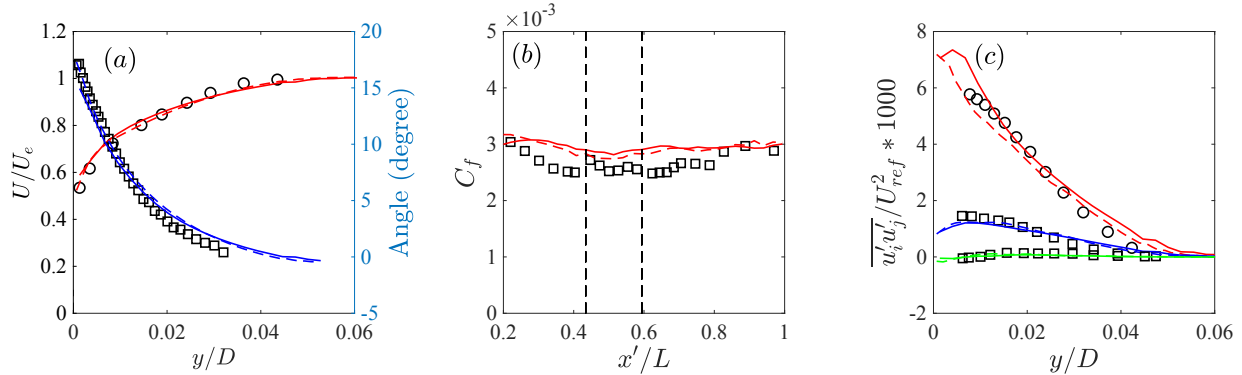


Figure 2.5: Grid convergence of the EQWM LES. (a) Blue, mean-flow direction vs. distance from the wall; red, mean velocity magnitude profile, (b) Centerline distribution of the skin-friction coefficient, and (c) Reynolds-stress profiles. Red, $\overline{u'u'}$; blue, $-\overline{u'v'}$; green, $\overline{v'w'}$. Solid lines, coarse grid; dashed line, fine grid. Profiles in (a) and (c) are at $x' = 1875$ mm (station 8). Black vertical dashed lines in (b) denote the start and end of the bend region.

substantially from the centerline as the flow passes through the bend region, as observed from the instantaneous flow field (Fig. 2.6) and the near-wall streamlines (Fig. 2.9(b)). This leaves some ambiguity in the interpretation of the statistics presented along the centerline, because any two fluid particles on the centerline (in and after the bend region) would have traveled along different Lagrangian trajectories, experiencing different history effects (most notably, they are subject to different upstream axial/spanwise pressure gradients.) With this limitation in mind, we still choose to show our results along the centerline, as all experimental data (except the wall-pressure) were presented so.

2.4.1. Grid convergence

Figure 2.5 shows the mean-flow statistics and the Reynolds stresses at $x' = 1875$ mm (the eighth measurement station in Fig. 2.1), as well as the centerline skin-friction coefficient C_f distribution obtained from the EQWM LES with the coarse and the fine grids described in Sec. 2.1. The skin-friction coefficient is defined as,

$$C_f = \frac{\tau_w}{\frac{1}{2}\rho U_e^2} \quad , \quad \frac{U_e}{U_{ref}} = (1 - C_p)^{1/2}, \quad (2.10)$$

where $\tau_w = \sqrt{\tau_{w,x}^2 + \tau_{w,z}^2}$ is the magnitude of the mean wall shear stress vector, and U_e is the local freestream velocity. The pressure coefficient is defined as

$$C_p = \frac{p - p_{ref}}{\frac{1}{2}\rho U_{ref}^2}. \quad (2.11)$$

Following the experiment, p_{ref} is the static pressure at $x' = 0$ mm, and U_{ref} is the freestream velocity at $x' = 826$ mm (defined at the spanwise centerline). Although only the EQWM results are shown here for brevity, it is noted that the other two wall models exhibited similar grid-convergence characteristics. In Fig. 2.5(a), both the mean velocity and the mean-flow direction (defined by the angle between the mean velocity vector and the freestream velocity vector) profiles obtained from the coarse-grid calculation are already in good agreement with the experiment, and the results only improve marginally with the grid refinement. More importantly, this points toward the grid convergence of the results for the refinement level used in this study. Figure 2.5(b) shows the skin-friction distribution along the centerline of the duct. Between the first and the last measurement stations, we observe a reasonably converged C_f , with the fine-grid calculation producing slight improvement in C_f . In Fig. 2.5(c), a similar trend is observed for all the Reynolds stress components shown, with the exception of the streamwise component of the Reynolds normal stress, which shows noticeable variation with grid refinement in the near-wall region; however, the Reynolds stresses in the outer portion of the boundary layer have largely converged. Having established reasonable evidence of grid-convergence for most of the flow statistics on the coarse grid, the remainder of this paper will focus largely on discussing the results obtained with the coarse grid unless stated otherwise.

2.4.2. Instantaneous flow field

Figure 2.6 visualizes the vortical structures in the floor boundary layer. Near the inlet (approximately within 20 times the inlet boundary-layer thickness from the inlet), structures with less coherence resulting from the synthetic inflow turbulence generation are observed. The floor boundary layer then gradually develops into a coherent fully developed state far upstream of the bend region, which is also verified by the velocity profile at $x' = 826$ mm (Fig. 2.4) following the typical

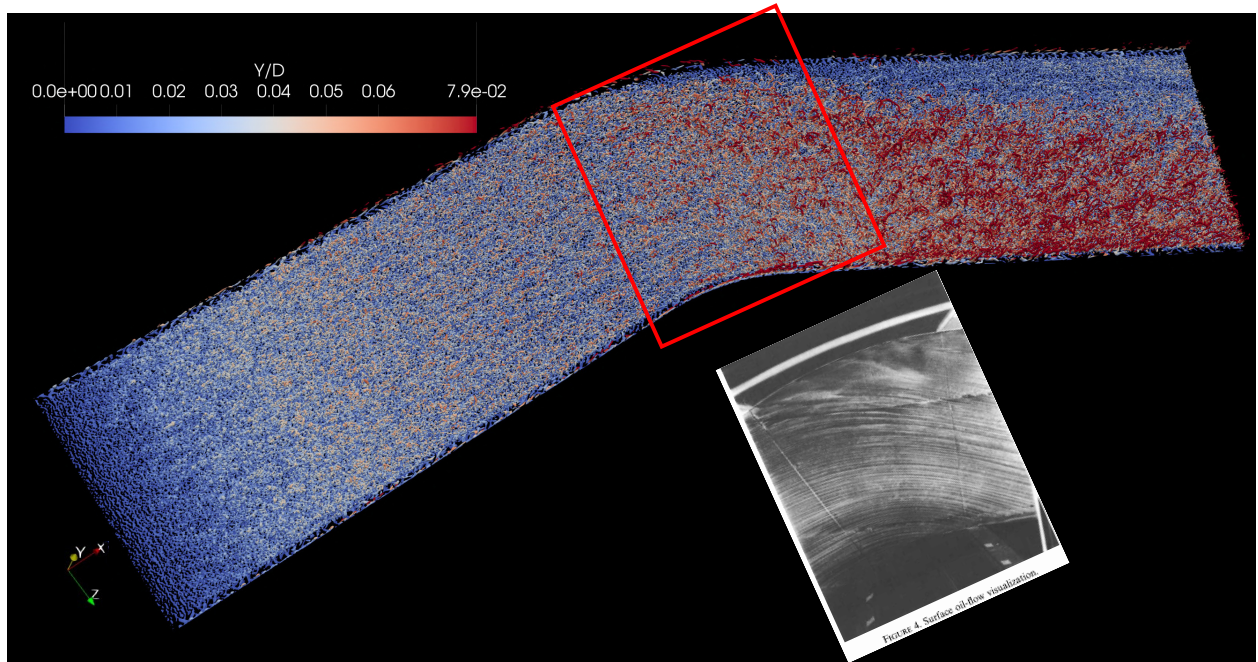


Figure 2.6: Visualization of the near-wall vortical structures using the isosurfaces of Q ($Q = Q_{rms}$, where Q is the second invariant of the velocity gradient tensor), colored by the distance from the floor of the duct. Flow is from the bottom left to the top right. Surface oil visualization from the experiment (Schwarz and Bradshaw, 1994) is shown in the inset (figure reprinted with permission from Schwarz and Bradshaw (1994)).

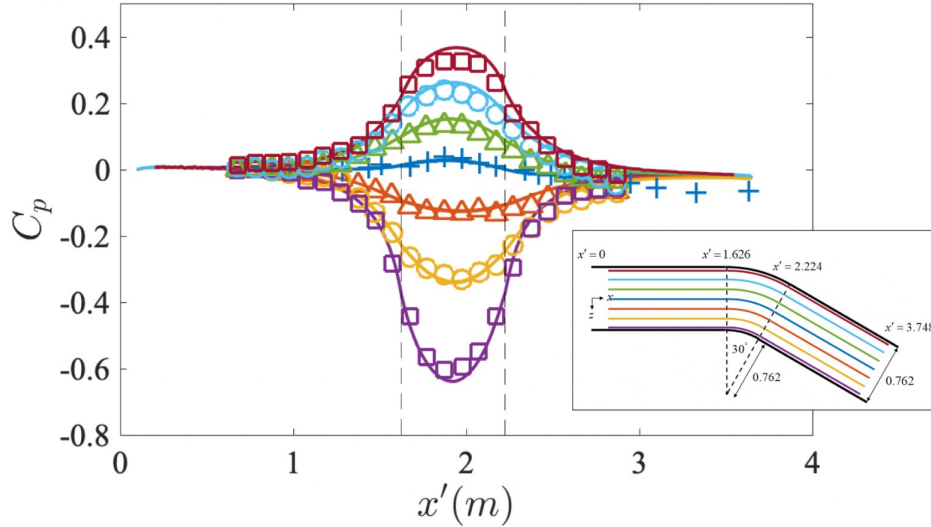


Figure 2.7: Variation of the wall-pressure coefficient from coarse EQWM simulation (results from the other wall models and resolutions are almost identical). Symbols are from the experiment. Colors denote different spanwise locations corresponding to the inset figure. z' : 0 mm, ± 127 mm, ± 254 mm, ± 368 mm

law of the wall observed in 2D turbulent boundary layer. When the flow enters the bend region, a clear contrast of two boundary layers with different origins (blue and red regions) are observed. The boundary layer in the red region is thicker than that in the blue region, showing that a new boundary layer is emerging from the concave sidewall within the bend region (at $z < 0$) and the original boundary layer developed from the upstream section is turning rapidly toward the convex side (at $z > 0$). This overall flow behavior is visually in fair agreement with the surface oil visualization in the experiment as shown in the inset in Fig. 2.6.

2.4.3. Mean-flow statistics

The cross-stream pressure gradient is the source of the mean three dimensionality in the bend region. It acts to deflect the streamlines close to the wall more strongly than those near the freestream. It is therefore important to first establish close agreement in the pressure distribution close to the bend between the simulation and the experiment. Note that in the current case without flow separation, the pressure distribution is determined largely by the wall geometry and the inviscid effect, presumably unaffected by the wall-modeling details. Figure 2.7 shows the distribution of the

static wall-pressure coefficient on the floor of the duct. The wall-pressure probing lines are parallel to the duct centerline as shown in the inset figure. The figure shows good agreement between the simulation and the experiment, except in the recovery region downstream of the bend. The axial pressure gradient is almost zero along the centerline. On the other hand, a significant spanwise pressure gradient starts to develop upstream of the bend, reaches a maximum within the bend region, and eventually decays to zero downstream of the bend. The reason for disagreement in the recovery region remains unclear to us. While C_p in the experiment remains to be slightly negative near the outlet, C_p in the simulation naturally vanishes to its upstream zero value as the flow relaxes back to its 2D ZPG state. Note that the experiment reported only the centerline distribution in this region, and that extending the duct further downstream in the simulation did not change the trend.

Figure 2.8 shows the distribution of the skin-friction coefficient along the duct centerline. The centerline mean-flow is expected to be agreeing well with the canonical ZPG 2DTBL in this region. A deviation of the skin friction from the ZPG 2DTBL near the inlet is the artifact of the inflow treatment. Note that the synthetic inflow turbulence generation methods when applied to DNS or wall-resolved LES of low Reynolds number are known to produce a development length of $10 \sim 20$ initial boundary layer thicknesses (δ_{in}), through which coherence-lacking artificial structures mature into fully-developed turbulence (e.g., Patterson et al. (2021); Sandberg (2012); Larsson (2021) where $Re_\tau = 400 \sim 500$). The present high-Reynolds number case simulated with very coarse meshes produced longer development lengths ($30 \sim 40 \delta_{in}$). The flow was observed to be fully developed from slightly upstream of the first measurement station, after which the WMLES results are in reasonable agreement with the experiment as well as with an empirical correlation (Fernholz and Finley, 1996) and a wall-resolved LES of ZPG 2DTBL (Eitel-Amor et al., 2014). In Fig. 2.8(b), slight overprediction of the skin friction from WMLES is observed throughout the duct. A similar trend was reported by Cho et al. (2021), where the EQWM was used with up to 76 million control volumes in LES. It should be noted that the wall shear stresses were measured indirectly in the experiment using a Preston tube and Patel’s calibration (Patel, 1965) for a 2DTBL. Patel (1965) reported that errors as large as 6% could occur when Preston tube is used in flows with moderate streamwise

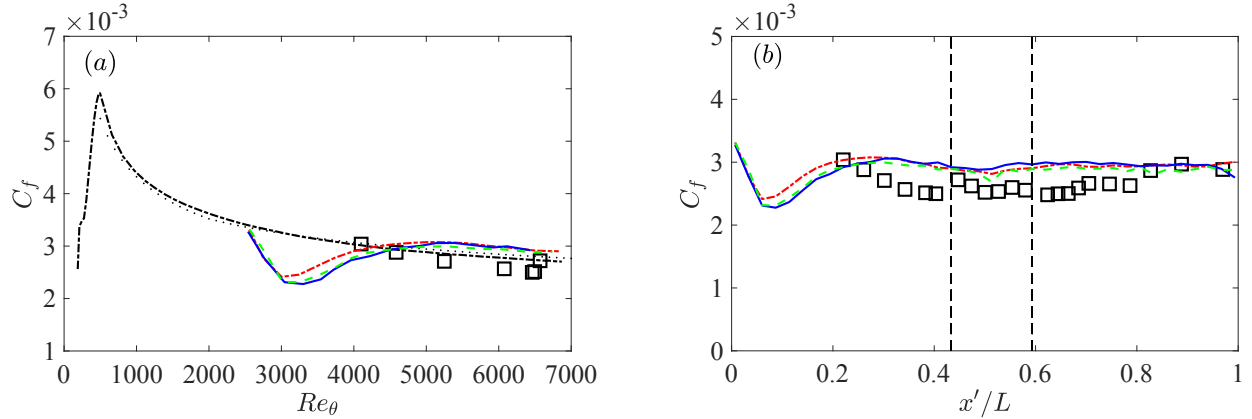


Figure 2.8: Centerline distribution of the skin-friction coefficient (C_f). (a) C_f vs. Re_θ upstream of the bend. (b) C_f vs. axial location. Squares, experiment; red dash-dotted line, EQWM; blue solid line, PDE NEQWM; green dashed line, integral NEQWM. In (a): Black dotted line, ZPGF-PBL empirical correlation (Eq. (9) in Fernholz and Finley (1996)); black dashed line, WRLES of ZPGFPBL (Eitel-Amor et al., 2014).

pressure gradient.

Next, we examine the mean three-dimensionality of the flow in the duct. The variation of the surface flow direction relative to the freestream direction is a measure of the mean-flow three-dimensionality. As shown in Fig. 2.9(a), the crossflow is almost zero in the upstream, and it grows rapidly as the flow approaches the bend. The resulting turning angle reaches the maximum near the end of the bend and decays gradually thereafter. These observations are consistent with the development of the spanwise pressure gradient. All three wall models predict the general trend in the turning-angle variation correctly; however, the PDE NEQWM gives the most accurate prediction among the three (especially within the bend region), followed by the integral NEQWM, and then the EQWM. The maximum difference between the PDE NEQWM and the EQWM is roughly 5 degrees occurring at $x'/L = 0.49$ within the bend. Note that the total flow turning is an accumulative effect of the local flow change, and the area under the curve in Fig. 2.9(a) can be thought of as an approximation of the near-wall total flow turning angle. Related to this, Fig. 2.9(b) visually highlights predictions of the near-wall flow direction by different wall models in terms of the select surface streamlines calculated from the mean wall shear-stress vector. It can be clearly seen that the flow deviates from the local centerline; however, the deviation is not predicted evenly across the different wall models,

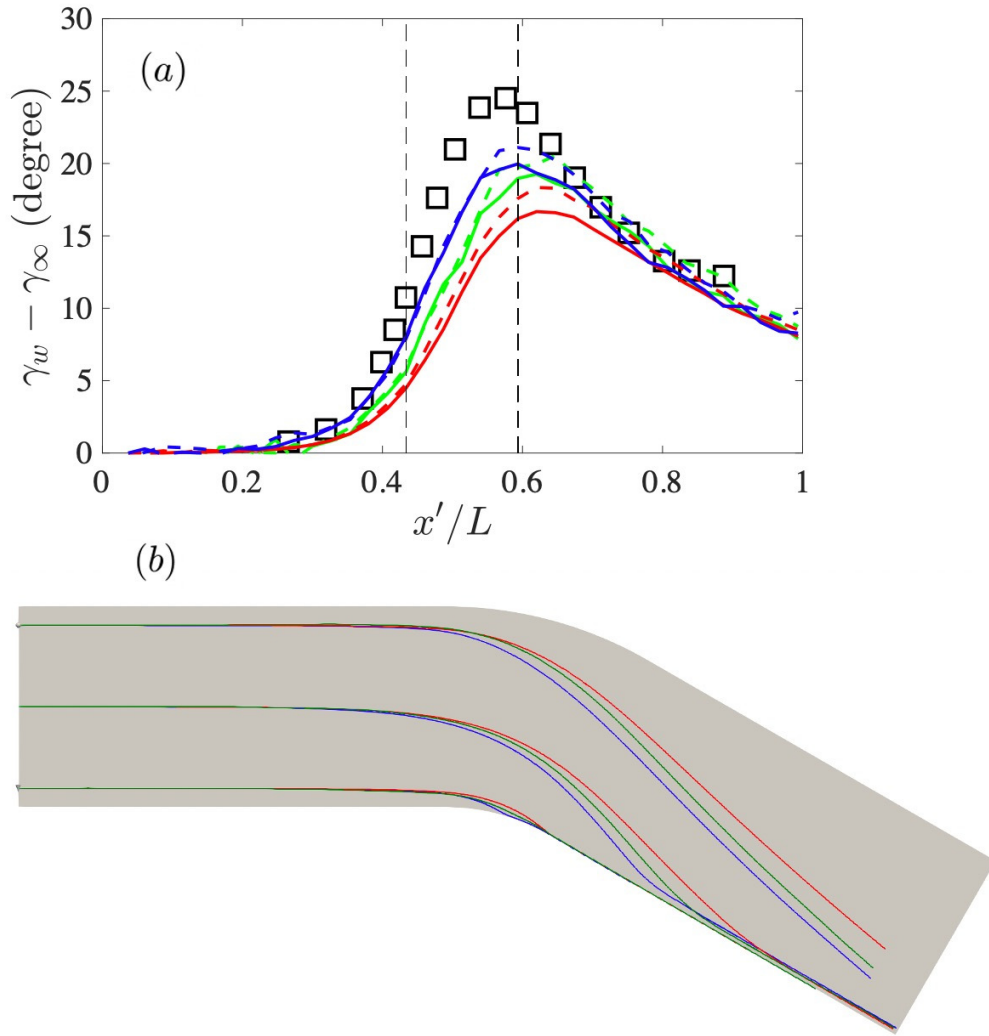


Figure 2.9: (a) Centerline distribution of the surface flow turning angles with respect to the freestream ($\gamma_w = \tan^{-1}(\tau_{w,z}/\tau_{w,x})$ is the wall shear stress direction, $\gamma_\infty = \tan^{-1}(W_e/U_e)$ is the freestream direction). (b) streamlines of wall shear stress. Squares, experiment; red line, equilibrium wall model; blue line, PDE nonequilibrium wall model; green line, integral nonequilibrium wall model. Solid and dashed lines are for coarse and fine grids, respectively.

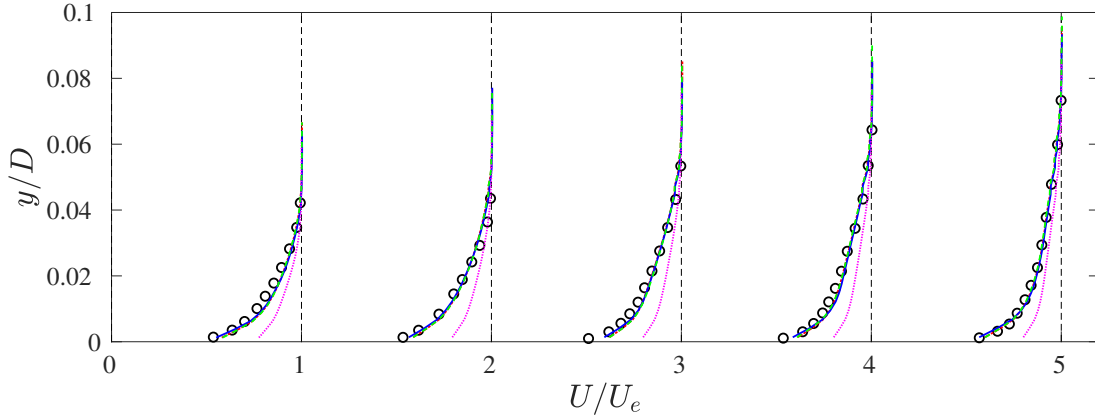


Figure 2.10: Profiles of the mean-velocity magnitude at 5 measurement locations (stations 4, 8, 12, 16, and 20, from left to right). Station 4 is upstream of the bend; station 8 is within the bend; stations 12, 16 and 20 are downstream of the bend. Red dash-dotted line, EQWM; blue solid line, PDE NEQWM; green dashed line, integral NEQWM; magenta dotted line, no-slip LES; black circle, experiment. Profiles are shifted along the abscissa by 1.

consistent with our observation in the flow turning angles in Fig. 2.9(a). The surface flow from the PDE NEQWM turns much more rapidly than that from the EQWM.

In Fig. 2.10, profiles of the mean-velocity magnitude are compared between the different wall models and the experiment, at several locations along the centerline, including upstream of, within, and downstream of the bend. It can be seen that the no-slip LES, which does not employ a wall model, gives a very poor prediction of the mean velocity. Here, a higher momentum is imparted to the boundary layer as a consequence of the underpredicted wall shear force. With the introduction of wall modeling, a significant improvement is achieved in the predicted mean-velocity profiles. In line with the predictions of the skin-friction coefficient in Fig. 2.8, the mean velocity profiles across the three wall models are almost identical. Note that here, the profiles only show the magnitude of the mean velocity, thus lacking information on the three-dimensionality of the mean-flow.

To complete this picture, Fig. 2.11 shows how the flow direction changes along the wall-normal direction. The mean-flow three-dimensionality is the strongest at the wall and becomes weaker with the increase in distance from the wall, as evident from the diminishing crossflow away from the

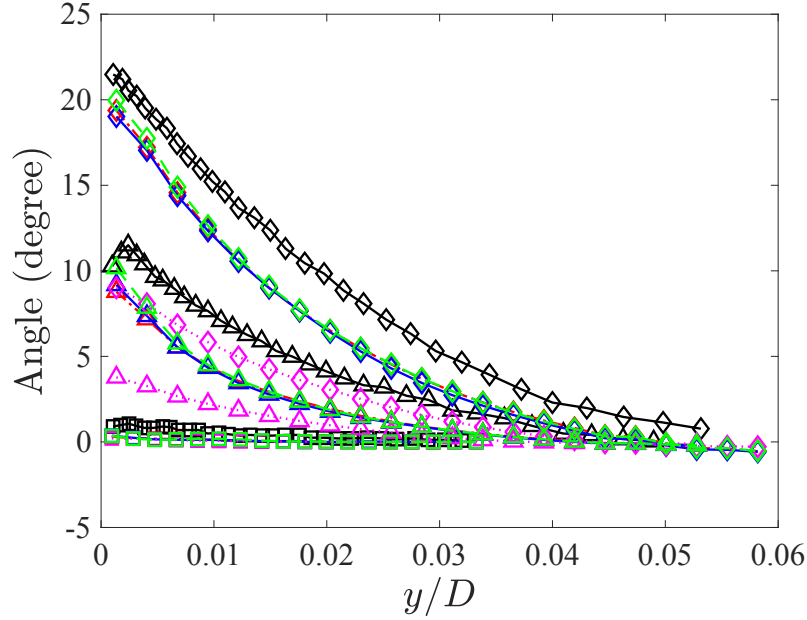


Figure 2.11: Mean-flow direction relative to the local freestream as a function of wall distance. Red dash-dotted line, EQWM; blue solid line, PDE NEQWM; green dashed line, integral NEQWM; magenta dotted line, no-slip LES; black solid line, experiment. Symbols are used to differentiate stations along the duct floor centerline only (Square, station 0; triangle, station 6; diamond, station 10). Lines with the same symbols denote the results at the same stations.

wall. A difference of approximately 3 degrees is observed between the WMLES and the experimental results. However, the predicted angles from the different wall models are almost identical, indicating that the difference in the wall-model outputs (the wall shear force direction observed in Fig. 2.9(b)) is not felt by the LES solutions away from the wall.

2.4.4. Reynolds stress

We now turn our attention to the turbulent content of the 3DTBL and its role in distinguishing this flow from the canonical 2DTBL, by examining the Reynolds stress related statistics. Indeed, the Reynolds stresses in the 3DTBL exhibit unique characteristics not seen in the 2DTBL, as we will see shortly.

Figure 2.12 shows the profiles of the Reynolds normal stresses at the same five centerline locations which were chosen to depict the mean velocity profiles. Note that the experiment did not have access to the Reynolds-stress data in the inner layer, therefore missing information on the peak values and

their locations. The no-slip LES acutely underpredicts the Reynolds normal stress, pointing towards the grid resolution being insufficient for the no-slip LES to resolve the near wall eddies. All three wall models significantly improve the prediction of the normal stresses, bringing the profiles closer to the experimental results. The predicted Reynolds normal stresses in the wall-parallel directions show remarkable agreement with the experiment, whereas those in the wall-normal direction are underpredicted near the wall. Figure 2.13 shows the profiles of the Reynolds shear stresses, where substantial improvement with wall modeling is also observed.

An important characteristic of the 3DTBL is that the Reynolds shear stress vectors are not necessarily aligned with the mean velocity gradient vectors, which challenges the fundamental assumption of the commonly used isotropic eddy viscosity model. The directions of these two vectors are characterized by the angles defined below,

$$\gamma_\tau = \tan^{-1}\left(\frac{\overline{v'w'}}{\overline{u'v'}}\right), \quad \gamma_g = \tan^{-1}\left(\frac{\partial W/\partial y}{\partial U/\partial y}\right). \quad (2.12)$$

Figure 2.14(a) clearly shows that the Reynolds shear stress vector lags behind the mean velocity gradient vector within the bend where mean-flow three-dimensionality is strongest. Downstream of the bend where mean-flow three-dimensionality declines, the difference between the two vectors also decreases (Fig. 2.14(b)). Furthermore, this lag appears to be a function of the distance from the wall. The experiment shows that the lag decreases with wall distance in the outer layer above $y/\delta_{99} \approx 0.7$ within the bend. Downstream of the bend, the Reynolds shear stress vector even starts to lead mean velocity gradient vector above $y/\delta_{99} \approx 0.8$, and this lead increases with wall distance. These behaviors and the shear-stress angles therein are not captured well in LES. We conjecture that computation of the angles in this region is prone to contamination by numerical error or measurement noise, because both the Reynolds shear stress and the mean velocity gradient values are very small there. At $y/\delta_{99} \leq 0.7$, a reasonable agreement between the simulations and the experiment is observed, and results from different wall models do not show notable difference.

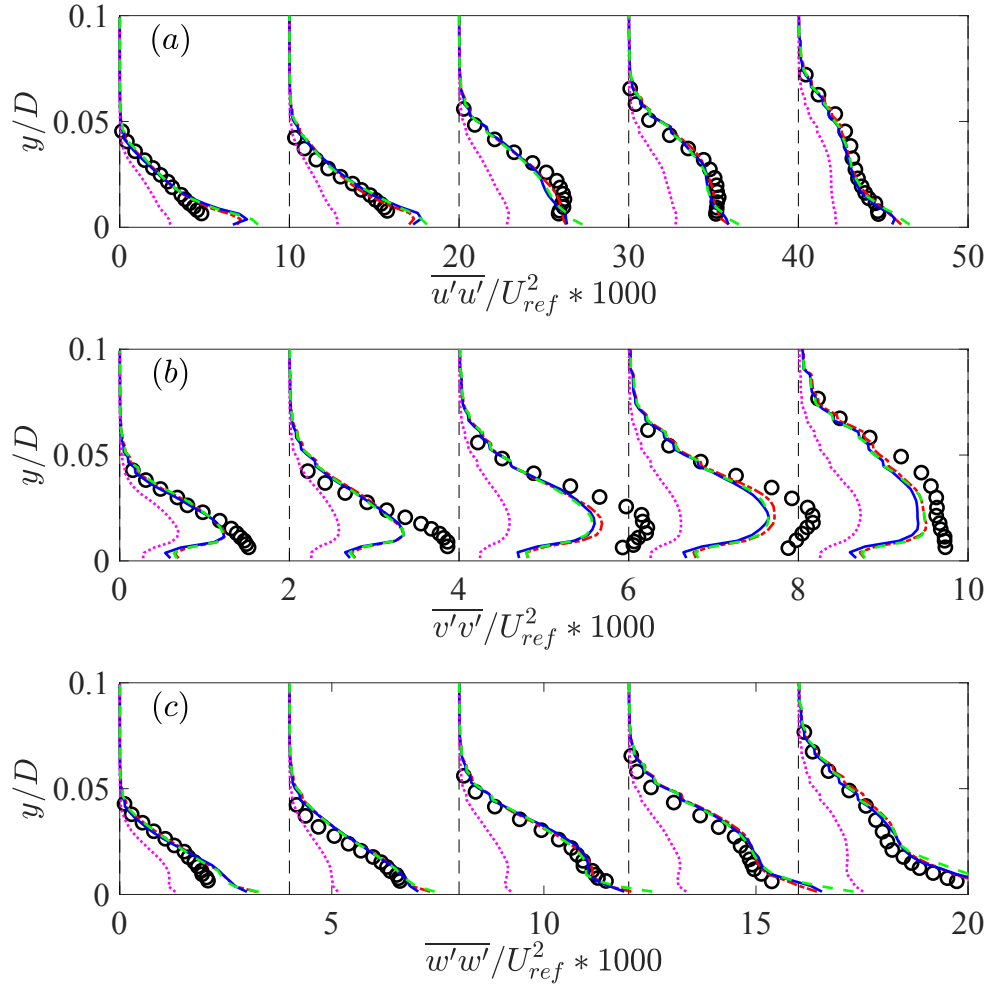


Figure 2.12: Reynolds normal stress profiles at the same five measurement stations as the mean velocity profiles in Fig. 2.10. Red dash-dotted line, EQWM; blue solid line, PDE NEQWM; green dashed line, integral NEQWM; magenta dotted line, no-slip LES; black circle, experiment. Profiles are shifted along the abscissa by multiples of 10, 2 and 4 for $\overline{u'u'}$, $\overline{v'v'}$ and $\overline{w'w'}$, respectively.

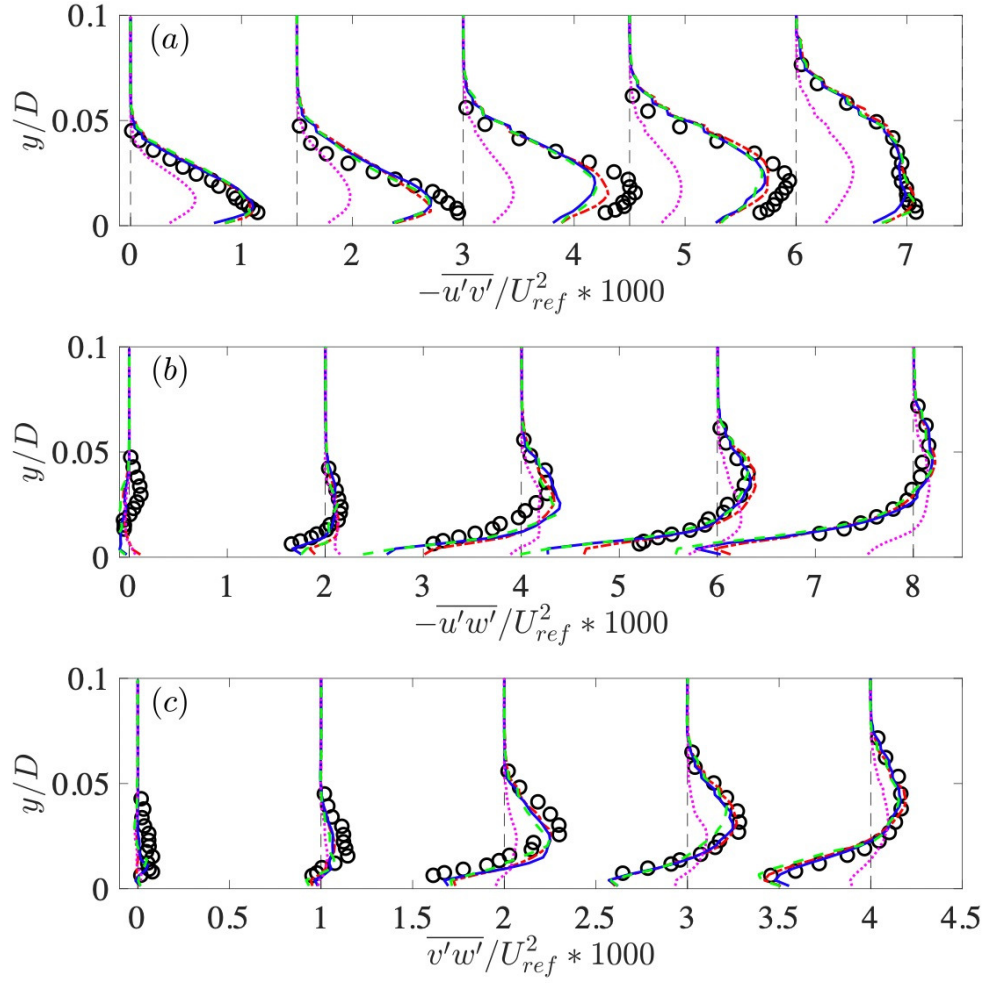


Figure 2.13: Reynolds shear stress profiles at the same five locations as the mean velocity profiles in Fig. 2.10. Red dash-dotted line, EQWM; blue solid line, PDE NEQWM; green dashed line, integral NEQWM; magenta dotted line, no-slip LES; black circle, experiment. Profiles are shifted along the abscissa by multiples of 1.5, 2 and 1 for $-\overline{u'v'}$, $-\overline{u'w'}$ and $\overline{v'w'}$, respectively.

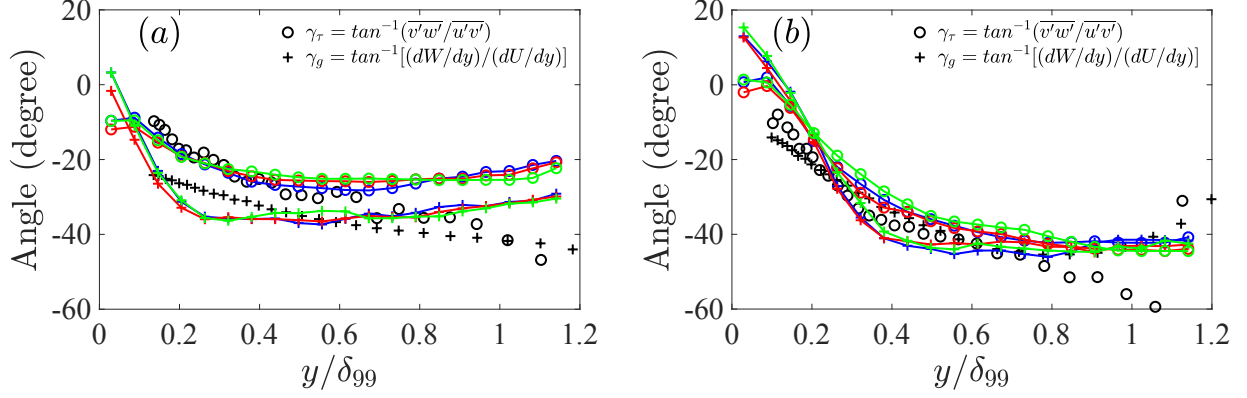


Figure 2.14: Directions (relative to the local freestream) of the mean velocity gradient vector and the Reynolds shear stress vector. (a) station 10; (b) station 17. Red, EQWM; blue, PDE NEQWM; green, integral NEQWM; black, experiment. Circle, angle between the Reynolds shear stress vector γ_τ and the local freestream; cross, angle between the mean velocity gradient vector γ_g and the local freestream.

2.5. Lumley triangle: anisotropy invariant map

We have noted that the Reynolds stresses from the simulations agree reasonably well with the experiment. This makes it possible to further investigate the anisotropy of the Reynolds stress in the outer layer of this 3DTBL using the WMLES solution. In this section, using the fine grid prediction, we employ the Lumley triangle to analyze the Reynolds-stress anisotropy. Following Pope (2000), the normalized anisotropy tensor is defined as,

$$b_{ij} = \frac{\langle u_i u_j \rangle}{\langle u_k u_k \rangle} - \frac{1}{3} \delta_{ij}. \quad (2.13)$$

The anisotropy tensor has zero trace and thus has two independent principal invariants. It is convenient to define two variables ξ and η , corresponding to the two invariants, as

$$6\eta^2 = -2I_2 = b_{ii}^2 = b_{ij}b_{ji} \quad (2.14)$$

$$6\xi^3 = 3I_3 = b_{ii}^3 = b_{ij}b_{jk}b_{ki}. \quad (2.15)$$

The state of anisotropy can be characterized by the above two variables ξ and η . All realizable Reynolds-stress states must be located within a triangular region in the ξ - η plane, which is known

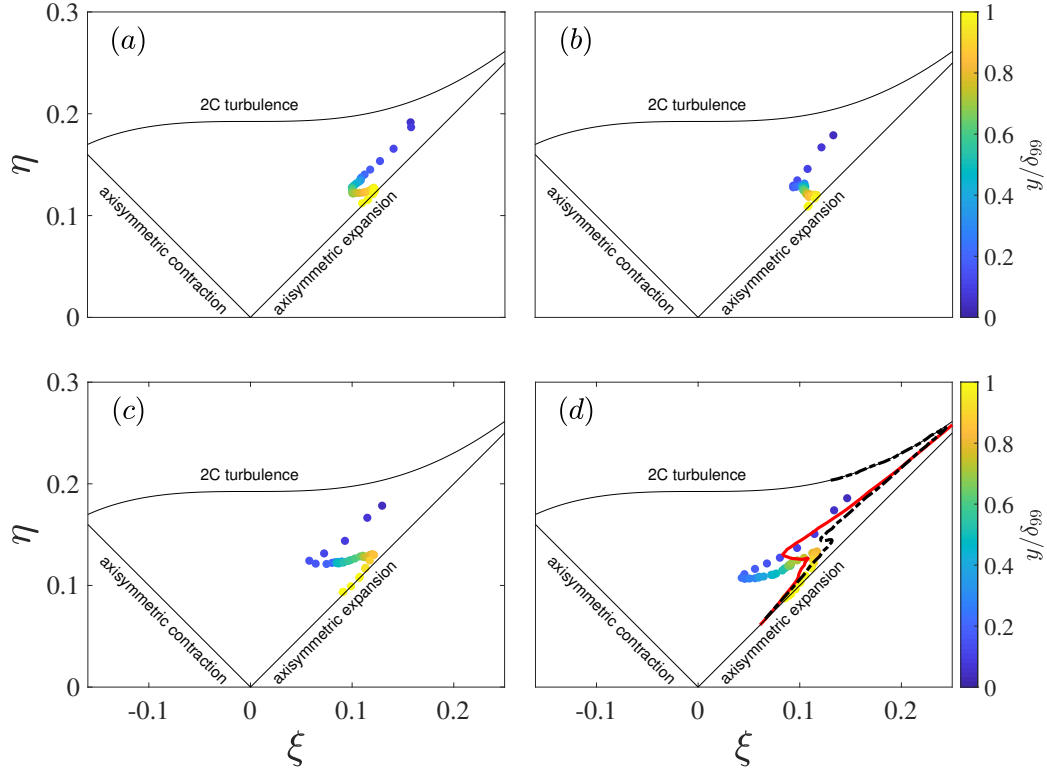


Figure 2.15: Lumley triangle of the WMLES results along the wall-normal direction. (a) station 4. (b) station 10. (c) station 12. (d) station 18. Colored dots, fine grid PDE-NEQWM result (all the wall models give almost identical results, and thus only PDE-NEQWM is shown here); black dash-dotted line, canonical 2D channel flow at $Re_\tau = 2003$ (Hoyas and Jimenez, 2006); red solid line, shear-driven 3DTBL from transient channel at $Re_\tau = 546$ at $t^+ = 192$ (Lozano-Durán et al., 2020). Colorbar denotes the wall distance normalized by the local boundary layer thickness.

as the Lumley triangle. The boundary of the Lumley triangle corresponds to some special states of the Reynolds-stress tensor: the origin corresponds to the isotropic turbulence; the left corner point corresponds to the two-component (2C) axisymmetric state; the right corner point corresponds to the one-component (1C) state; the left straight line corresponds to the axisymmetric contraction and the right straight line corresponds to the axisymmetric expansion; the top curve represents the two component (2C) turbulence.

The evolution of the Reynolds stress anisotropies through the bend is shown in Fig. 2.15. Comparisons to a statistically 2D channel flow at $Re_\tau = 2003$ (Hoyas and Jimenez, 2006) and a transient

statistically 3D channel flow at $Re_\tau = 546$ (Lozano-Durán et al., 2020) can be also made from these data shown in Fig. 2.15(d). Lozano-Durán et al. (2020) studied a transient three-dimensional channel flow, where an initially statistically one-dimensional flow in a doubly periodic channel evolves to a new state after a sudden imposition of a spanwise pressure gradient. This flow models a shear-driven 3DTBL, and it can be used for comparison to the pressure-driven case discussed in the current work. Right upstream of the bend, the wall-normal distribution of the anisotropies away from the wall shows some similarity to that in the 2D channel (Fig. 2.15(a)), exhibiting a characteristic S-shape lying close to the axisymmetric-expansion (AE) limit. As the flow passes through the bend, the left cusp of this S curve rapidly dislocates toward inside the triangle, leaving less points close to the AE limit. The non-monotonic decrease of the anisotropies (with increasing wall distance) is also observed vividly, which is only weakly present in the 2D channel. While the station 18 is considerably downstream of the bend region, the anisotropies are still seen further departing from its 2D behavior. This is consistent with the observation in Fig. 2.14 that the Reynolds stresses respond more slowly than the mean to the imposed three-dimensionality. Also, in Fig. 2.15(d), note the similarity of the anisotropy distributions in the duct and the shear-driven 3DTBL from the transient channel flow, although departure from the 2D behavior is much stronger in the duct case.

2.6. Triangular plot

In the present work, the mean three-dimensionality in the outer layer is created by the inviscid skewing mechanism, where the streamwise vorticity is produced by reorientation of the spanwise vorticity. A popular way of representing the crossflow so developed is the “Johnston triangular plot” (Johnston, 1960), which is the triangular plot of U_s against U_n , where U_s and U_n are along and normal to the local freestream direction, respectively. In particular, the outer-layer mean velocity profile of the skew-induced 3DTBLs can be accurately approximated by the Squire-Winter-Hawthorne (SWH) relation (Squire and Winter, 1951; Hawthorne, 1951; Bradshaw, 1987),

$$\frac{U_n}{U_e} = 2\gamma_e \left(1 - \frac{U_s}{U_e} \right). \quad (2.16)$$

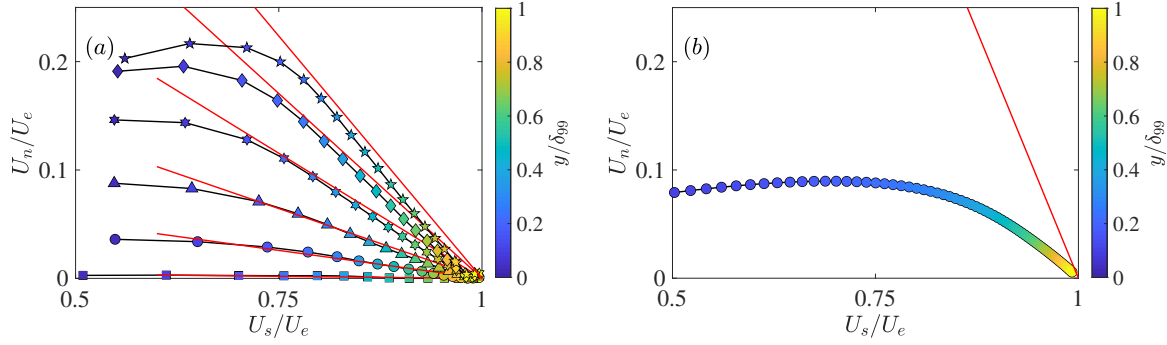


Figure 2.16: Johnston triangular plot (a) WMLES of the bent square duct (all the wall models give almost identical results, and thus only PDE-NEQWM is shown here): square, station 0; circle, station 4; triangle, station 6; cross, station 8; diamond, station 10; star, station 12. (b) DNS of the shear-driven 3DTBL from the transient channel flow at $Re_\tau = 546$ at $t^+ = 192$ (Lozano-Durán et al., 2020). Red straight line, the SWH formula Eq. (2.16). Colorbar denotes the wall distance normalized by the local boundary layer thickness.

where γ_e is the freestream turning along the streamline. This is a special case of the vorticity transport equation in which viscous terms and Reynolds stresses are neglected. The SWH relation shows up as a straight line with a negative slope toward the right end of the triangular plot. In Fig. 2.16, we present the mean velocity for the current bent duct flow and a temporally developing shear-driven 3D channel flow from Lozano-Durán et al. (2020) in the triangular plot. It is observed that the mean velocities in the outer layer from the duct flow satisfy the SWH formula well, whereas they deviate from the SWH relation in the shear-driven case, as expected. The slope in the SWH relation represents the freestream turning angle with respect to the upstream flow, and the freestream slope in the triangular plot (Fig. 2.16(a)) therefore increases toward the downstream direction.

The wall model solutions (defined only close to the wall) are also visualized along with the outer LES solution in Fig. 2.17. It gives us a vivid picture of different wall models' capabilities to depict skewed mean-velocity profiles. In the triangular plot, the wall model solutions are from the origin to the 3rd cell LES solutions (coarse grid resolution). The EQWM, due to its unidirectional assumption, cannot describe skewed mean-velocity profiles, and it shows up as a straight line starting from the origin in the triangular plot. On the other hand, the PDE NEQWM and the integral NEQWM are able to represent skewed mean-velocity profiles. They show up as curved lines in the triangular plot,

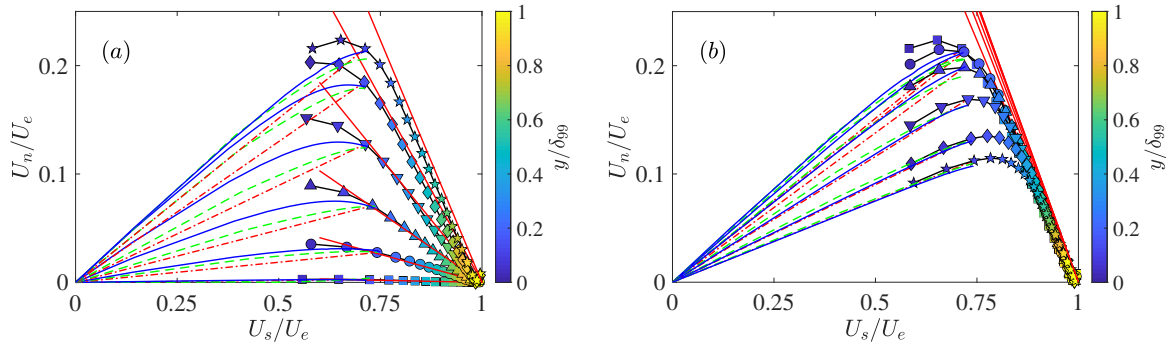


Figure 2.17: Johnston triangular plot of LES and wall-model solutions. (a) Crossflow developing stage: square, station 0; circle, station 4; triangle, station 6; cross, station 8; diamond, station 10; star, station 12. (b) Crossflow decaying stage: square, station 12; circle, station 14; triangle, station 16; cross, station 18; diamond, station 20; star, station 21. Red solid straight line, relation given by the SWH formula (Eq. (2.16)); red dash-dotted line, EQWM; blue solid line, PDE NEQWM; green dashed line, integral NEQWM. Lines with symbols represent the WMLES solution similar to Fig. 2.16(a). Colorbar denotes the wall distance normalized by the local boundary layer thickness.

implying that the flow direction changes with the wall distance. During the crossflow developing stage (Fig. 2.17(a)), the difference between the two NEQWM solutions and the EQWM solution gradually grows. Notice that the PDE NEQWM is able to represent a richer variation of the slope (flow direction) along the wall-normal direction than the integral NEQWM. During the crossflow decaying stage (Fig. 2.17(b)), the difference among three wall model solutions gradually decreases. All three wall model solutions become almost unidirectional close to the end of the duct.

2.7. Quantification of the nonequilibrium contributions to the wall shear stress direction

In this section, the nonequilibrium effects neglected in the EQWM are analyzed through the full RANS equations used in the nonequilibrium wall models. This analysis highlights the importance of accounting for the nonequilibrium effects in wall modeling for accurate prediction of the surface flow direction, as well as the subtle difference in how these effects are incorporated in different wall models. Our analysis is based on the solutions of the PDE NEQWM and the integral NEQWM. Ideally, this analysis should be done in a priori sense utilizing the fully resolved flow fields, as attempted in Hickel et al. (2012). This was deemed infeasible in the present case due to the high Reynolds number.

Assuming incompressible flow, the time-averaged momentum equations in the PDE NEQWM can be recasted as

$$\frac{\partial}{\partial y}[(\nu + \nu_t) \frac{\partial \langle u \rangle}{\partial y}] = S_x \quad (2.17)$$

$$\frac{\partial}{\partial y}[(\nu + \nu_t) \frac{\partial \langle w \rangle}{\partial y}] = S_z, \quad (2.18)$$

where S_x and S_z are the nonequilibrium source terms comprising the following terms ($S = A + P - D$),

$$\text{advection } A_x = \frac{\partial \langle u \rangle^2}{\partial x} + \frac{\partial \langle u \rangle \langle v \rangle}{\partial y} + \frac{\partial \langle u \rangle \langle w \rangle}{\partial z} + \frac{\partial \langle u' u' \rangle}{\partial x} + \frac{\partial \langle u' v' \rangle}{\partial y} + \frac{\partial \langle u' w' \rangle}{\partial z} \quad (2.19)$$

$$\text{advection } A_z = \frac{\partial \langle w \rangle^2}{\partial z} + \frac{\partial \langle v \rangle \langle w \rangle}{\partial y} + \frac{\partial \langle u \rangle \langle w \rangle}{\partial x} + \frac{\partial \langle w' w' \rangle}{\partial z} + \frac{\partial \langle v' w' \rangle}{\partial y} + \frac{\partial \langle u' w' \rangle}{\partial x} \quad (2.20)$$

$$\text{pressure gradient } P_x = \frac{1}{\rho} \frac{\partial \langle P \rangle}{\partial x} \quad (2.21)$$

$$\text{pressure gradient } P_z = \frac{1}{\rho} \frac{\partial \langle P \rangle}{\partial z} \quad (2.22)$$

$$\text{lateral diffusion } D_x = \frac{\partial}{\partial x}[(\nu + \nu_t) \frac{\partial \langle u \rangle}{\partial x}] + \frac{\partial}{\partial z}[(\nu + \nu_t) \frac{\partial \langle u \rangle}{\partial z}] \quad (2.23)$$

$$\text{lateral diffusion } D_z = \frac{\partial}{\partial x}[(\nu + \nu_t) \frac{\partial \langle w \rangle}{\partial x}] + \frac{\partial}{\partial z}[(\nu + \nu_t) \frac{\partial \langle w \rangle}{\partial z}] \quad (2.24)$$

By integrating Eqns. (2.17) and (2.18) twice, the following expressions of the wall shear stress for the PDE NEQWM are obtained

$$\tau_{w,x} = \frac{U_{LES} - \int_0^{h_{wm}} \frac{\int_0^y S_x dy}{\nu + \nu_t} dy}{\int_0^{h_{wm}} \frac{1}{\nu + \nu_t} dy}, \quad (2.25)$$

$$\tau_{w,z} = \frac{W_{LES} - \int_0^{h_{wm}} \frac{\int_0^y S_z dy}{\nu + \nu_t} dy}{\int_0^{h_{wm}} \frac{1}{\nu + \nu_t} dy}, \quad (2.26)$$

where U_{LES} and W_{LES} are the LES velocity components at the matching location. A similar expression can be found in Wang and Moin (2002). As shown in the previous sections, U_{LES} and W_{LES} are almost identical among the simulations with the different wall models. The wall shear stress direction, which is the quantity of interest exhibiting the most significant difference among

the three wall models, is then expressed as

$$\frac{\tau_{w,z}}{\tau_{w,x}} = \frac{W_{LES} - I_z}{U_{LES} - I_x}, \quad (2.27)$$

where $I_z = \int_0^{h_{wm}} \frac{\int_0^y S_z dy}{\nu + \nu_t} dy$ and $I_x = \int_0^{h_{wm}} \frac{\int_0^y S_x dy}{\nu + \nu_t} dy$. When all the nonequilibrium effects are neglected (i.e., letting $S_x = S_z = 0$), this relation reduces to the wall shear stress direction predicted by the EQWM which assumes unidirectional flow ($\frac{\tau_{w,z}}{\tau_{w,x}} = \frac{W_{LES}}{U_{LES}}$). The fidelity with which the constitutive terms of I_x and I_z are modeled is, therefore, crucial to the performance of wall models in predicting the surface flow direction.

To separate the nonequilibrium contributions from the flow direction predicted by the EQWM, we can first reorganize Eqn. (2.27) as

$$\frac{\tau_{w,z}}{\tau_{w,x}} = \frac{W_{LES}}{U_{LES}} \left(\frac{1 - I_z/W_{LES}}{1 - I_x/U_{LES}} \right). \quad (2.28)$$

For the present flow, it is shown in Fig. 2.18 that I_x is relatively small compared to U_{LES} , which permits the use of truncated Taylor series expansion of $\frac{1}{1 - I_x/U_{LES}}$,

$$\frac{\tau_{w,z}}{\tau_{w,x}} = \frac{W_{LES}}{U_{LES}} \left(1 - \frac{I_z}{W_{LES}} \right) \left[1 + \frac{I_x}{U_{LES}} + O\left(\frac{I_x}{U_{LES}}\right)^2 \right], \quad (2.29)$$

Equation (2.29) can be further expanded as the following expression

$$\frac{\tau_{w,z}}{\tau_{w,x}} = \frac{W_{LES}}{U_{LES}} \left(1 - \frac{I_z}{W_{LES}} + \frac{I_x}{U_{LES}} + \dots \right). \quad (2.30)$$

The terms I_x/U_{LES} and I_z/W_{LES} can be viewed as representing the corrective contributions from the nonequilibrium effects to the surface flow direction predicted by the EQWM. In essence, Eqn. (2.30) enables the surface flow angle to be decomposed into distinct contributions originating from the equilibrium and the nonequilibrium terms. Although not shown here for brevity, this truncated relation was found to provide almost identical description as the actual wall flow direction

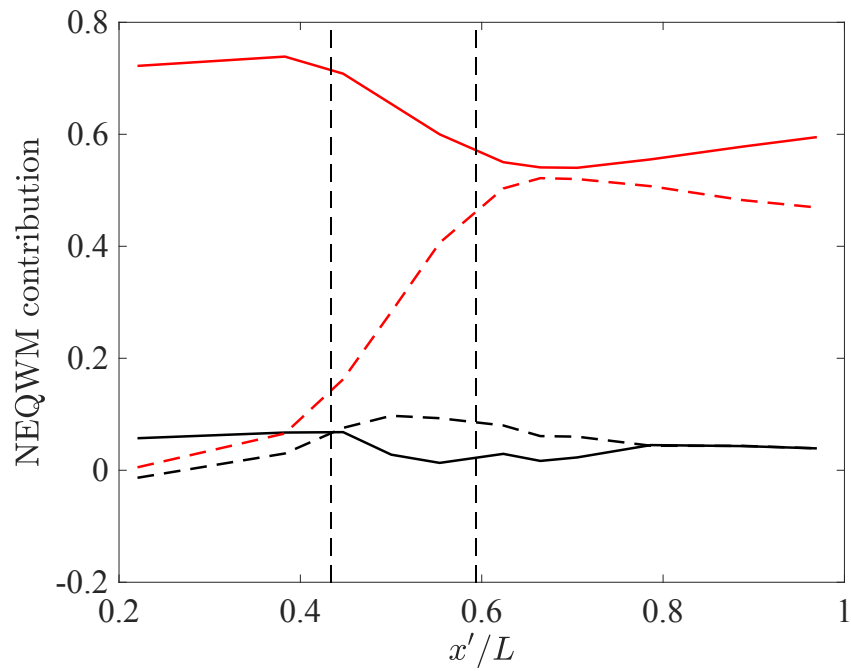


Figure 2.18: Centerline distribution of the nonequilibrium contributions (from PDE NEQWM). Red solid line, U_{LES}/U_{ref} ; red dashed line, W_{LES}/U_{ref} ; black solid line, $-I_x/U_{ref}$; black dashed line, $-I_z/U_{ref}$.

$(\tau_{w,z}/\tau_{w,x})$. Note that Eqn. (2.30) applies to the integral NEQWM as well. However, the terms I_x and I_z therein are largely modeled using the assumed velocity profile, in contrast to the PDE NEQWM where these terms are largely solved for, using the full RANS equations.

To further compare the wall models, we plot the two leading order terms of Eqn. (2.30) for the two nonequilibrium wall models in Fig. 2.19 (all nonequilibrium terms are zero for EQWM and they are not plotted.) Several interesting observations are made. First, the two nonequilibrium wall models show that the total nonequilibrium angle corrections are large at the beginning of the bend region, and that they gradually decrease to zero towards the end of the duct. That is, the nonequilibrium models properly sense the region where nonequilibrium effects are important, and attempt to model them therein. Second, the two nonequilibrium wall models produce comparable distributions of I_x/U_{LES} , implying that the axial (x) contents of the nonequilibrium effects are modeled almost identically by the two wall models. Third, the difference between the wall models appears to be concentrated in $-I_z/W_{LES}$, i.e., in the way the models sense and model the cross-flow (z) component of the nonequilibrium effects. The integral NEQWM underpredicts $-I_z/W_{LES}$ throughout the duct compared to the PDE NEQWM. Furthermore, within the bend, the signs of this term are opposite in the two wall models. This term is comprised of advection (A_z), pressure gradient (P_z), lateral diffusion (D_z), and W_{LES} . Among these terms, P_z and W_{LES} are imposed largely from the LES solution (which are seen to be identical from the simulations using the two wall models), and D is seen to be negligible in its magnitude. Therefore, we conjecture that the difference of $-I_z/W_{LES}$ in the integral wall model originates largely from its assumed velocity profile, which is directly used in computing the advection term A_z . It should be noted that the lines representing $-I_z/W_{LES}$ in Fig. 2.19 show rapid changes in the upstream region ($0.2 \leq x'/L \leq 0.4$) because the spanwise velocity W_{LES} is almost zero therein. This makes these terms ill-behaved (division by 0) in this region with extreme data range. It should also be noted that these terms will be multiplied by W_{LES}/U_{LES} in the end, as in Eq. (2.30). When W_{LES} is almost zero, the flow angle will just be zero. Therefore, the focus should be on the bend and the downstream regions.

Furthermore, the individual contribution from different nonequilibrium effects are also analyzed.

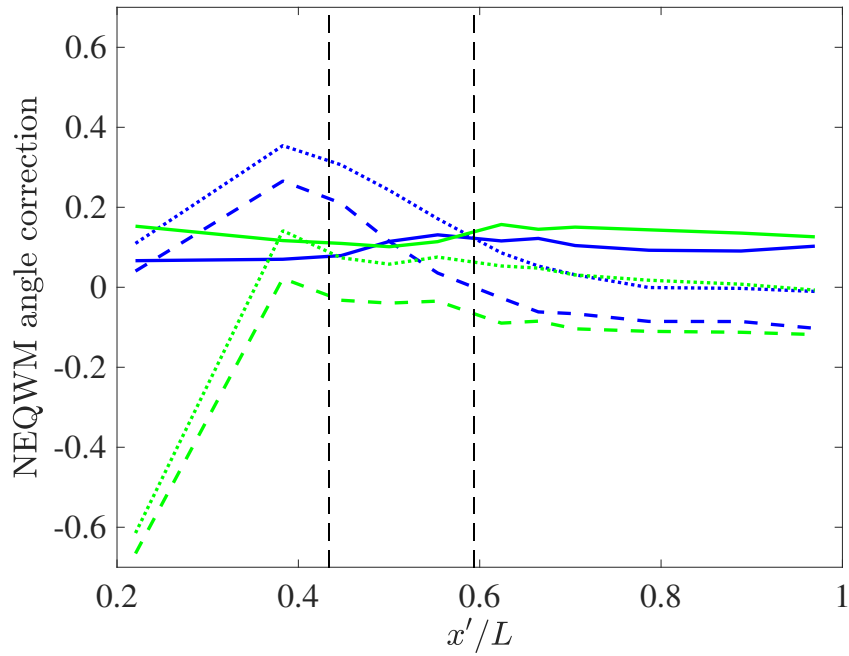


Figure 2.19: Centerline distribution of the nonequilibrium contribution to the flow direction. Solid line, I_x/U_{LES} ; dashed line, $-I_z/W_{LES}$; dotted line, total nonequilibrium correction. Blue, NEQWM; green, integral NEQWM. Black vertical dashed lines, start and end of the bend region.

Starting from Eqn. (2.27) with $I_x = I_z = 0$ (corresponding to the EQWM prediction), we examine the change in the surface flow turning angle by systematically including the contributions from various nonequilibrium effects (advection, pressure gradient, and lateral diffusion) to I_x and I_z . Note that this is done in a post-processing manner using the solution of the PDE NEQWM. The results are shown in Fig. 2.20. When all the nonequilibrium effects are taken into account, the reconstructed surface flow turning-angle agrees with the PDE NEQWM prediction, as expected. The lateral diffusion terms have negligible contributions to the surface flow turning angle. The pressure gradient and advection terms are significant within the bend, where the mean three-dimensionality develops. However, these terms appear to have a competing effect within the bend. The pressure gradient tends to make the flow deviate more from the local freestream, while the advection tends to make the flow deviate less from the local freestream. These two contributions largely cancel out each other, but a subtle balance between the two appears to be crucial in prediction of the surface flow direction.

2.8. Effects of the SGS modeling

To evaluate the effects of SGS modeling on the prediction of the mean three dimensionality, another WMLES (with EQWM) was performed with the dynamic Smagorinsky model (DSM) (Moin et al., 1991; Lilly, 1992) using the coarse mesh. Since there is no homogeneous direction available in this flow, the commonly deployed practice of averaging the model expression along the homogeneous spatial directions to regularize the behavior of the model coefficient is replaced with averaging over neighbor cells using the test filter. It was observed that the DSM produces a similar eddy viscosity field as the Vreman model does. The results of the near wall flow turning and flow direction with respect to wall distance are shown in Fig. 2.21. The DSM results are almost identical to the Vreman model results. Although not shown for brevity, similar trends were observed in all other flow statistics.

Both the Vreman model and DSM are isotropic eddy viscosity models, which assume a perfect alignment between the strain-rate tensor and the SGS stress tensor. This is likely invalid in 3DTBL, similar to the well known misalignment of the Reynolds stress tensor and the mean strain-rate

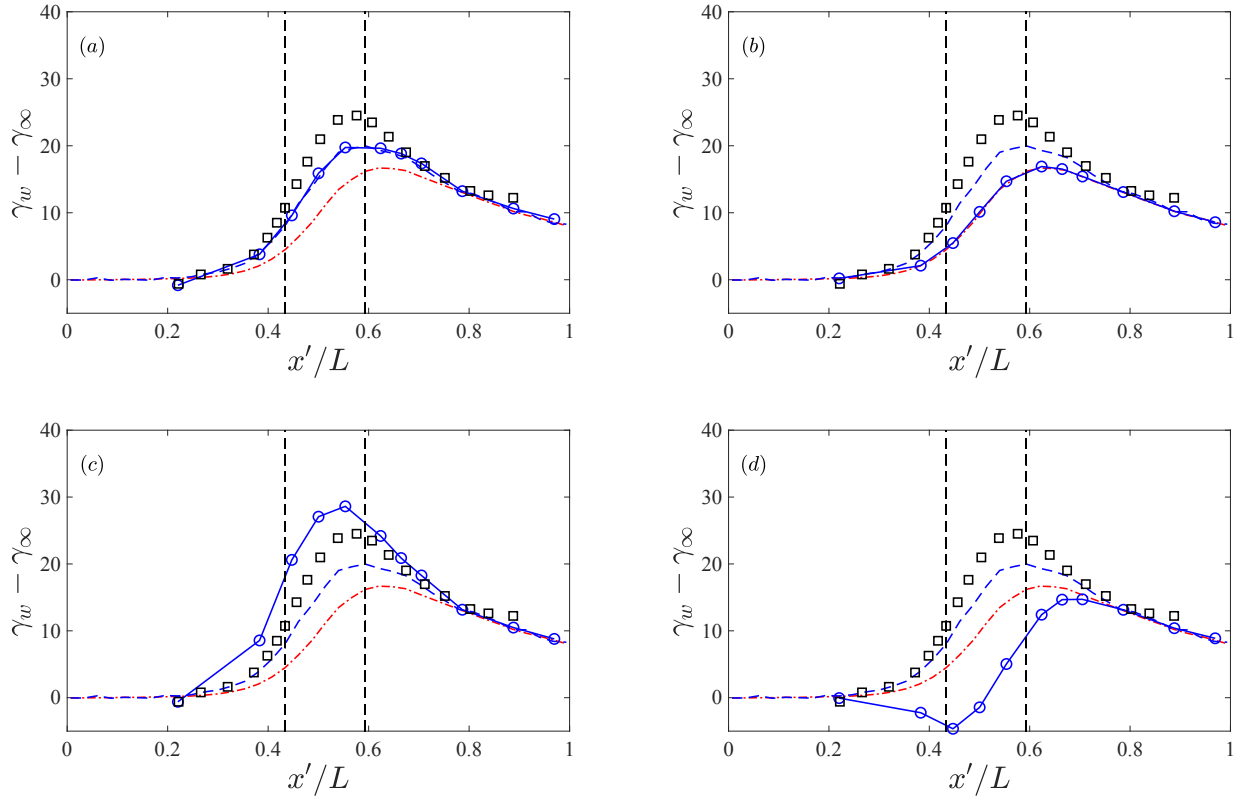


Figure 2.20: Centerline distribution of the surface flow turning angles with respect to the freestream (γ_w is the wall shear stress direction, γ_∞ is the freestream direction). (a) including all nonequilibrium effects, (b) including diffusion only, (c) including pressure gradient only, (d) including advection only. Red dash-dotted line, EQWM; blue dashed line, PDE NEQWM; blue solid line with circles, reconstruction with nonequilibrium contributions; black squares, experiment; black vertical dashed line, start and end of the bend region.

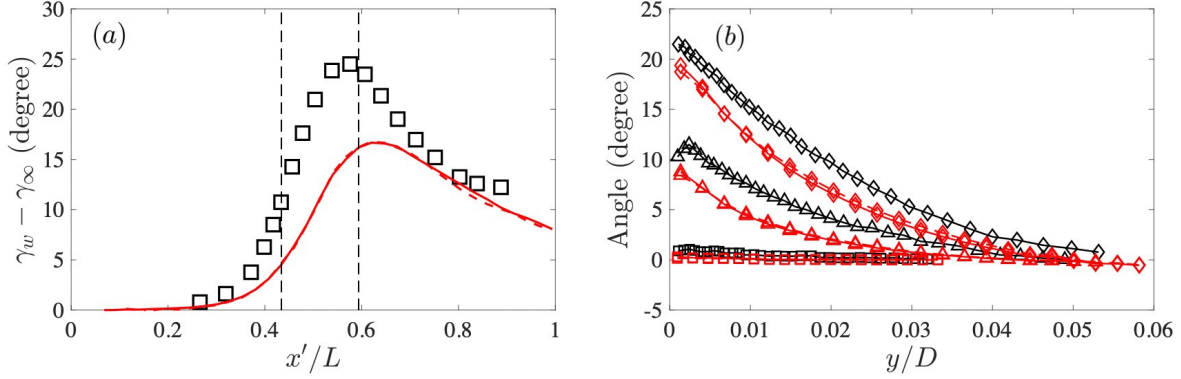


Figure 2.21: (a) Centerline distribution of the surface flow turning angles with respect to the freestream ($\gamma_w = \tan^{-1}(\tau_{w,z}/\tau_{w,x})$ is the wall shear stress direction, $\gamma_\infty = \tan^{-1}(W_e/U_e)$ is the freestream direction). Squares, experiment; red solid line, EQWM with Vreman model; red dashed line, EQWM with DSM. (b) Mean-flow direction relative to the local freestream as a function of wall distance. Red solid line, EQWM with Vreman model; red dashed line, EQWM with DSM; black solid line, experiment. Symbols are used to differentiate stations along the duct floor centerline only (Square, station 0; triangle, station 6; diamond, station 10). Lines with the same symbols denote the results at the same stations.

tensor in 3DTBLs in the RANS context. Agrawal et al. (2022) recently proposed a dynamic tensor-coefficient Smagorinsky model (DTCSM), where the SGS stress tensor is related to the filtered rate-of-strain tensor through a second-order tensor of model coefficients with four independent parameters. This tensor-coefficient-based SGS model is also examined under the same numerical setup as with the DSM model. The results of flow directions are presented in Fig. 2.22. The effect of DTCSM is shown to be most pronounced in the region where the mean-flow three-dimensionality is strongest. It is noted that the surface flow turning angles (wall model, Fig. 2.22(a)) and the mean-flow direction near the wall (LES, Fig. 2.22(b)) are both underpredicted with the DTCSM as compared to other SGS models deployed. However, the prediction seems to improve as the distance from the wall increases (Fig. 2.22(b)). Within $0.015 \leq y/D \leq 0.025$, DTCSM and Vreman results are almost the same. Further away from the wall, the DTCSM results have better agreement with the experiment.

2.9. Effects of the matching height

The wall-model/LES matching height (h_{wm}), which dictates the extent of the wall-modeled region, is an implicit model parameter in the majority of wall models. Previous studies reported potential

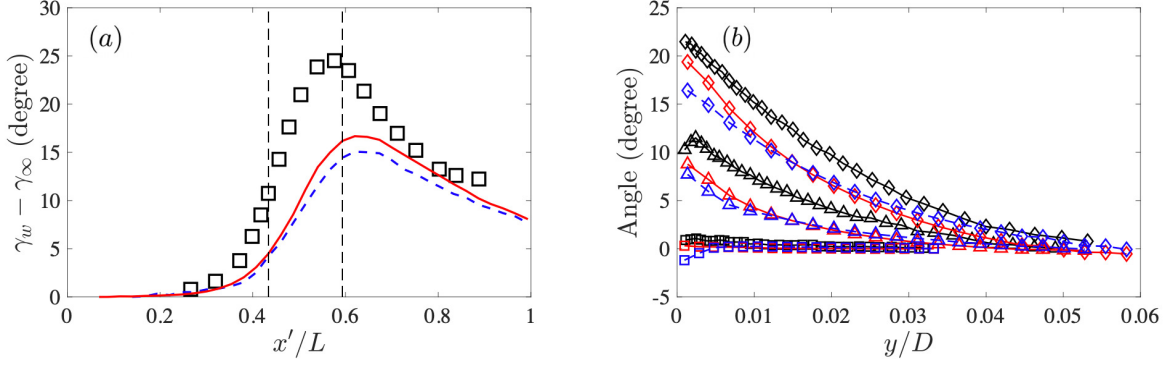


Figure 2.22: (a) Centerline distribution of the surface flow turning angles with respect to the freestream ($\gamma_w = \tan^{-1}(\tau_{w,z}/\tau_{w,x})$ is the wall shear stress direction, $\gamma_\infty = \tan^{-1}(W_e/U_e)$ is the freestream direction). Squares, experiment; red solid line, EQWM with Vreman model; blue dashed line, EQWM with DTCSM. (b) Mean-flow direction relative to the local freestream as a function of wall distance. Red solid line, EQWM with Vreman model; blue dashed line, EQWM with DTCSM; black solid line, experiment. Symbols are used to differentiate stations along the duct floor centerline only (Square, station 0; triangle, station 6; diamond, station 10). Lines with the same symbols denote the results at the same stations.

sensitivities of WMLES result with respect to h_{wm} (Kawai and Larsson, 2012; Yang et al., 2017). Log-layer mismatch associated with over- or underprediction of the wall shear stress is known to occur when this interface is placed near the wall-adjacent cells in LES or when h_{wm} lies below the buffer layer. Some remedies, such as filtering the wall-model input in time (Yang et al., 2017), taking the model input from farther away from the wall (Kawai and Larsson, 2012), or a combination of the two (Owen et al., 2020), are reported to resolve this issue. In the present study, we adopt the method of (Kawai and Larsson, 2012), as it was shown effective enough to eliminate log-layer mismatch issue in the previous studies (Park and Moin, 2014, 2016a). The practice of using the information away from the wall for wall modeling can, however, pose a challenge to the wall models in complex flows. It is often argued that wall models can better reflect the local near-wall flow when operating with the near-wall information, particularly in separated flows with locally reversed fluid motion, and in 3DTBLs where the flow direction changes with wall distance. Sensitivity of WMLES result to h_{wm} has not been reported in 3DTBLs to the best of our knowledge. This issue is discussed in this section using the three wall models deployed in the present study.

To test the effects of the matching height on the prediction of the mean three dimensionality,

WMLES with double the matching height of the original simulations were performed using the three wall models on the coarse mesh. The new matching height is still found to be well within the log layer, and the log-layer mismatch is avoided as in the original calculations. While the outer-layer flow statistics in the LES were found to be largely unchanged, notable changes in the surface flow angle were found. From Fig. 2.23(a), it is clear that prediction of the near wall flow turning becomes worse when h_{wm} is increased. Note that the PDE NEQWM is much less sensitive to change in h_{wm} compared to the other two wall models: the changes in the prediction with the PDE NEQWM simulation are smaller than that with the other two wall models when the matching height is doubled, particularly for the maximum turning angle ($\max(\gamma_w - \gamma_\infty)$). This is consistent with the fact that the PDE NEQWM has the superior capability among the three models of representing the flow-direction variation with respect to wall distance, as discussed in Fig. 2.17(a). On the other hand, the EQWM assumes a unidirectional flow within the wall model, imposing the flow direction from the LES at the matching height. This makes the EQWM result sensitive to h_{wm} when the flow direction varies with wall distance. The integral NEQWM models the two wall-parallel velocity components separately, assuming a linear sublayer near the wall and a linear departure from the log law elsewhere. This appears to render the sensitivity of the integral NEQWM to be in between the PDE NEQWM and the EQWM, albeit it is closer to the EQWM. As noted earlier, this change in the surface flow direction appears to have limited impact on the outer layer of 3DTBLs driven with the inviscid skewing mechanism. From Fig. 2.23(b), the mean-flow direction with respect to the wall distance shows negligible difference for the two matching heights.

2.10. Modifications to the original integral NEQWM

In the original 3D integral NEQWM formulation in Yang et al. (2015), the assumed velocity profiles for the two wall-parallel velocity components in the viscous sublayer were given by,

$$\begin{aligned} u &= u_{\tau,x} \frac{y}{\delta_\nu} \\ w &= u_{\tau,z} \frac{y}{\delta_\nu}, \end{aligned} \tag{2.31}$$

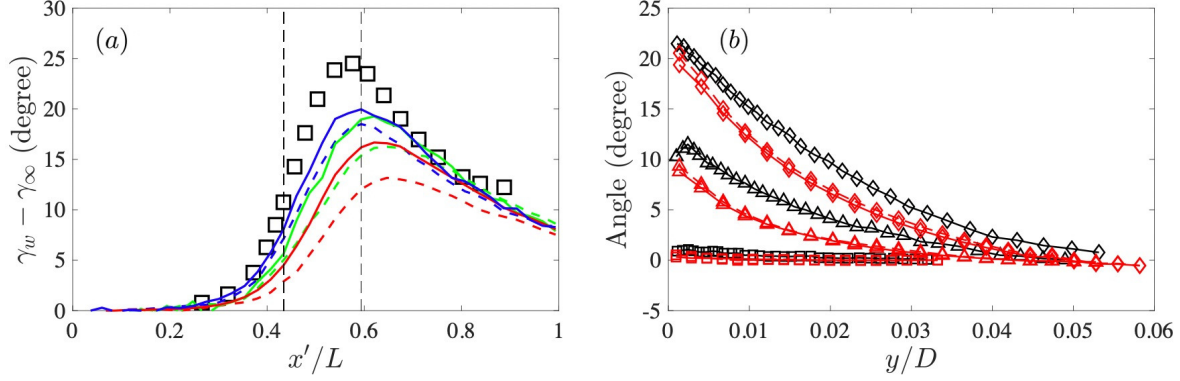


Figure 2.23: (a) Centerline distribution of the surface flow turning angles with respect to the freestream ($\gamma_w = \tan^{-1}(\tau_{w,z}/\tau_{w,x})$ is the wall shear stress direction, $\gamma_\infty = \tan^{-1}(W_e/U_e)$ is the freestream direction). Squares, experiment; red line, EQWM; blue line, PDE NEQWM; green line, integral NEQWM. Dashed lines denote calculations run with double the matching height. Solid lines denote the baseline calculations as in Fig. 2.9. (b) Mean-flow direction relative to the local freestream as a function of wall distance. Red solid line, EQWM with the original matching height; red dashed line, EQWM with double the matching height; black solid line, experiment. Symbols are used to differentiate stations along the duct floor centerline only (Square, station 0; triangle, station 6; diamond, station 10). Lines with the same symbols denote the results at the same stations.

where $u_{\tau,x} \equiv \left(\frac{\tau_{w,x}}{\rho}\right)^{1/2}$ and $u_{\tau,z} \equiv \left(\frac{\tau_{w,z}}{\rho}\right)^{1/2}$ are the local x and z components of friction velocity, δ_ν is the viscous length-scale obtained from the consistent relation $u_\tau^4 = u_{\tau,x}^4 + u_{\tau,z}^4$, and y is the wall-normal distance from the wall. In our current formulation, we modify the sublayer profile as follows,

$$\begin{aligned} u &= \text{sign}(u_{\tau,x}) \frac{u_{\tau,x}^2}{u_\tau} \frac{y}{\delta_\nu} \\ w &= \text{sign}(u_{\tau,z}) \frac{u_{\tau,z}^2}{u_\tau} \frac{y}{\delta_\nu}, \end{aligned} \quad (2.32)$$

where $\text{sign}()$ operator outputs the sign of the quantity within the parenthesis.

The desired asymptotic behavior of velocity near the wall is given by the Taylor series expansion as,

$$u = u(0) + \left. \frac{\partial u}{\partial y} \right|_w y + \mathcal{O}(y^2) \approx \left(\frac{\tau_{w,x}}{\mu} \right) y, \quad (2.33)$$

where $u(0)$ is zero due to the no-slip condition, and the higher order terms are ignored as $y \rightarrow 0$. With the original formulation 2.31, the following asymptotic behavior is obtained (derivation is provided in Hayat and Park (2021)),

$$u = \left(\frac{\tau_{w,x}}{\mu} \right) y \frac{1}{\sqrt{\cos^2 \theta + \cos \theta \sin \theta}}, \quad (2.34)$$

where $\theta = \arctan\left(\frac{\tau_{w,z}}{\tau_{w,x}}\right)$. Note that θ is dependent on the choice of local x/z coordinate system through the respective components of the predicted wall shear stress along those coordinate axes. The additional factor $\frac{1}{\sqrt{\cos^2 \theta + \cos \theta \sin \theta}}$ in Eqn. 2.34 compared to Eqn. 2.33 is what renders the original formulation inconsistent. It can be shown (Hayat and Park (2021)) that the new choice of assumed sublayer profile in Eqn. 2.32 always results in the consistent near-wall asymptotic behavior as given by Eqn. 2.33, irrespective of the choice of local x/z coordinate system. Therefore, consistent results are obtained with arbitrary choices of the local wall-parallel coordinate axes in our current formulation.

Further improvements to the original integral NEQWM include those on the implementation side. Specifically, the model is extended to unstructured solvers, which require the spatial gradients within the wall model to be computed using the cell-based gradient routine of the LES solver. This requires exchanging information between wall model and LES solvers, for which new communication protocols have been implemented. For details of this implementation, the reader is referred to Hayat and Park (2021).

CHAPTER 3

ON THE GRID CONVERGENCE OF WALL-MODELED LARGE-EDDY SIMULATION

3.1. Convergence in WMLES: Background

Wall modeling and demonstration of grid convergence may appear incompatible at first glance. The former prefers coarse grid resolutions by definition, while the latter requires finer grids. How can these seemingly competing objectives be reconciled? Figure 3.1 shows a schematic of the grid convergence concept in WMLES. WMLES operates with grid spacings that are large in the inner viscous scale (say, Δ^+ at least $O(100)$). In fact, preference to use increasingly coarse LES grids to produce reasonable results with very low cost seems to be shared among the LES community, because it better demonstrates the effectiveness of wall modeling. At the same time, and conversely, demonstration of grid convergence in WMLES requires proving a reasonable level of invariance of the WMLES prediction when the LES grid is successively refined. To keep the cost at the wall-modeled regime, the grid convergence is often expected to be demonstrated using $O(10)$ grid cells to resolve the boundary layer thickness (δ). For instance, Choi and Moin (2012) suggested 10 to 30 cells per δ . Note that for large-scale external aerodynamics applications, the cost of LES is still very high even with wall modeling, and the grid convergence is sometimes examined with $O(1)$ cells per δ Goc et al. (2021). Overall, an ideal situation is that the grid convergence in WMLES is demonstrated with grids that satisfy $\Delta^+ \gg O(100)$ and $\Delta/\delta = O(0.1) \sim O(1)$, corresponding to the overlapping shaded region in Fig. 3.1.

Feasibility of grid convergence in canonical wall-bounded flows meeting these conditions can be discussed qualitatively based on the overlap layer argument for the log layer. In derivation of the log law, it is assumed that there is a range of y (wall distance) which is large/small in the inner/outer scales, respectively. Combined with the fact that the eddy size (ℓ) scales with the wall distance according to the attached eddy theory Marusic and Monty (2019), the overlap-layer assumption is in fact compatible with the desired condition of WMLES convergence discussed earlier. Assuming resolution of the eddies residing in the log layer (which exists between about $y^+ = 30$

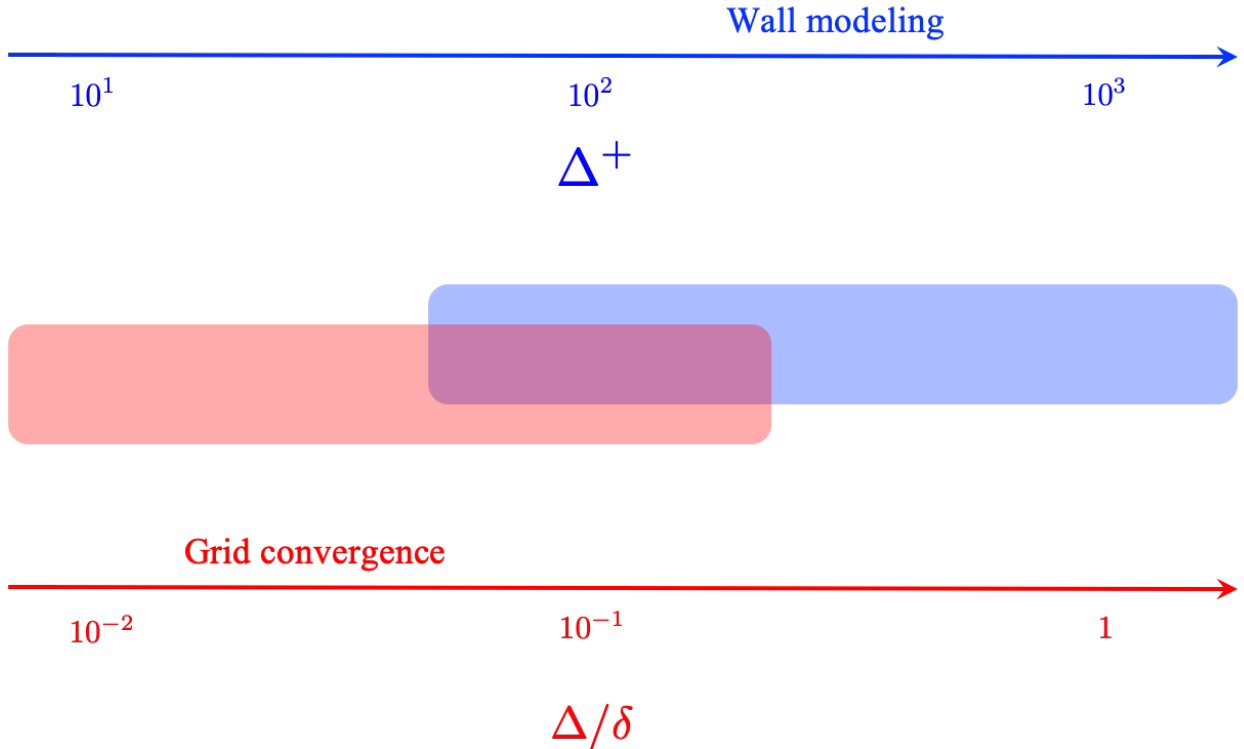


Figure 3.1: A schematic of the grid convergence concept in WMLES. The axes with different colors denote grid spacing in inner viscous scale (blue, Δ^+) or outer scale (red, Δ/δ). Wall modeling is called for when the near-wall grid spacings in LES are large (say, $O(10^2)$ or larger) in viscous wall units. At the same time, convergence of WMLES should be ideally demonstrable with $\Delta/\delta = O(10^{-2}) \sim O(10^{-1})$ before reaching the resolved LES limit. The friction Reynolds number is assumed to be $O(10^4)$ or higher.

and $y/\delta = 0.3$) requires $O(1) \sim O(10)$ cells, it can be argued loosely that the eddies residing in the log layer (especially those at $y/\delta > 0.1$, typically above the LES/wall-model matching location) can be reasonably resolved (and converged) with grid spacings satisfying $\Delta^+ \gg O(100)$ and at the same time $\delta/\Delta = O(1) \sim O(10)$ for high enough Reynolds number flows. Features residing above the log layer will be naturally resolved, as they are larger in their size. In short, the existence of log layer in high Reynolds number wall turbulence somewhat alludes to the possibility of achieving grid convergence in WMLES (at least above the buffer layer) without overly refining the grid.

This line of thinking can be extended further to incorporate existing data on the lengths scales of certain flow features/statistics. Given the fact that WMLES aims for accurate prediction of the outer portion of boundary layer (say, $y/\delta > 0.1$) using grid resolutions (Δ) that scale with the local

boundary-layer thickness

$$\frac{\delta}{\Delta} \sim O(10), \quad (3.1)$$

we first assume that a quantity of interest (QoI) in WMLES has a length scale ℓ that is $O(1)$ when expressed in terms of the boundary-layer thickness (δ).

$$\frac{\ell}{\delta} \sim O(1). \quad (3.2)$$

The QoI is then to be resolved with $O(10)$ cells in WMLES Larsson et al. (2016); Bose and Park (2018),

$$\frac{\ell}{\Delta} \sim O(10), \quad (3.3)$$

which is assumed to be adequate for demonstrating grid independence of the QoI with the length scale ℓ , based on convergence trend of reported WMLES calculations Park and Moin (2016b); Park (2017); Goc et al. (2021); Hu et al. (2023). By definition, the grid spacing in viscous wall unit has to be sufficiently large in WMLES. This quantity can be expressed as

$$\frac{\Delta}{\delta_\nu} = \frac{\Delta}{\delta} \cdot Re_\tau \sim O(Re_\tau/10). \quad (3.4)$$

This line of analysis suggests that, when a boundary layer at sufficiently high Reynolds number is calculated with WMLES using $O(10)$ cells per boundary-layer thickness, a QoI with a length scale comparable to δ can be converged on typical WMLES grid resolutions without reaching the WRLES limit. It is then of interest to explore length scales (ℓ) of a few important flow quantities in canonical flows. Sillero et al. (2014) reported in their DNS of zero-pressure gradient flat plate boundary layer up to $Re_\tau = 2000$ that the integral length scale of the streamwise velocity fluctuations (u') stays roughly constant at δ for $y/\delta > 0.2$ and approaches zero toward the wall. In the wall-normal and the spanwise directions, the integral length scales of u' at $y/\delta > 0.2$ varied between about 0.2δ and 0.4δ . The integral length scales of v' and w' were about two to three times smaller than those of u' . Integral length scales of the pressure fluctuations were at most 0.5δ , and they remain finite at about 0.1δ at the wall (Xu et al., 2020), unlike those of velocity fluctuations (also note that the variance

of pressure remains finite at the wall, unlike the velocity fluctuations). Based on this observation, one may anticipate the followings.

- The mean velocity has chances to converge on typical WMLES grid resolution, because it generally has length scales comparable to the flow scale δ .
- The Reynolds stresses will generally converge slower than the mean velocity. One may be able to converge Reynolds stresses at $y/\delta > 0.2$ with typical WMLES grid resolutions (but needs to be finer than the minimum grid resolution required for convergence of the mean field).
- As the pressure fluctuations remain finite at the wall, its convergence in WMLES may require at least about 0.02δ of grid spacing (4 to 5 cells per integral length scale).

The convergence trend reported in WMLES of channel flow at $Re_\tau = 2000$ (e.g., Fig. 1 and Table 1 from Park and Moin (2016b)) and separating/reattaching flow over a hump up to $Re_\tau \approx 5000$ (e.g., Fig. 9 from Park (2017)) is consistent with this suggestion. Note that the analysis above suggests that convergence and accurate prediction of fluctuating quantities near and at the wall (say, $y/\delta < 0.1$) may necessitate quite fine grid resolutions. In doing so, the grid spacings in viscous wall units might end up being small enough to be considered as WRLES, if Reynolds number is not sufficiently high (Eq. 3.4).

3.2. A proposition on the grid convergence in WMLES

The previous section introduced a qualitative discussion on what grid convergence means in inherently very coarse WMLES calculations. In this section, we provide a proposition on how this convergence behavior might be mediated by a wall modeling choice, namely, the extent of the wall-modeled region, which is commonly referred to as the matching height in the literature (denoted h_{wm} in this work). We hypothesize that h_{wm} affects the convergence behavior of WMLES conducted with conventional wall-stress models, where the wall-shear stress modeled by wall models are used as the Neumann-type wall boundary condition in the LES. Wall models take input from the LES at $y = h_{wm}$, which typically is at about 10% of the local boundary-layer thickness. Frequently, a couple LES grid cells are deployed between the wall and $y = h_{wm}$ to avoid the log-layer mismatch

problem where the wall stress is over- or underpredicted Kawai and Larsson (2012); Yang et al. (2017); Owen et al. (2020).

For a fixed extent of the wall-modeled region, once the turbulence scales start to be resolved at $y = h_{wm}$, the wall-model input taken from the LES is likely unchanged with further grid refinements, leading to the converged model output (wall stress). Convergence in WMLES might be expected from this point. Additional refinements beyond this point will likely generate smaller length scales in the LES only between the wall and the matching location, but not in the wall stress as well as in the LES solution above $y = h_{wm}$. This is particularly true for widely used simple wall models (e.g., algebraic (Owen et al., 2020; Goc et al., 2021) or ODE wall models (Wang and Moin, 2002; Bodart and Larsson, 2011; Hayat and Park, 2023)) in which the model input and output are perfectly correlated as shown in Park and Moin (2016b). This state where the wall stress and the outer 90% of the boundary layer is not responding to further grid refinements may be considered as the onset of grid convergence in WMLES for practical reasons. If this assumption is combined with the commonly accepted notion of wall-attached eddies where the size of the coherent structures in wall turbulence is proportional to the wall distance (therefore requiring coarser grid resolution to converge eddies further away from the wall), one can hypothesize that WMLES would tend to converge at a coarser grid resolution when the wall-modeled region extends further away from the wall.

A schematic illustrating the above proposition is shown in Fig. 3.2, where a potential convergence trend of WMLES conducted with different extents of the wall-modeled region is shown. The WMLES would reach grid convergence at certain grid resolution $\Delta_i = C * h_{wm,i}$ ($i = 1, 2, 3$) that is proportional to the wall model matching height. The constant $C = \Delta_i/h_{wm,i}$ could potentially be the same among different wall model matching heights. Note that Kawai and Larsson (2012) suggested that C be less than one in the context of removing the log-layer mismatch, and many reported WMLES calculations adopted $C = 0.2 \sim 0.3$ (i.e., deploying about three LES grid cells in the wall-modeled region) (Larsson et al., 2016; Owen et al., 2020; Park and Moin, 2016b; Park, 2017).

Note that the final converged states obtained with different values of h_{wm} can be potentially different, as depicted in Fig. 3.2. This can be argued in two different contexts. First, wall models are generally known to exhibit some sensitivities of the predicted wall stress to the matching height, especially for simple type of wall models. For example, the algebraic or ODE equilibrium wall models assume a unidirectional flow within the wall-modeled region, which is invalid in three dimensional boundary layer where the flow direction depends on the wall distance. In this situation, the wall modeling error increases with higher values of h_{wm} . Also note that a recent model comparison study Hu et al. (2023) showed that more complex wall models (nonequilibrium models of the integral type Yang et al. (2015) and the PDE type Park and Moin (2014)) are considerably less sensitive to the change in the matching location than the ODE equilibrium wall model Kawai and Larsson (2012) in prediction of a three dimensional boundary layer in a bent square duct. Second, in analogy to the role of filter width in the explicitly filtered LES Bose et al. (2010), the matching height (or extent of the wall-modeled region) is expected to dictate the range of length scales that are explicitly modeled (and also the scales somewhat prohibited from being generated) in the LES. In explicitly filtered LES, the converged LES result depends on the choice of filter width (kept constant during grid refinements) and the subfilter-scale (SFS) stress model. In analogy, it might be postulated that the converged WMLES result may (or, have to) depend on the choice of h_{wm} (the extent of the wall-modeled region) and the wall model. To elaborate more on this point, in explicitly filtered LES, the filter prevents generation of subfilter scales in the LES, ensuring the grid-converged LES are free from numerical error while the subfilter-stress model is still active. If the so obtained grid-independent LES is any different from the expected ground truth (e.g., filtered DNS), the error can be attributed solely to the modeling error. In a somewhat similar spirit, fixing the extent of the wall-modeled region during the LES grid refinement will likely have similar effects as fixing the filter width during grid refinements in explicitly filtered LES. For instance, no finer scales in the wall stress field will develop once the LES flow at the matching location is resolved. Error in the converged WMLES result may be attributed solely to the wall-modeling error, as wall models are presumably not subject to numerical error once the flow at $y = h_{wm}$ is resolved.

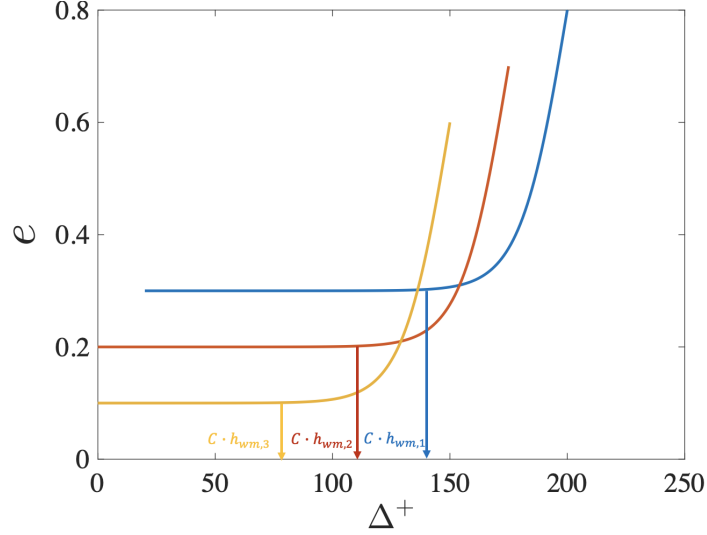


Figure 3.2: A schematic of the grid convergence trend (error vs. grid resolution) for three different wall model matching heights ($h_{wm,1} > h_{wm,2} > h_{wm,3}$) as described in the proposition.

3.3. Numerical details and wall modeling

Numerical experiments were performed with CharLES, an unstructured cell-centered finite-volume compressible LES solver developed at Cascade Technologies Inc. and Cadence. The solver employs an explicit third-order Runge-Kutta (RK3) scheme for time advancement and a second-order central scheme for spatial discretization. More details regarding the flow solver can be found in Khalighi et al. (2011) and Park and Moin (2016a). Vreman model (Vreman, 2004) is used to close the SGS stress and heat flux. The wall model used in the present work is an algebraic wall model based on the law of the wall, which was used recently for aircraft LES at high lift configurations Goc et al. (2021). The model is give as

$$u^+(y^+) = \begin{cases} y^+ + a_1(y^+)^2 & \text{for } y^+ < 23 \\ \frac{1}{\kappa} \log y^+ + B & \text{otherwise} \end{cases} \quad (3.5)$$

where $B = 5.2$ and a_1 is calculated to ensure C^1 continuity at $y^+ = 23$. The algebraic wall model is adopted here due to its simplicity in the context of WMLES grid convergence, as it obviates the need for meshing or discretization for the wall model.

3.4. Flow configuration

Two flow configurations are considered in the present study. The first case is the plane turbulent channel flow with periodic boundary conditions in the streamwise and spanwise directions. The Johns Hopkins Turbulence Database (JHTDB)(Li et al., 2008; Perlman et al., 2007; Graham et al., 2016) turbulent channel flow data ($Re_\tau = 1000$) is used as the reference. The computational domain is set to be $(L_x, L_y, L_z) = (2\pi\delta, 2\delta, \pi\delta)$, where x is the streamwise direction, y is the wall-normal direction, and z is the spanwise direction. δ is the channel half height. The flow is driven by a constant mass flow rate in the streamwise direction.

The second flow configuration is based on the work of Spalart (Spalart, 1989), where a boundary layer is created on an infinite flat plate by a time-dependent freestream velocity vector, whose magnitude is independent of time but whose direction (as seen in the wall-parallel plane) changes at a constant angular velocity. The Reynolds number $Re_l = U_0 \left(\frac{2}{f\nu}\right)^{1/2}$ is 767, where U_0 is the freestream velocity magnitude, f is the angular rate of rotation of the freestream velocity vector, and ν is the kinematic viscosity. In our numerical simulation, the computational domain is set to be $(L_x, L_y, L_z) = (2\delta, \delta, 2\delta)$, where y is the wall-normal direction. The outer length scale used in the reference study is $\delta = \frac{u^*}{f}$, where u^* is the velocity scale (equal to u_τ in the basic theory in (Spalart, 1989)). The top boundary condition is set to be the rotating velocity vector given by,

$$U_\infty = U_0 \cos(ft), \quad W_\infty = W_0 \sin(ft). \quad (3.6)$$

Periodic boundary conditions are applied to the two horizontal directions, x and z . The flow statistics are computed in the coordinate system that is rotating with the freestream velocity vector. In this coordinate system, the mean flow is steady, having two non-zero wall-parallel velocity components which vary in the wall-normal direction. The velocity profile is ‘skewed’, where the flow direction changes continuously with the wall distance.

Table 3.1: Isotropic grid resolutions (in wall units) and the matching heights used in the WMLES of the turbulent channel flow at $Re_\tau = 1000$.

cases	$h_{wm} = 0.1$	$h_{wm} = 0.2$
1	200	400
2	66.7	133
3	40	80
4	22.2	44.4
5	15.4	30.8
6	11.8	23.5

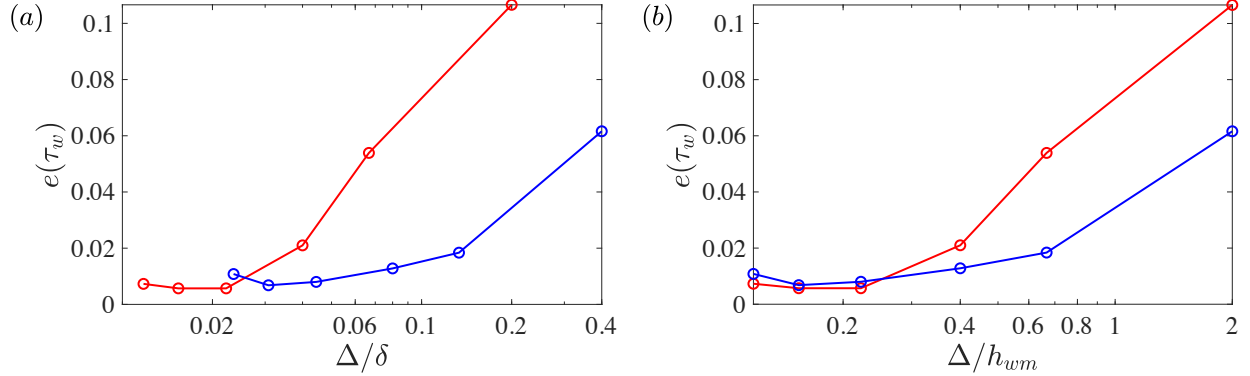


Figure 3.3: Grid convergence of the skin friction (τ_w) in turbulent channel flow at $Re_\tau = 1000$. (a) Grid spacing is normalized by the half channel height δ ; (b) Grid spacing is normalized by the wall model matching height (h_{wm}). Blue, $h_{wm} = 0.2\delta$; red, $h_{wm} = 0.1\delta$.

3.5. Results and discussion

3.5.1. Grid convergence of skin friction

Figure 3.3 shows the grid convergence trend for turbulent channel flow. All the cases with different grid spacings and matching heights are listed in Table 3.1. Note that the isotropic grid resolutions are selected such that the matching location is always located at the cell centers. This helps eliminating the odds that the interpolation error interferes the interpretation of the convergence trend. The error of the wall shear stress is defined as

$$e(\tau_w) = \frac{|\tau_w - \tau_{w,DNS}|}{\tau_{w,DNS}}. \quad (3.7)$$

Figure 3.3(a) shows the error as a function of the absolute grid spacing. The skin friction predicted by the wall model gradually approaches the exact wall-shear stress and remains largely unchanged when the grid is refined sufficiently. For the case with $h_{wm} = 0.2\delta$, the grid convergence (identified as a plateau in the figure) can be clearly observed starting at $\Delta/\delta = 0.08$. For the $h_{wm} = 0.1\delta$ case, the grid convergence started at about $\Delta/\delta = 0.02$. Thus, the $h_{wm} = 0.1\delta$ case reaches grid convergence more slowly (i.e. at a finer grid resolutions) than the case with $h_{wm} = 0.2\delta$, which is consistent with our proposition illustrated in Fig. 3.2. When the grid spacing is normalized by the wall model matching height (Fig. 3.3(b)), some level of self-similarity is found. The error curves toward the finest resolutions show a better collapse, and the onset of convergence is marked roughly at a common value of the grid spacing as a fraction of the matching height ($\Delta/h_{wm} \approx 0.4$). This suggests that the wall model matching height is closely related to the convergence trajectory.

Figure 3.4 shows the grid convergence trend for the skin friction from the 3DTBL with a rotating freestream velocity vector. Figure 3.4(a) shows the error as a function of the grid spacing normalized by the boundary layer thickness. Unlike the previous case, stronger sensitivity of the converged skin friction value to the matching location is found. The simple wall model deployed in this work assumes a unidirectional flow within the wall-modeled region, modeling only the magnitude of the skin friction but assuming the flow is aligned with the LES velocity at $y = h_{wm}$. This assumption is invalid in 3DTBL, and generally the converged wall-shear stress is more accurate for smaller value of h_{wm} (recall that the the flow direction varies with the wall distance). Nonetheless, it is observed that the convergence in the skin friction starts at a coarser grid resolution for a larger extent of the wall-modeled region, as posited earlier. For instance, the convergence starts at $\Delta = 0.05\delta$ for $h_{wm} = 0.15\delta$, while it starts at $\Delta = 0.02\delta$ for $h_{wm} = 0.05\delta$. In Fig. 3.4(b), the grid spacing is normalized by the matching height. It can be observed again that the collapse of the error curves improve with this scaling, and that the convergence starts roughly at a common value (≈ 0.3) of Δ/h_{wm} . This supports our proposition that the wall model matching height would be a proper length scale for the grid convergence of WMLES.

Note that all cases from the channel and the 3DTBL appear to share a common requirement of

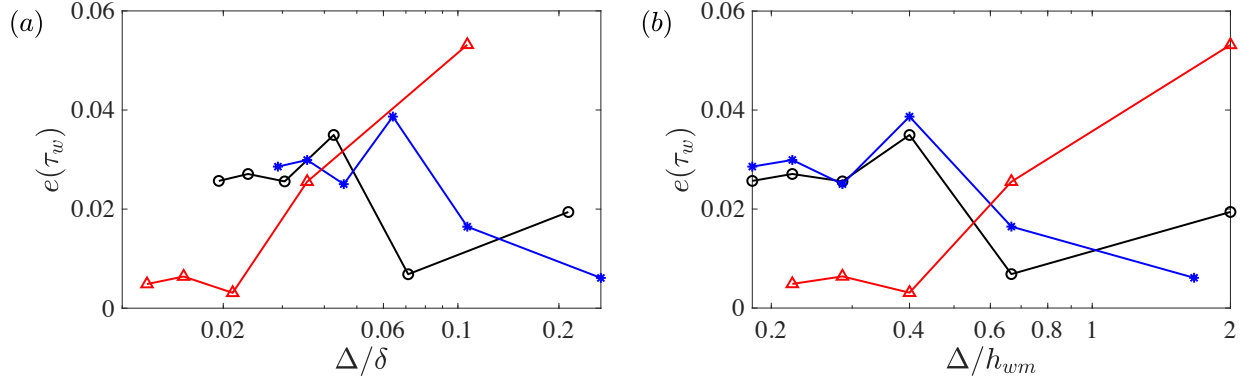


Figure 3.4: Grid convergence of the skin friction (τ_w) in 3DTBL. (a) Grid spacing is normalized by the boundary layer thickness δ ; (b) Grid spacing is normalized by the wall model matching height (h_{wm}). Blue, $h_{wm} = 0.15\delta$; black, $h_{wm} = 0.1\delta$; red, $h_{wm} = 0.05\delta$.

$\Delta/h_{wm} < 0.4$ to claim convergence, which is comparable to the condition to avoid the log-layer mismatch problem (Kawai and Larsson, 2012).

3.5.2. Grid convergence of mean velocity and Reynolds stress

The convergence of the mean velocity and Reynolds stress are discussed in terms of their errors compared to the DNS results. For the mean velocity profile, the global error is defined as the integration of the local error from the wall model matching height $y = h_{wm}$ to the channel centerline, following Lozano-Durán and Bae (2019),

$$e(U) = \frac{\left[\frac{1}{\delta - h_{wm}} \int_{h_{wm}}^{\delta} (U - U_{DNS})^2 dy \right]^{1/2}}{\max |U_{DNS}|}. \quad (3.8)$$

Similarly, the global error of the streamwise rms intensity (u_{rms}) is defined as

$$e(u_{rms}) = \frac{\left[\frac{1}{\delta - h_{wm}} \int_{h_{wm}}^{\delta} (u_{rms} - u_{rms,DNS})^2 dy \right]^{1/2}}{\max |u_{rms,DNS}|}. \quad (3.9)$$

The choice of the wall model matching height as the lower limit of integration of the error is motivated by the fact that the sharp velocity gradient within the wall-modeled region cannot be resolved by the LES. The mean velocity gradient profiles from WMLES with $h_{wm} = 0.2\delta$ are presented in Fig. 3.5. It is worth mentioning that the velocity gradient here is calculated from the

mean momentum balance

$$\frac{dU}{dy} = \frac{\overline{\rho u'v'} - \tau_w \frac{y}{\delta} + \tau_w}{\mu + \mu_t}. \quad (3.10)$$

Equation 3.10 provides a way to obtain the mean velocity gradient without resorting to direct gradient calculation schemes (e.g. finite difference), which is inaccurate with the extremely coarse near-wall grid in WMLES. It can be clearly seen that WMLES solutions are relatively well converged above the matching location ($y^+ = 200$) where the velocity gradient is relatively small. However, the velocity gradient increases drastically towards the wall. Additionally, grid refinements keep introducing new information toward the wall (larger velocity gradient at the first grid point) until the DNS or WRLES resolution has been achieved. Overall, grid convergence will hardly be achieved below the wall model matching height (in general, buffer layer and below) in typical WMLES of high Reynolds number wall turbulence. It is therefore natural to limit our interest to convergence above $y = h_{wm}$.

The errors of the mean flow in channel flow are presented in Fig. 3.6. It can be observed that the errors gradually reach a plateau with the decrease of the grid spacing. When the grid spacing is normalized by the half channel height (Fig. 3.6(a)), it can be seen that the flattening of the error curve starts at a coarser grid resolution for $h_{wm} = 0.2\delta$, compared to the $h_{wm} = 0.1\delta$ case. When the grid spacing is normalized by the matching height h_{wm} (Fig. 3.6(b)), a better collapse in the convergence trajectories is found for values of $\Delta/h_{wm} < 0.6$, similar to the trend in the wall-stress convergence. Figure 3.7 shows the convergence trend of the streamwise turbulence intensity from the channel flow. First, it should be recognized that the error level of the intensity is an order of magnitude larger than that of the mean velocity on the same grid, consistent with the earlier discussion in Section 3.1. The Reynolds stresses have not converged on the grids where the mean flow has already converged. Although some plateau regions can be seen, they should not be taken as a measure of convergence. Overall, compared to the mean velocity, dependence of the onset of convergence on h_{wm} appears much weaker, and improvement in collapsing the curves with the Δ/h_{wm} scaling is only marginal (Fig. 3.7(b)), implying that the convergence of the Reynolds stress is not as much dependent on the extent of the wall-modeled region as the mean flow is.

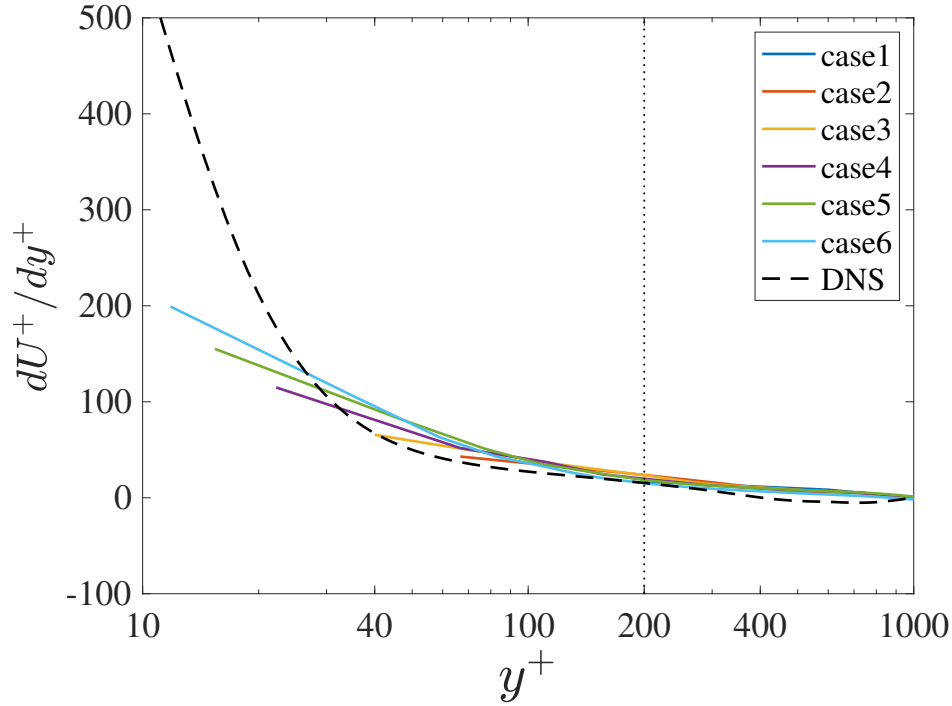


Figure 3.5: Mean velocity gradient profile in turbulent channel flow at $Re_\tau = 1000$. The mean velocity gradient is calculated from the mean momentum balance equation. Different colors denote different LES grid resolutions with $h_{wm} = 0.2\delta$ in Table 3.1. The black dashed line denotes DNS result (Li et al., 2008; Perlman et al., 2007). The vertical black dotted line denotes the wall model matching location.

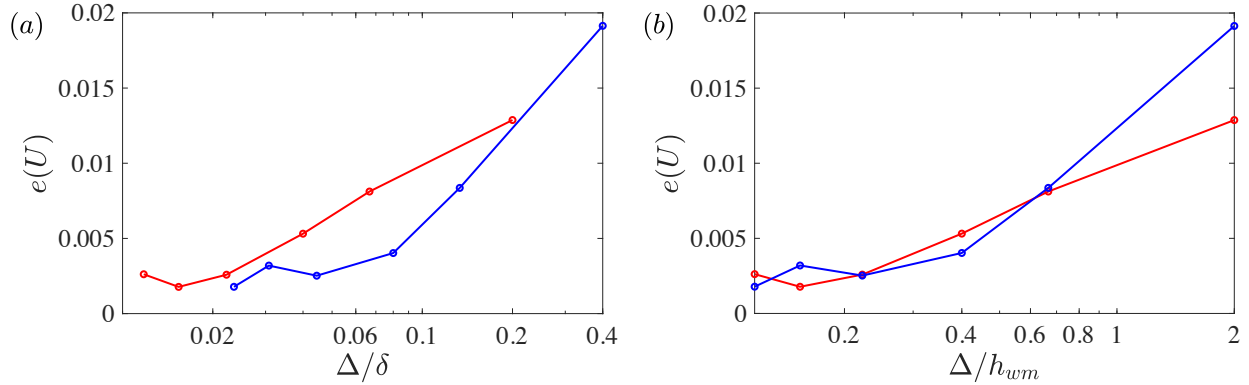


Figure 3.6: Grid convergence of mean velocity in turbulent channel flow at $Re_\tau = 1000$. (a) Error of mean velocity as a function of the grid resolution normalized by the half channel height δ ; (b) Error of mean velocity as a function of the grid resolution normalized by the matching height h_{wm} . Blue, $h_{wm} = 0.2\delta$; red, $h_{wm} = 0.1\delta$.

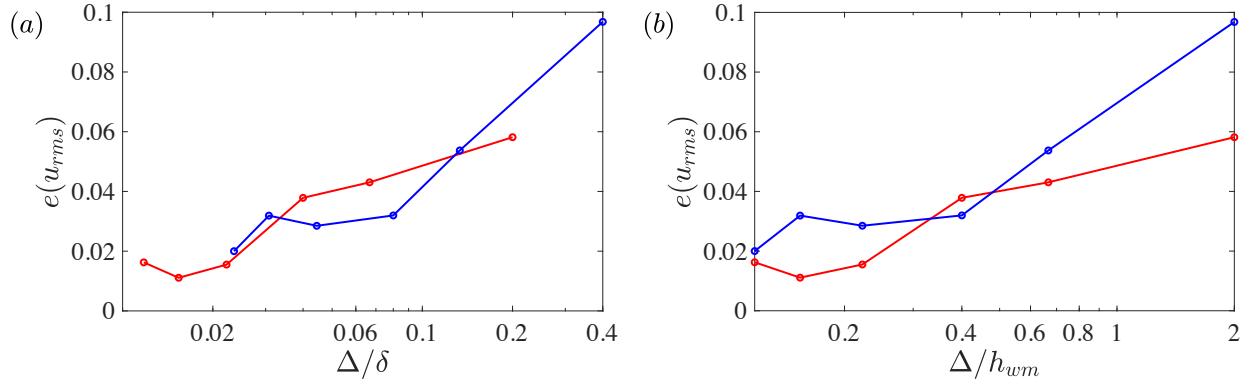


Figure 3.7: Grid convergence of rms intensity u_{rms} in turbulent channel flow at $Re_\tau = 1000$. (a) Error of u_{rms} as a function of the grid resolution normalized by the half channel height δ ; (b) Error of u_{rms} as a function of the grid resolution normalized by the matching height h_{wm} . Blue, $h_{wm} = 0.2\delta$; red, $h_{wm} = 0.1\delta$.

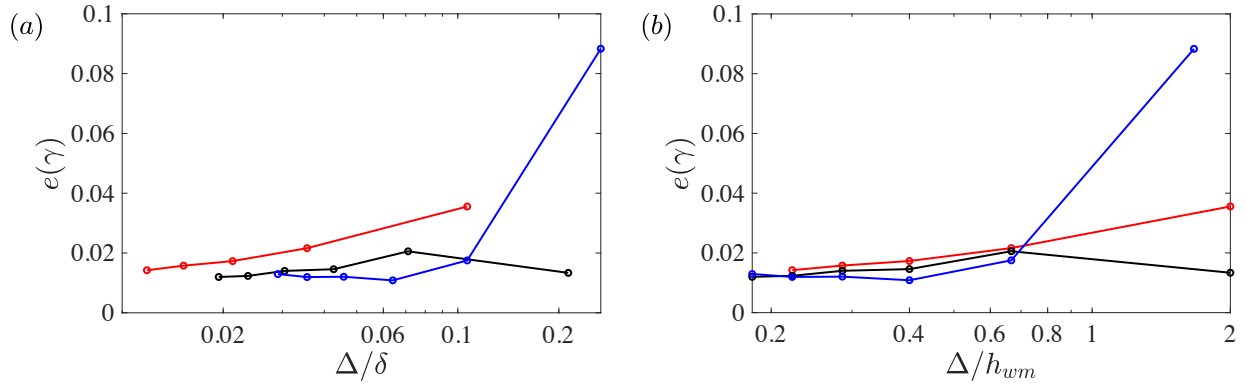


Figure 3.8: Grid convergence of mean flow direction $\gamma = \arctan(W/U)$ in 3DTBL. (a) Error of γ as a function of the grid resolution normalized by the boundary layer thickness δ ; (b) Error of γ as a function of the grid resolution normalized by the matching height h_{wm} . Blue, $h_{wm} = 0.15\delta$; black, $h_{wm} = 0.1\delta$, red, $h_{wm} = 0.05\delta$.

For the 3DTBL, the main difference compared to the canonical 2DTBL is that the flow direction changes with wall distance. Therefore, the convergence of the mean flow direction should also be taken into consideration. The error of the flow direction is defined as,

$$e(\gamma) = \frac{\left[\frac{1}{\delta - h_{wm}} \int_{h_{wm}}^{\delta} (\gamma - \gamma_{DNS})^2 dy \right]^{1/2}}{\max |\gamma_{DNS}|}, \quad (3.11)$$

where $\gamma = \arctan(W/U)$ represents the flow angle (in degree) within wall-parallel planes, U and W being the velocity components parallel and perpendicular to the freestream, respectively. The convergence of the flow direction γ is shown in Fig. 3.8. Similar to the mean flow convergence in the channel, the convergence of the flow direction is marked at a coarser grid resolution for a larger value of h_{wm} (Fig. 3.8(a)). For instance, the convergence for $h_{wm} = 0.15\delta$ starts at around $\Delta/\delta = 0.1$, and for $h_{wm} = 0.05\delta$ it starts at $\Delta/\delta < 0.02$. Additionally, a better collapse of the convergence trajectories is seen under the h_{wm} normalization of the grid spacing (Fig. 3.8(b)). These observations from the mean flow direction support the proposition in Section 3.2. Note that for all the three matching heights, the mean velocity magnitude essentially converged except for the first very coarse resolution, the error of which being all around 0.5% of the maximum velocity magnitude, and it is therefore not shown here. Figure 3.9 shows the convergence of u_{rms} for the 3DTBL (the flow remains laminar with the coarsest grid resolution for $h_{wm} = 0.15\delta$, and it is therefore not included here). It should be noted that $e(\gamma) = 0.01$ represents roughly 0.2 degree difference in the flow direction, leading to approximately 0.3% error in U . Therefore, the error level of the turbulence intensity ($> 2\%$) is much larger than that of the mean flow. As in the channel flow, the Reynolds stresses do not show strong evidence of convergence on grids where the mean flow has clearly converged. Additionally, the Δ/h_{wm} scaling does not offer improved collapse of curves for the stresses. Overall, it is seen again the matching location has no control over convergence of the Reynolds stress.

To understand the distinct behavior of the Reynolds stress convergence, the attached eddy theory has been utilized. In our proposition, the dependence of the convergence on the matching height is due to the fact that the attached eddies scale as their distance from the wall. However, for Reynolds stresses, Hu et al. Hu et al. (2020) showed that there are energy-containing eddies other than the wall-

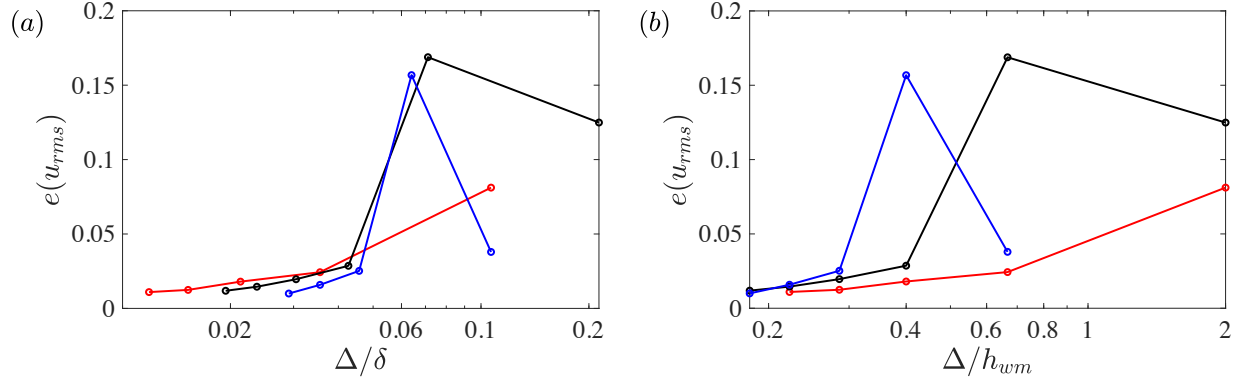


Figure 3.9: Grid convergence of rms intensity u_{rms} in 3DTBL. (a) Error of u_{rms} as a function of the grid resolution normalized by the boundary layer thickness δ ; (b) Error of u_{rms} as a function of the grid resolution normalized by the matching height h_{wm} . Blue, $h_{wm} = 0.15\delta$; black, $h_{wm} = 0.1\delta$, red, $h_{wm} = 0.05\delta$.

attached eddies, which are the small (Kolmogorov)-scale eddies and the large-scale wall-detached eddies. A similar decomposition is adopted here for the analysis of the grid convergence. The attached eddies are responsible for the streamwise velocity fluctuations of scales

$$\alpha y < \lambda_x < \beta \delta, \quad \gamma < y^+, \quad (3.12)$$

where $\alpha = 5.7$, $\beta = 2$ and $\gamma = 100$, corresponding to the triangular region in Fig. 3.11(a) from by three dashed lines. The small-scale eddies correspond to the trapezoid-like zone in the top-left corner in Fig. 3.11(a). According to this scale decomposition, contributions to the energy ($(u'_{rms})^2$) from different types of eddies can be computed by summing the energy from the respective regions in the discrete energy spectrum. The wall-normal distributions of this spectral energy contributed from the attached eddies and the small-scale eddies are shown in Fig. 3.10. The wall-normal range is roughly $100 < y^+ < 350$, which is the region where the above scale decomposition is defined, and also where the mean-velocity log law is valid. For the attached eddies, the spectral energy distributions from cases 3-5 with $h_{wm} = 0.2\delta$ show good level of collapse, which is evidence of grid convergence of the wall-attached eddies. It can also be noticed that the total spectral energy of the attached eddies increases as the wall-normal distance decreases. On the other hand, the spectral energy for the small-scale eddies is clearly not grid-converged across the entire wall-normal range.

With grid refinement, the spectral energy for the small-scale eddies increases, showing that more small-scale eddies get resolved with finer mesh. Considering case 5, the distribution of the small-scale eddies' spectral energy is nearly uniform across the log layer which is a clear contrast to the spectral energy distribution of the attached eddies.

This explains why Reynolds stresses converge more slowly than the mean velocity, and also why it shows weaker dependence on the matching location. On the grids where attached eddies have been well resolved, the mean flow (that closely follows the log law) has also converged. However, the small-scale eddies whose contribution to the Reynolds stresses is not negligible are not fully resolved. The small-scale eddies not scaling as their distance from the wall seem to make our proposition based largely on the attached-eddy idea less applicable to the fluctuating quantities. As convergence of the Reynolds stress is contingent on that of the small-scale eddies, characterizing its resolution requirement is of interest. Figure 3.11(a) shows the proportion of the spectral energy from different scales of eddies computed from the DNS data. Three lines in the small-scale eddy zone indicates the minimum length scales to be resolved for representing 70%, 80%, and 90% of the energy carried by the small-scale eddies. Assuming at least four cells are required to represent these scales in simulation, it can be argued that grid spacings of $80 \sim 30$ viscous wall units are required to produce 70 \sim 90 percents of the energy carried by the small-scale eddies. Figure 3.11(b) shows the fraction of the small-scale energy resolved in the WMLES simulations (cases 3-5) relative to the DNS data. Only the finest calculation (case 5, $\Delta^+ \approx 30$) is shown to resolve 90% of the small-scale energy in the outer region. Both cases 4 and 5 resolve 80% of the energy from the small-scale eddies at $y^+ > 200$. From Fig. 3.10(a), this condition appears to be adequate for convergence of the energy from the small-scale eddies ($\Delta^+ \approx 50$). Apparently, WMLES starts to approach WRLES upon fulfilling this condition.

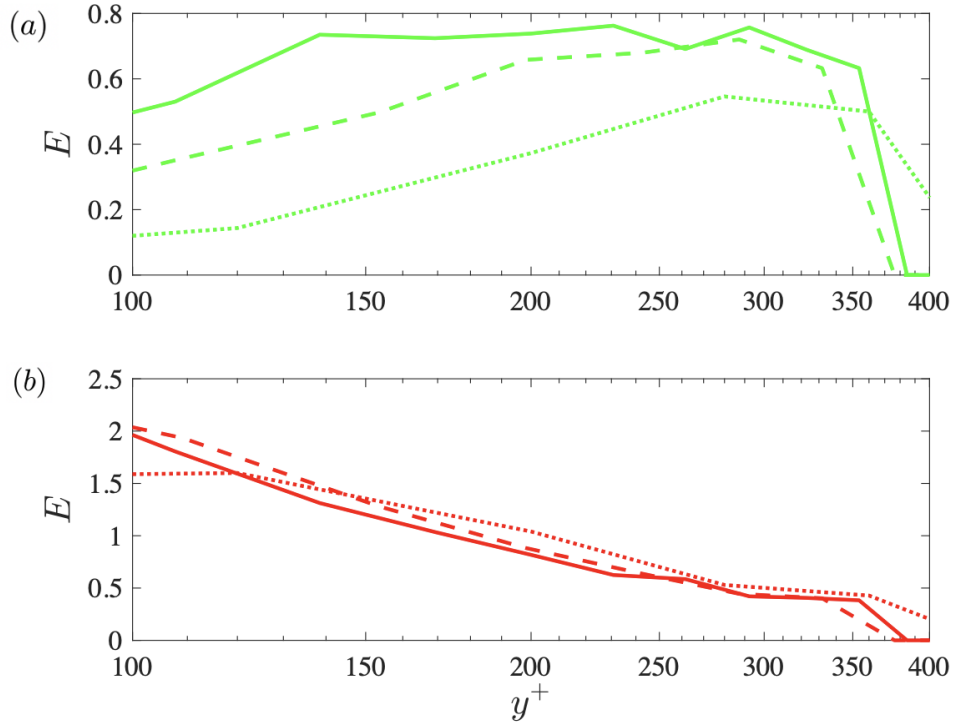


Figure 3.10: Grid convergence of the spectral energy contributed by different types of eddies in WMLES of turbulent channel flow at $Re_\tau = 1000$ (matching height $h_{wm} = 0.2\delta$). The energy from different types of eddies is calculated by integrating over corresponding length scale ranges according to Parseval's theorem. The length scales of the attached eddies are defined as given in Eq. (3.12). In the current channel flow, the definition is valid in the wall normal range $100 \leq y^+ \leq 350$. (a) Grid convergence of the energy of small-scale eddies; (b) grid convergence of the energy of attached eddies. Line types are for different cases as described in Table 1. Dotted lines: case 3; dashed lines: case 4; solid lines, case 5.

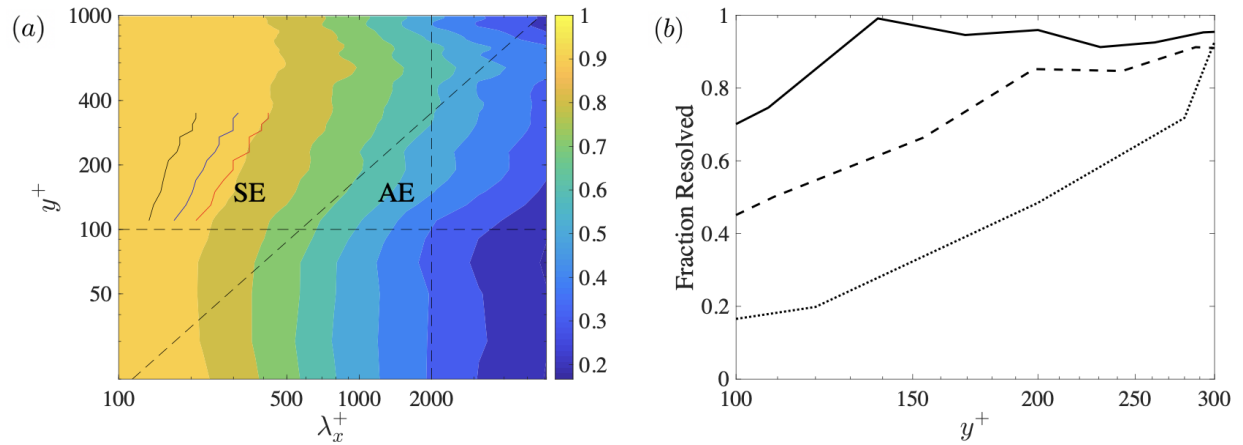


Figure 3.11: (a) Proportion of the spectral energy (streamwise velocity) as a function of length scales (λ_x^+ , streamwise wavelength) and wall distance (y^+). The result is computed from the DNS data Li et al. (2008); Perlman et al. (2007). The color denotes the percentage of the energy contained in eddies of scales larger than certain wavelength. Three colored solid lines in the small-scale (SE) eddy zone denote the minimum length scales to be resolved for representing 70% (red), 80% (blue) and 90% (black) of the energy contained in the small-scale eddies. The triangular region formed by the three black dashed lines denotes the scales of the attached eddies as given in Eq. (3.12). (b) Fraction of the small-scale eddies' energy being resolved in WMLES ($h_{wm} = 0.2\delta$) at different wall-normal locations. Black dotted line, case 3; black dashed line, case 4; black solid line, case 5.

CHAPTER 4

A HIDDEN MECHANISM OF DYNAMIC LES MODELS

4.1. Reduction of dynamic procedures along the principal directions of \bar{S}_{ij}

In Smagorinsky-type models, the deviatoric part of the SGS stress tensor τ_{ij} is modeled as

$$\tau_{ij} - \frac{1}{3}\delta_{ij}\tau_{kk} = 2C\Delta^2|\bar{S}|\bar{S}_{ij}, \quad (4.1)$$

where δ_{ij} is the Kronecker delta, Δ is the grid filter size, $\bar{S}_{ij} = \frac{1}{2}\left(\frac{\partial\bar{u}_i}{\partial x_j} + \frac{\partial\bar{u}_j}{\partial x_i}\right)$ is the resolved strain-rate tensor at the grid filter level, and $|\bar{S}| = (2\bar{S}_{kl}\bar{S}_{kl})^{1/2}$. The overbar $\bar{\cdot}$ denotes the grid-filtered quantities. The Smagorinsky coefficient C is determined by a dynamic procedure (Lilly, 1992) based on the Germano identity (GI),

$$L_{ij} = T_{ij} - \widehat{\tau}_{ij}, \quad (4.2)$$

where T_{ij} is the SGS stress at the test-filter level defined as

$$T_{ij} = \widehat{\bar{u}_i}\widehat{\bar{u}_j} - \widehat{\bar{u}_i\bar{u}_j}, \quad (4.3)$$

and τ_{ij} is the SGS stress at the grid-filter level

$$\tau_{ij} = \bar{u}_i\bar{u}_j - \overline{\bar{u}_i\bar{u}_j}. \quad (4.4)$$

The overhat $\widehat{\cdot}$ denotes the test-filtered quantities. L_{ij} contains the resolved components of the stress tensor associated with scales between the test and grid filter scales, and it can be computed directly from the information available in the LES calculations,

$$L_{ij} = -\widehat{\bar{u}_i}\widehat{\bar{u}_j} + \widehat{\bar{u}_i}\widehat{\bar{u}_j}, \quad (4.5)$$

using Eq.(4.2)–(4.4). T_{ij} is modeled similarly as in Eq. (4.1). Substitution of the modeled stresses into the deviatoric part of the Germano identity produces an over-determined system for the un-

known coefficient C ,

$$L_{ij} - \frac{1}{3}\delta_{ij}L_{kk} = CM_{ij} \quad (4.6)$$

where

$$M_{ij} = 2\widehat{\Delta}^2|\widehat{S}|\widehat{S}_{ij} - 2\Delta^2|\overline{S}|\overline{S}_{ij} \quad (4.7)$$

is again computable with the LES solution. Here, $\widehat{\Delta}$ is the test-filter size typically taken as $\widehat{\Delta} = 2\Delta$. The commonly used procedure is the least squares approach, which minimizes the L_2 norm of the GIE tensor, $Q = Q_{ij}Q_{ij}$ (Lilly, 1992). Here, Q_{ij} is the GIE tensor defined as the residual of the Germano identity

$$Q_{ij} = L_{ij} - \frac{1}{3}\delta_{ij}L_{kk} - CM_{ij}, \quad (4.8)$$

and the coefficient C is then determined as

$$C = \langle L_{ij}M_{ij} \rangle / \langle M_{ij}M_{ij} \rangle. \quad (4.9)$$

Here, $\langle \cdot \rangle$ denotes the averaging in homogeneous directions (if any) or local filtering operation used to stabilize the model. This original dynamic procedure accounts for all components (and therefore directions) of the GIE tensor collectively with equal weights.

Vorticity dynamics in the inviscid limit implies that vortices are frozen to fluid elements and therefore they deform in the same way fluid elements do. As the strain-rate tensor characterizes the local deformation state of fluid elements, vortices are more likely aligned with the principal directions of the strain-rate tensor (Davidson, 2015; Misra and Pullin, 1997). If one adopts the scale-similarity ansatz (Bardina et al., 1980), it can be further assumed that the most energetic SGS eddies are oriented primarily by the smallest resolved scale. Motivated from this line of argument, we postulate that there are dynamically more important directions along which the dynamic procedure can be further reduced, namely, the principal directions of the resolved strain rate field. That is, we focus on satisfying the GI along the principal directions of \bar{S}_{ij} only, and examine effectiveness of this assumption. Three closely related formulations will be introduced below.

Dynamic procedures which account for the GI along the principal directions of \bar{S}_{ij} only can be expressed in a general form as

$$C = \frac{\sum_{j=1}^n \langle \alpha_j L'_{jj} M'_{jj} \rangle}{\sum_{j=1}^n \langle \alpha_j M'_{jj} M'_{jj} \rangle}, \quad (4.10)$$

where α_j are proper weights for the j^{th} principal direction, and the prime symbol ($'$) is used to denote tensors represented in the eigen coordinate of \bar{S}_{ij} . For instance, $Q'_{kl} = V_{ki}^{-1} Q_{ij} V_{jl}$, where V_{ij} contains the orthonormal eigenvectors of \bar{S}_{ij} . The first formulation denoted as PDL2 (L_2 norm minimization along principal directions) is defined as $n = 3$ and $\alpha_j = 1$. This approach minimizes the modified cost function $Q = \sum_{j=1}^3 (Q'_{jj})^2$, i.e., the squared sum of the GIE along the principal directions of \bar{S}_{ij} . The second formulation denoted as PDWL2 is defined as $n = 3$ and $\alpha_j = \lambda_j^2$, where λ_j are the eigenvalues of \bar{S}_{ij} . This approach minimizes $Q = \sum_{j=1}^3 (\lambda_j Q'_{jj})^2$, i.e., the squared sum of the GIE weighted according to the level of stretching/compression along the principal directions of \bar{S}_{ij} . A maximally reduced version is where $n = 1$ and $\alpha_j = 1$, which cares only about the direction with the maximum stretch: C is determined from the GI applied along the direction with the maximum positive eigenvalue of \bar{S}_{ij} . This approach (denoted as PDMAX) assumes that the SGS eddies align along the maximal vortex stretching direction of the resolved-scale eddies, and only that direction matters to the SGS dynamics/energetics.

4.2. Flow configuration

The first case considered in the present work is the plane turbulent channel flow with periodic boundary conditions in the streamwise and spanwise directions. DNS results from Moser et al. (1999) and the Johns Hopkins Turbulence Database (JHTDB) (Li et al., 2008; Perlman et al., 2007) are used as reference. The computational domain is set to be $(L_x, L_y, L_z) = (2\pi\delta, 2\delta, 2\pi\delta/3)$ for $Re_\tau = 395$ and $(L_x, L_y, L_z) = (2\pi\delta, 2\delta, \pi\delta)$ for $Re_\tau = 1000$, where x is the streamwise direction, y is the wall-normal direction and z is the spanwise direction. δ is half channel height. The flow is driven by the constant pressure gradient in the streamwise direction.

The second case is the boundary layer created on a flat plate by a time-dependent freestream

velocity vector, whose magnitude is independent of time but whose direction changes at a constant angular velocity (Spalart, 1989). The Reynolds number ($Re_l = U_0 \left(\frac{2}{f\nu}\right)^{1/2}$) is 767. Here, U_0 is freestream velocity magnitude, f is the angular rate of rotation of the freestream velocity vector and ν is the kinematic viscosity. In our numerical simulation, the computational domain is set to be $(L_x, L_y, L_z) = (2\delta, \delta, 2\delta)$, where y is the wall normal direction. $\delta = \frac{u^*}{f}$ is the outer length scale where u^* is the velocity scale as defined in Spalart (1989). The top boundary condition is set to be the rotating velocity vector,

$$U_\infty = U_0 \cos(ft), \quad W_\infty = U_0 \sin(ft) \quad (4.11)$$

Periodic boundary conditions are applied to the two horizontal directions x and z . The flow statistics are computed in the coordinate system that is rotating with the freestream velocity vector. In this coordinate system, the flow is statistically steady.

The third case is the separating flow over periodic hills (Rapp and Manhart, 2011). The computational domain is $(L_x, L_y, L_z) = (9h, 3.035h, 4.5h)$ where h is the height of the hill. x , y and z denote the streamwise, wall-normal and spanwise directions respectively. The Reynolds number based on the hill height h and bulk velocity above the hill crest U_S is $Re_S = U_S h / \nu$. It is related to the domain-averaged bulk Reynolds number ($Re_B = U_B h / \nu$) by a factor of 0.72, $Re_B = 0.72 Re_S$. The flow is driven by a constant mass flow rate. Periodicity is applied to the streamwise and spanwise directions.

4.3. Results and discussion

4.3.1. Turbulent channel flow at $Re_\tau = 395$ and $Re_\tau = 1000$

Figure 4.1 shows the profiles of flow statistics for turbulent channel flow at $Re_\tau = 395$. The grid spacing in wall units is $(\Delta_x^+, \Delta_y^+, \Delta_z^+) = (50, 0.22 \sim 13, 16.5)$. The LES results agree well with DNS (Moser et al., 1999) in terms of mean velocity. As commonly reported in underresolved LES (Bae et al., 2018), a slight overprediction of the streamwise intensity (u_{rms}) and underprediction of the other intensities are observed. All dynamic procedures (the original and PD versions) produce

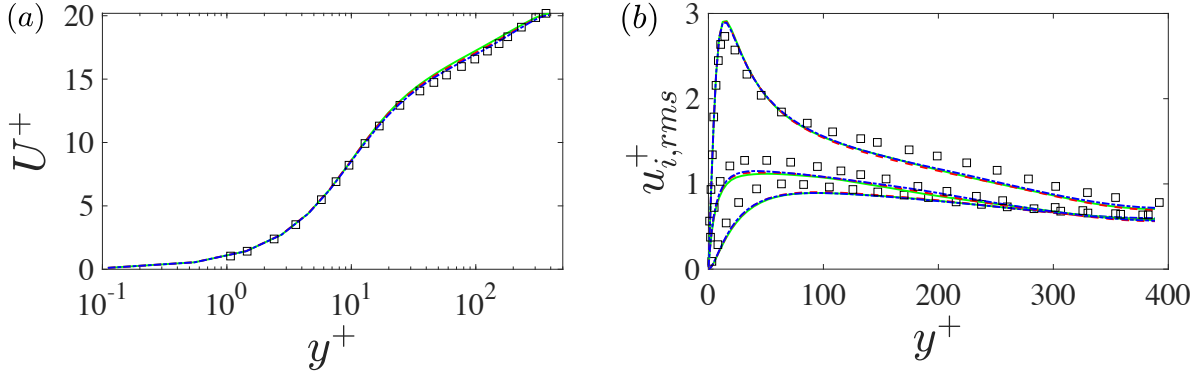


Figure 4.1: Profiles of flow statistics in wall units in turbulent channel flow at $Re_\tau = 395$. (a) Mean streamwise velocity; (b) Turbulence intensities (u_{rms} , v_{rms} and w_{rms}). Black squares, DNS (Moser et al., 1999); green solid line, LES with DSM; red dashed line, LES with PDL2; blue dash-dotted line, LES with PDWL2.

nearly identical result, the PD versions are seen slightly more accurate when zoomed in (see Fig. 4.2). PDL2 and PDWL2 which use only three diagonal components of the GIE tensor in the principal coordinate system of the grid-filtered strain-rate tensor perform equally well compared to the original DSM, which includes all components of the GIE tensor. It should also be noted that the GIE tensor is found not diagonal in the eigen coordinate of \overline{S}_{ij} . The results here imply that not all the components of the GI are equally important. By working on only partial information of the GI, the dynamic model can produce almost identical results to the original DSM results. Although not shown here for brevity, an identical behavior was observed in a channel flow calculation with $Re_\tau = 1000$ using a relatively coarser grid with $(\Delta_x^+, \Delta_y^+, \Delta_z^+) = (100, 0.5 \sim 32, 50)$.

To further highlight how different components of the GIE tensor contribute to the performance of the DSM, another two models are tested in the same turbulent channel flow at $Re_\tau = 395$ as a comparison. The first one includes only the non-principal components (off-diagonal components of the GIE tensor represented in the principal coordinates of \overline{S}_{ij}) in the dynamic procedure. The model is referred to as PDOFF. Another model is PDMAX introduced earlier in Sec. 4.1, which operates only on the principal direction of \overline{S}_{ij} with the maximum stretching. The mean velocity profiles are shown in Fig. 4.2. It can be observed that PDOFF underpredicts the mean velocity, and interestingly, it performs as bad as the no SGS model result. This indicates that the non-principal

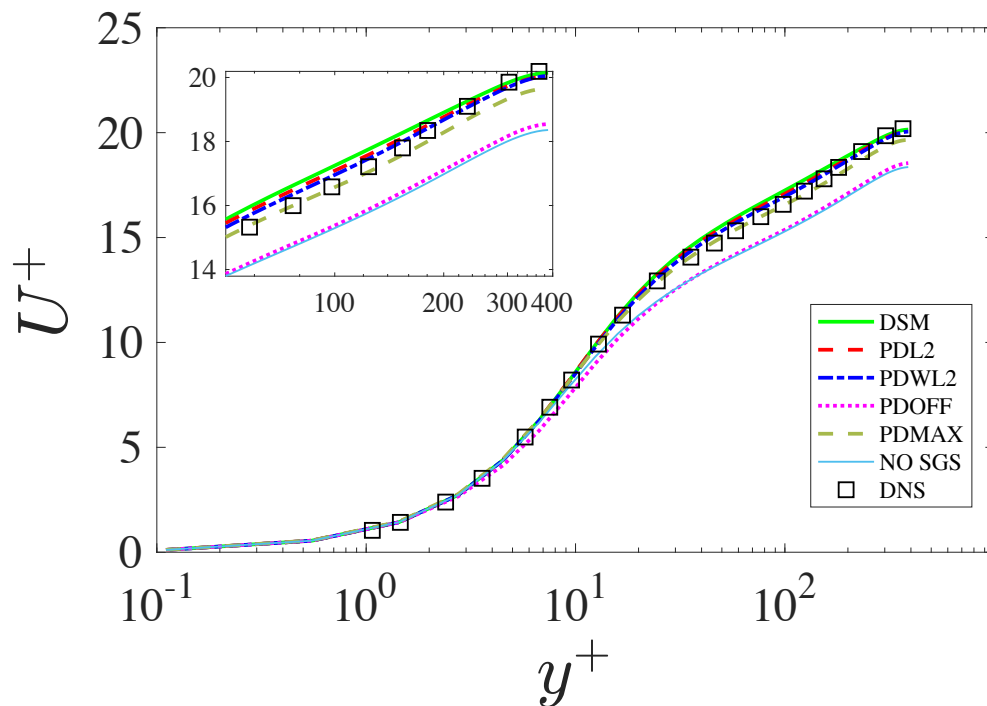


Figure 4.2: Mean velocity profiles of channel flow at $Re_\tau = 395$. Squares, DNS (Moser et al., 1999); green solid line, LES with DSM; red dashed line, LES with PDL2; blue dash-dotted line, LES with PDWL2; magenta dotted line, LES with non-principal components model, PDOFF; olive green dashed line, LES with PDMAX; cyan solid line, no SGS model.

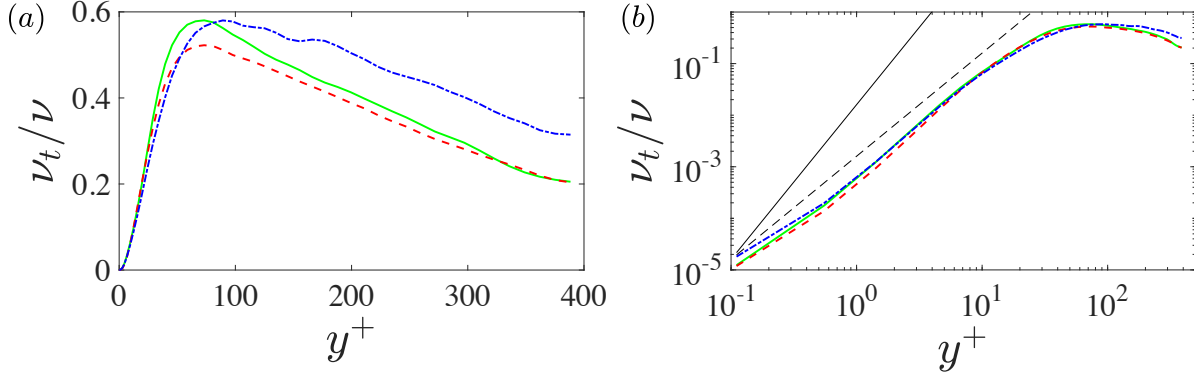


Figure 4.3: Average SGS eddy viscosity from LES of channel flow at $Re_\tau = 395$. SGS eddy viscosity is normalized by kinematic viscosity. (a) Linear scale. (b) Log scale. Green solid line, LES with DSM; red dashed line, LES with PDL2; blue dash-dotted line, LES with PDWL2. In (b), black solid/dashed lines are y^3/y^2 reference lines, respectively.

components have no contribution in the determination of the eddy viscosity. On the other hand, the PDMAX model performs similarly as the original DSM. It has a better agreement with DNS between $50 < y^+ < 110$ but slightly underpredicts the mean velocity for $y^+ > 110$. The reasonably good performance of the PDMAX model is especially surprising given it only considers one component of the GI tensor. This may imply that the SGS model can be further reduced, and the stretching directions are potentially more important than the compressing directions. However, it should be noted that there is a 50% clipping rate in the PDMAX model to avoid negative eddy viscosity. This clipping mostly happens above $y^+ = 50$ and leads to zero eddy viscosity above $y^+ = 100$, which can explain its underprediction for $y^+ > 110$. Figure. 4.3 shows the time-averaged SGS eddy viscosity across the channel. The three SGS models produce similar levels of SGS eddy viscosity. The near-wall SGS eddy viscosity exhibits y^2 behavior instead of y^3 , consistent with the finding of Park and Mahesh (2009) where the SGS eddy viscosity computed from DNS data of channel flow at $Re_\tau = 590$ also exhibited y^2 behavior near the wall.

The effects of different model formulations can also be evaluated through the norm of the GIE tensor Q_{ij} , given by $J = Q_{ij}Q_{ij}$ (Q_{ij} defined in Eq. (4.8)). As pointed out in Park and Mahesh (2009) and Toosi and Larsson (2021), the GIE will be zero for the exact SGS model, and a good SGS model should pursue small GIE. We focus on the coarse LES case of $Re_\tau = 1000$, but the

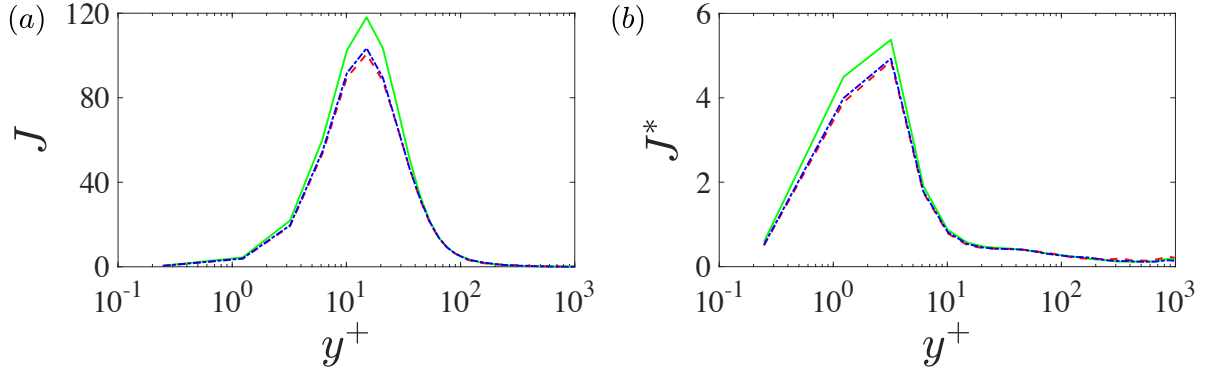


Figure 4.4: Profile of J (the L2 norm of the GIE tensor) along the wall-normal direction in channel flow at $Re_\tau = 1000$. (a) J is not normalized; (b) J is normalized by a combination of mean velocity gradient dU/dy and Reynolds stress $\langle u'u' \rangle$. Green solid line, LES with DSM; red dashed line, LES with PDL2; blue dash-dotted line, LES with PDWL2.

same trend is observed in the $Re_\tau = 395$ case as well. The profile of J in Fig. 4.4(a) shows that the peak location of the GIE is at around $y^+ = 10$ within the buffer layer, consistent with findings of Park and Mahesh (2009). It is found that the GIE from the original DSM is almost identical to the GIE from the PD formulations, except in the buffer layer ($y^+ = 5 \sim 30$). In the buffer layer, about 15% reduction in the peak GIE is observed with the PD formulations as compared to the original DSM. Figure 4.4(b) presents the normalized J profile. Here, J is normalized by $\left(\frac{d\langle U \rangle}{dy} \delta_\nu\right)^4 + \langle u'u' \rangle^2$, where $\delta_\nu = \nu/u_\tau$. This normalization includes the strain rate $\frac{d\langle U \rangle}{dy}$ and Reynolds stress $\langle u'u' \rangle$ which are related to M_{ij} and L_{ij} in the GIE tensor. This normalization produces $J = O(1)$, suggesting that the mixed viscous/turbulent scaling is effective for the GIE. Under such normalization, the peak the error appears around $y^+ = 5$. Overall, the three models produce almost identical GIE.

4.3.2. Three-dimensional turbulent boundary layer

The idea of the reduced dynamic procedure in the DSM is also examined in a 3DTBL. In this flow, the freestream velocity vector is rotating at a constant angular velocity. The flow is statistically steady in the coordinate system rotating with the freestream. x and z denote the directions parallel/perpendicular to the freestream, respectively. Figure 4.5(a) shows the mean velocity magnitude profile in the 3DTBL. For the velocity magnitude, the three different formulations produce almost identical results, showing reasonable agreement with the DNS. A salient feature of 3DTBLs

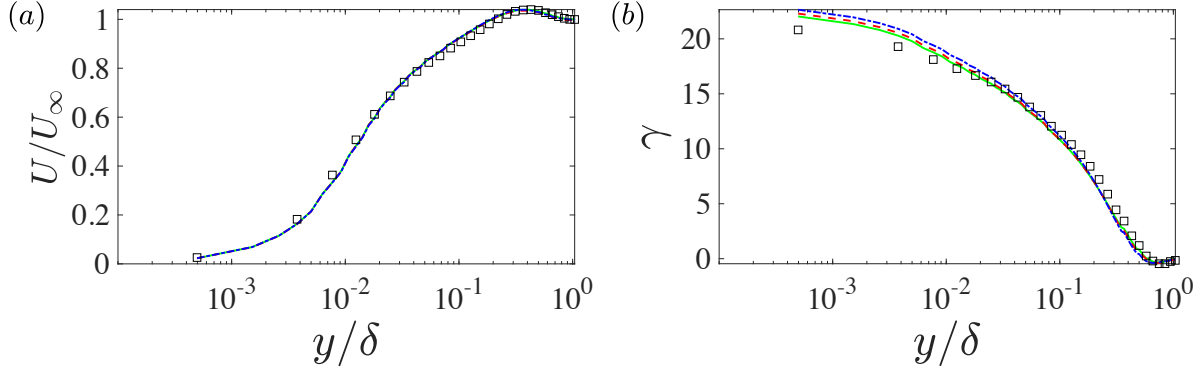


Figure 4.5: Mean velocity in the 3DTBL. (a) Mean velocity magnitude; (b) Mean flow direction $\gamma = \arctan(W/U)$. Squares, DNS (Spalart, 1989); green solid line, LES with DSM; red dashed line, LES with PDL2; blue dash-dotted line, LES with PDWL2.

is the variation of the flow direction with wall distance. The mean flow direction is quantified in Fig. 4.5(b) using the flow angle in wall-parallel planes, $\gamma = \arctan(W/U)$, where U and W are aligned with/perpendicular to the freestream, respectively. The agreement with DNS is slightly worse compared to that of the velocity magnitude. LES solutions have about 3 degrees of discrepancy close to the wall, and a slight underprediction of the flow angle is seen in the outer layer. PDL2 and DSM produce nearly identical predictions. PDWL2 is relatively worse in $y/\delta < 0.1$, but the agreement is still reasonable. Overall, the two modified PD models are as good as the original DSM.

In the following section, the reduced dynamic procedure is also applied to a non-Boussinesq tensor-coefficient SGS model in the same flow. This type of model is better suited for 3DTBLs, because the stress/strain alignment assumption in the Boussinesq eddy viscosity models is invalid in 3DTBLs. Overall, the PD formulation shows slightly improved performance compared to the original dynamic tensor-coefficient SGS model of Agrawal et al. (2022). Details related to this aspect can be found in Sec. 4.4.

4.3.3. Flow over periodic hills

Figure 4.6 shows the the mean streamwise velocity in the separating flow over periodic hills predicted with the DSM with different dynamic procedures. Good agreements is found with the experiment in all three SGS models. The largest discrepancy is observed at $x/h = 0.05$ close to the separation

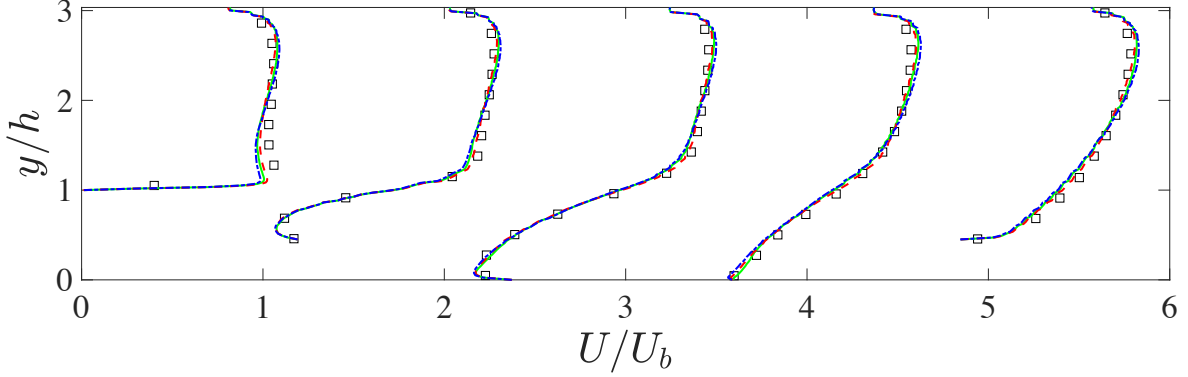


Figure 4.6: Streamwise mean velocity profiles in the flow over periodic hills ($Re = 10595$) from $x/h = 0.05, 1.00, 2.00, 4.00, 8.00$. Profiles are shifted along the abscissa by 1.2. Black squares, experiment (Rapp and Manhart, 2011); green solid line, LES with DSM; red dashed line, LES with PDL2; blue dash-dotted line, LES with PDWL2.

point ($x/h \approx 0.2$). At this location, PDL2 shows slightly better performance than the other two formulations.

4.4. Application to dynamic tensor coefficient Smagorinsky model

Reduction of the dynamic procedure onto the principal directions of the strain rate tensor can be applied to the dynamic tensor coefficient Smagorinsky model (DTCSM) (Agrawal et al., 2022) as well. The DTCSM models the SGS stress as

$$\tau_{ij} - \frac{\tau_{kk}}{3}\delta_{ij} = -(C_{ik}\bar{S}_{kj} + C_{jk}\bar{S}_{ki})|\bar{S}|\Delta^2, \quad (4.12)$$

where C_{ij} is the tensor of model coefficients. For the DTCSM, the Germano identity is defined as

$$L_{ij} = (C_{ik}\Delta^2 M_{kj} + C_{jk}\Delta^2 M_{ki}). \quad (4.13)$$

Agrawal et al. (2022) imposed the trace-free requirement on the model leading to the following constraints,

$$C_{11} = C_{22} = C_{33}; \quad C_{ij} = -C_{ji} (i \neq j), \quad (4.14)$$

and the 4 independent coefficients were determined to best satisfy 6 constraints from the GI in a L_2 sense. The identity can be rewritten as

$$\begin{pmatrix} L_{11} \\ L_{22} \\ L_{33} \\ L_{12} \\ L_{13} \\ L_{23} \end{pmatrix} = \begin{pmatrix} 2M_{11} & 2M_{12} & 2M_{13} & 0 \\ 2M_{22} & -2M_{12} & 0 & 2M_{23} \\ 2M_{33} & 0 & -2M_{13} & -2M_{23} \\ 2M_{12} & M_{22} - M_{11} & M_{23} & M_{13} \\ 2M_{13} & M_{23} & M_{33} - M_{11} & -M_{12} \\ 2M_{23} & -M_{13} & -M_{12} & M_{33} - M_{22} \end{pmatrix} \begin{pmatrix} C_{11} \\ C_{12} \\ C_{13} \\ C_{23} \end{pmatrix} \quad (4.15)$$

with Δ^2 being absorbed into the coefficients. Similar to the formulation described in Sec. 4.1, the GIE tensor $Q_{ij} = L_{ij} - (C_{ik}\Delta^2 M_{kj} + C_{jk}\Delta^2 M_{ki})$ for the DTCSM can be transformed into the principal coordinate system of the filtered strain-rate tensor (\bar{S}_{ij}). The PD-version of the DTCSM then determines model coefficients by enforcing the GI along the principal directions of \bar{S}_{ij} only (the diagonal components of the transformed GIE tensor).

$$\begin{pmatrix} L'_{11} \\ L'_{22} \end{pmatrix} = \begin{pmatrix} 2M'_{11} & 2M'_{12} & 2M'_{13} & 0 \\ 2M'_{22} & -2M'_{12} & 0 & 2M'_{23} \end{pmatrix} \begin{pmatrix} C_{11} \\ C_{12} \\ C_{13} \\ C_{23} \end{pmatrix}. \quad (4.16)$$

It can be observed readily that there are 4 unknown variables and but only two constraints. To close the system, we introduce an additional assumption on the coefficients operating on the non-principal components of M_{ij} , letting $C_{12} = C_{13} = C_{23}$. This leads to a closed 2x2 system from which the model coefficients can be determined.

$$\begin{pmatrix} L'_{11} \\ L'_{22} \end{pmatrix} = \begin{pmatrix} 2M'_{11} & 2M'_{12} + 2M'_{13} \\ 2M'_{22} & -2M'_{12} + 2M'_{23} \end{pmatrix} \begin{pmatrix} C_{11} \\ C_{12} \end{pmatrix}. \quad (4.17)$$

The DTCSM and its PD-variant (denoted here as DTCSM-PD) is applied to the 3DTBL case

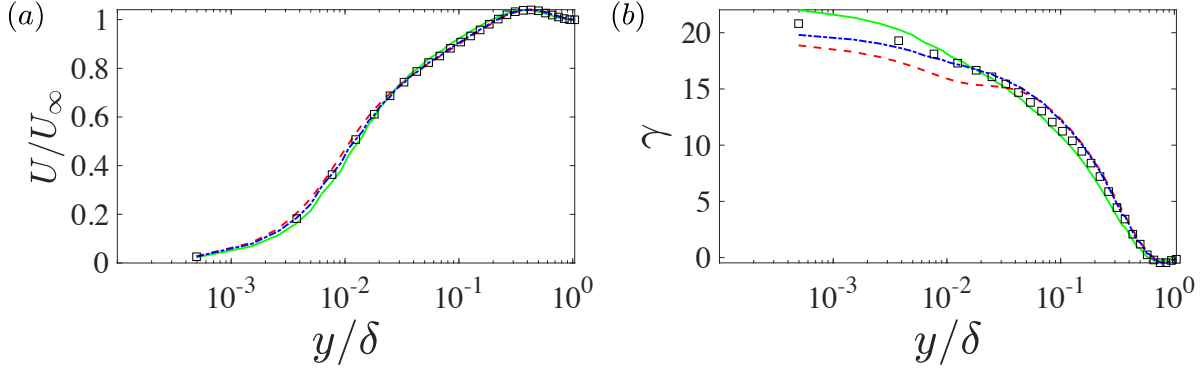


Figure 4.7: Mean velocity in the 3DTBL. (a) Mean velocity magnitude; (b) Mean flow direction $\gamma = \arctan(W/U)$. Black squares, DNS; green solid line, LES with DSM; red dashed line, LES with DTCSM; blue dash-dotted line, LES with DTCSM-PD.

considered in Sec. 4.3.2. Figure 4.7 shows the profiles of the mean velocity magnitude and flow direction. For the velocity magnitude, the two tensor coefficient SGS models have a very good agreement with the DNS, while the DSM has a slight discrepancy (under/over prediction in the near-wall/bulk regions). For the flow direction, it is clear that the DTCSM-PD has the best performance close to the wall, where the DSM overpredicts and the DTCSM underpredicts the flow angle. For $y/\delta > 0.2$, the DTCSM and the DTCSM-PD produce almost identical results for the flow direction and they agree well with the DNS. The original DSM slightly underpredicts the flow angle at $y/\delta > 0.2$. Overall, we again confirm that reduction of the dynamic procedure along the principal direction is as effective as the original DTCSM. In fact, the DTCSM-PD has the best prediction of the mean velocity. We do note that the choice of the additional constraints ($C_{12} = C_{13} = C_{23}$) is somewhat arbitrary. Other choices are possible, and how we close the system may affect the performance of the model. The purpose of this section is to provide a potential extension of the conclusion in the main text towards more comprehensive SGS models.

CHAPTER 5

CONCLUSION

The WMLES has emerged as a promising numerical tool for scale-resolving simulations of high Reynolds number wall-bounded turbulent flows in practical engineering applications. However, the assessment of wall model performance in nonequilibrium turbulent boundary layers is still lacking. In the present work, we have studied a spatially-developing pressure-driven 3DTBL over the floor of a square duct with a 30° bend using WMLES. The major focus of this study is to contrast the performance of three commonly used wall models in a high Reynolds number pressure-driven 3DTBL.

These models represent varying degrees of physical fidelity: the EQWM solves the simplified boundary-layer equations which neglect all nonequilibrium effects and assume the flow is unidirectional in the wall-modeled region; the PDE NEQWM solves unsteady 3D RANS equations which maintain much of the nonequilibrium effects; the integral NEQWM represents a compromise between the two models. Algebraic complexity is kept low thanks to the presumed velocity profile, while the nonequilibrium effect is represented by the linear perturbation to the logarithmic law of the wall.

The mean-flow statistics and the Reynolds stresses are predicted reasonably well by the WMLES under the current grid resolutions, which are too coarse for the no-slip LES. The more comprehensive PDE NEQWM does show improvement against the integral NEQWM (which is in turn better than the EQWM) in predicting the direction of mean wall shear stress. The error in the local wall shear force direction accumulates along the surface streamlines, leading to significant difference of the surface flow at the end of the duct. Budget analyses have been conducted to elucidate precise mechanisms by which the three wall models produce different predictions of the wall shear stress directions given almost identical inputs. For the present flow, the surface flow direction is shown to have separable contributions from the equilibrium part of the wall models and the integrated nonequilibrium effects (advection and pressure transports). It was shown that difference in how the

cross-flow component of the nonequilibrium contribution is modeled leads to different behaviors of the models. Additionally, the pressure gradient and the advection are shown to have a competing effect in deflecting the surface flow within the bend. Although these terms largely cancel out each other, neglecting any of them produces large errors in the surface flow direction, and a subtle balance between the two appears to be crucial in prediction of the surface flow.

However, such difference in the wall shear stress direction predicted by the wall models appears to be not felt by the (outer) LES solution. The three wall models produce almost the same mean velocity and Reynolds stresses profiles. A possible explanation for this phenomenon comes from the nature of the pressure-driven 3DTBL. In the duct flow under consideration, the mean-flow three-dimensionality in the outer layer is largely controlled by the “inviscid skewing” mechanism, which is not affected by the near wall viscous effects. In this class of 3DTBL, the outer-layer mean-flow appears to be robustly set up by the inviscid effect, provided that the momentum drain by the wall is specified with reasonable accuracy only (in particular, its magnitude rather than the direction).

The characteristics of the 3DTBL are also analyzed. The anisotropy of turbulence along the wall-normal direction is investigated with the Lumley triangle. Compared to the 2DTBL, a large inward pointing sharp corner is presented in the Lumley triangle plot of 3DTBL in the downstream section. This large sharp corner represents a non-monotonic decrease of anisotropy for increasing wall distance. When the mean crossflow is generated by the inviscid effect (reorientation of spanwise vorticity), the relation between spanwise and streamwise velocity in the local freestream coordinate system in the outer part of the boundary layer shows as a straight line predicted by the SWH formula. In the present duct flow, the outer LES results show good agreement with the SWH formula, which shows that the “inviscid skewing” mechanism is the major effect for generating mean three-dimensionality in the outer layer. The triangular plot of the inner wall-model solution reveals that the PDE NEQWM is most capable of representing the change in the flow direction along the wall-normal direction. The EQWM is most restrictive in this sense with its unidirectional flow assumption. The integral NEQWM is in between the two.

Grid convergence is another problem to be addressed for WMLES. It is not well understood (and

not attempted as rigorously as resolved LES) due to the high computational cost and seemingly conflicting objectives of grid convergence and wall modeling. This motivates us to investigate the grid convergence trend for WMLES. It is proposed that the wall model itself can be considered as an input-output system that takes the input from the LES at the matching location, and produces the wall stress as the output. Furthermore, well-resolved outer LES solutions at the matching location should provide unchanged input to the wall model upon further grid refinement, and the wall model should also produce unchanged output. This situation can be considered as the grid-converged state for WMLES—although the grid-converged solution is not necessarily accurate. Then, it is natural to hypothesize that the wall model matching height is critical for the convergence rate, since the attached eddies scale as their distance from the wall and resolving attached eddies at different wall-normal heights require different grid resolutions.

The proposition is tested in two different attached turbulent boundary layers, namely, the turbulent channel flow and a 3DTBL with its freestream velocity vector rotating at constant angular velocity. In both cases, it is found that the WMLES converges in terms of the wall model output (i.e. the wall-shear stress) at coarser grid resolutions when the wall model matching location is farther away from the wall. The convergence trends for different wall model matching heights collapse better when the grid spacing is normalized by the matching height.

The analysis of LES quantities provides another perspective on the grid convergence. While the grid convergence behavior of the mean velocity is similar to that of the skin friction from the wall model, the grid convergence of turbulence intensities is slower than that of the mean quantities. It is also noted that the error of the turbulence intensity does not have a clear dependence on the wall model matching height. This different behavior is explained based on the attached eddy theory. It is shown that the attached eddies have been resolved at the grid resolutions at which the mean flow converged. However, the small-scale eddies which contribute to the Reynolds stress require finer grid resolutions for convergence. An approximate estimation based on the ratio of the spectral energy being resolved is that about 80% of the energy carried by the small-scale eddies (as classified in Hu et al. (2020)) is resolved to expect convergence of the streamwise Reynolds normal stress. This

corresponded to $\Delta^+ \approx 50$ in channel flow at $Re_\tau = 1000$, starting to approach the wall-resolved limit.

The present work also invites us to think about what approaches to take on h_{wm} during the grid refinement, and what its implication is. If one is to reduce the extent of the wall-modeled region in proportion to the level of grid refinements, WMLES may be expected to converge to the WRLES and then to the DNS: In the limit of DNS-like resolution in the LES, wall models which can represent the viscous sublayer will produce the linear flux based on the no-slip wall and the LES data at $y = h_{wm}$, and this will be little different from direct application of the no-slip condition in the LES codes (frequently, the first order linear approximation is used for application of the no-slip condition.) This aspect may be considered ideal on one hand, as the model contribution eventually vanishes, providing WMLES with a natural convergence path to the first-principle based methods. On the other hand, this limit in practice can never be reached for high Reynolds number flows due to the cost, and the convergence will be achieved at an extreme cost. Conversely, if one is to maintain the fixed extent of the wall modeled region (h_{wm} unchanged) during the refinement, the convergence of WMLES will likely take place at much coarser resolution before reaching the WRLES limit. The converged result however may contain error (potentially depending on h_{wm}), originating primarily from invalid modeling assumptions in wall models. This situation could be reminiscent of RANS or explicitly filtered LES, where the model contributions remain constant irrespective of grid resolution. An interesting proposition along this line could be that one may attempt converging WMLES at a desired target grid resolution by selecting h_{wm} somewhat larger than the target grid spacing. This can be practically useful for ensuring convergence of WMLES at the finest affordable grid resolution, or in the absence of experimental or truth data. The converged result might depend on h_{wm} , and wall models which are known to have less sensitivities to the matching location could be preferred.

Future work regarding the grid convergence in WMLES can be extended to the separated turbulent boundary layers, where the proposition herein based largely on the notion of wall attached eddies may require revision, and different practical guidelines could be proposed. Lastly, effects of grid

topology and anisotropy can be explored.

Lastly, we revisit the dynamic procedure of DSM. Motivated from vorticity dynamics, a hidden mechanism at work in the success of dynamic LES SGS models is explored. Based on the assumption that the SGS eddies tend to be aligned with the principal stretching/compression directions of the resolved flow field, we postulate that only a few elements of the Germano identity, pertaining to the principal directions of the resolved strain-rate, matter in the dynamic procedure to determine the model coefficient.

Some principal-direction (PD) variants of the DSM based on this idea are tested in canonical turbulent channel flows, a turbulent boundary layer with mean-flow three-dimensionality, and a separating flow over periodic hills. In all the cases, PD formulations produced almost identical results as the original DSM. These results demonstrate that not all components of the Germano identity matters, and that satisfaction of the Germano identity along the principal directions of the resolved strain-rate tensor might be the essence of the dynamic procedure. This builds the physical connection between the Germano identity and the resolved flow field, and can potentially help in understanding why the dynamic model succeeds in the SGS modeling effort.

APPENDIX A

DERIVATION FOR SWH FORMULA

Below, we delineate the steps for deriving the SWH formula. Equation A.1 is the transport equation for the mean streamwise vorticity Bradshaw (1987), where the terms on the right hand side of this equation represent the contributions from vortex stretching, vortex tilting, Reynolds stress, and viscous effect, in the shown order. The "inviscid skewing" mechanism generates the mean three-dimensionality by reorienting the mean spanwise vorticity as the streamwise vorticity. If we assume that the "inviscid skewing" mechanism is the dominant mechanism for the mean three-dimensionality, the third term on the right hand side would contribute the most to the generation of mean streamwise vorticity. Keeping only the dominant terms in this equation leads to equation A.2, where the second equality in this equation is obtained by assuming the mean wall-normal vorticity to be zero ($\Omega_y = \frac{\partial U}{\partial z} - \frac{\partial W}{\partial x} = 0$).

$$\begin{aligned}
 U \frac{\partial \Omega_x}{\partial x} + V \frac{\partial \Omega_x}{\partial y} + W \frac{\partial \Omega_x}{\partial z} &= \Omega_x \frac{\partial U}{\partial x} + \Omega_y \frac{\partial U}{\partial y} + \Omega_z \frac{\partial U}{\partial z} \\
 + \left(\frac{\partial^2}{\partial y^2} - \frac{\partial^2}{\partial z^2} \right) (-\overline{v'w'}) &+ \frac{\partial^2}{\partial y \partial z} (\overline{v'^2} - \overline{w'^2}) + \nu \nabla^2 \Omega_x
 \end{aligned} \tag{A.1}$$

$$U \frac{\partial \Omega_x}{\partial x} = \Omega_z \frac{\partial U}{\partial z} = \Omega_z \frac{\partial W}{\partial x} \tag{A.2}$$

Reorganizing equation A.2 by dividing $U\Omega_z$ gives equation A.3. Assuming that Ω_z and U vary little in the streamwise direction, we can re-express this equation as equation A.4.

$$\frac{1}{\Omega_z} \frac{\partial \Omega_x}{\partial x} = \frac{1}{U} \frac{\partial W}{\partial x} \tag{A.3}$$

$$\frac{\partial}{\partial x} \frac{\Omega_x}{\Omega_z} = \frac{\partial}{\partial x} \frac{W}{U} \tag{A.4}$$

Equation A.4 is referred to as the SWH relation in the global coordinate system. Equation A.2 in the local freestream coordinate system is given by equation A.5 Horlock and Lakshminarayana (1973):

$$U_s \frac{\partial \Omega_s}{\partial s} + \frac{U_s \Omega_n}{R} = \Omega_s \frac{\partial U_s}{\partial s} + \Omega_n \frac{\partial U_s}{\partial n} + \Omega_b \frac{\partial U_s}{\partial b}, \quad (\text{A.5})$$

here, (s, n, b) represents the streamwise, spanwise and wall normal directions in the local freestream coordinate system, respectively. Since $\Omega_n = \frac{\partial U_s}{\partial b}$ and $\Omega_b = -(\frac{\partial U_s}{\partial n} + \frac{U_s}{R})$, we get,

$$\frac{\partial}{\partial s} \left(\frac{\Omega_s}{U_s} \right) = -\frac{2\Omega_n}{U_s R} \quad (\text{A.6})$$

Using the relation $Rd\theta = ds$, equation A.6 can be re-written as equation A.7, which is the SWH formula in the local freestream coordinate system.

$$\frac{d\Omega_s}{\Omega_n} = -2d\theta. \quad (\text{A.7})$$

Integrating equation A.7 along the streamline and substituting the definitions of vorticity, we get,

$$\frac{U_n}{U_e} = 2\gamma_e \left(1 - \frac{U_s}{U_e} \right). \quad (\text{A.8})$$

When the "inviscid skewing" mechanism is the dominant generation mechanism of the mean streamwise vorticity (mean three-dimensionality), U_n plotted against U_s under the local freestream coordinates will form a straight line. Plotting U_n against U_s in the duct flow and the transient 3D channel flow, we can find that the above relation is satisfied in the duct flow but not in the 3D channel flow. This indicates the "inviscid skewing" mechanism is the dominant contribution to the mean three-dimensionality in the outer part of the boundary layer in the duct flow. While in the transient 3D channel flow, "inviscid skewing" does not exist, i.e. the vortex tilting term is zero.

BIBLIOGRAPHY

- R. Agrawal, M. P. Whitmore, K. P. Griffin, S. T. Bose, and P. Moin. Non-boussinesq subgrid-scale model with dynamic tensorial coefficients. *Phys. Rev. Fluids*, 7:074602, 2022.
- H. J. Bae, A. Lozano-Duran, S. T. Bose, and P. Moin. Turbulence intensities in large-eddy simulation of wall-bounded flows. *Phys. Rev. Fluids*, 3(1):014610, 2018.
- H. J. Bae, A. Lozano-Durán, S. T. Bose, and P. Moin. Dynamic slip wall model for large-eddy simulation. *J. Fluid Mech.*, 859:400–432, 2019.
- E. Balaras, C. Benocci, and U. Piomelli. Two-layer approximate boundary conditions for large-eddy simulations. *AIAA J.*, 34:1111–1119, 1996.
- J. Bardina, J. Ferziger, and W. C. Reynolds. Improved subgrid-scale models for large-eddy simulation. In *13th fluid and plasmadynamics conference*, page 1357, 1980.
- Y. Bentalb and M. A. Leschziner. The structure of a three-dimensional boundary layer subjected to streamwise-varying spanwise-homogeneous pressure gradient. *Int. J. Heat. Fluid. Fl.*, 43:109–119, 2013.
- L. R. Bissonnette and G. L. Mellor. Experiments on the behaviour of an axisymmetric turbulent boundary layer with a sudden circumferential strain. *J. Fluid Mech.*, 63:369–413, 1974.
- J. Bodart and J. Larsson. Wall-modeled large eddy simulation in complex geometries with application to high-lift devices. *Annual Research Briefs* in Center for Turbulence Research, Stanford University, pages 37–48, 2011.
- J. Bodart and J. Larsson. Wall-modeled large eddy simulation of the mcdonnell-douglas 30p/30n high-lift airfoil in near-stall conditions. *30th AIAA Applied Aerodynamic Conference*, page 3022, 2012.
- S. T. Bose and P. Moin. A dynamic slip boundary condition for wall-modeled large-eddy simulation. *Phys. Fluids*, 26:015104, 2014.
- S. T. Bose and G. I. Park. Wall-modeled large-eddy simulation for complex turbulent flows. *Ann. Rev. Fluid Mech.*, 50:535–561, 2018.
- S. T. Bose, P. Moin, and D. You. Grid-independent large-eddy simulation using explicit filtering. *Phys. Fluids*, 22:105103, 2010.
- P. Bradshaw. Turbulent secondary flows. *Ann. Rev. Fluid Mech.*, 19:53–74, 1987.
- P. Bradshaw and N. Pontikos. Measurements in the turbulent boundary layer on an ‘infinite’ swept

- wing. *J. Fluid Mech.*, 159:105–130, 1985.
- J. M. Bruns, H. H. Fernholz, and P. A. Monkewitz. An experimental investigation of a three-dimensional turbulent boundary layer in an ‘s’-shaped duct. *J. Fluid Mech.*, 393:175–213, 1999.
- W. Cabot and P. Moin. Approximate wall boundary conditions in large-eddy simulation of high reynolds number flow. *Flow, Turbul. Combust.*, 63:269–291, 2000.
- C. J. Chesnakas and R. L. Simpson. Full three-dimensional measurements of the cross-flow separation region of a 6:1 prolate spheroid. *Exp. Fluids*, 17:68–74, 1994.
- M. Cho, A. Lozano-Durán, P. Moin, and G. I. Park. Wall-modeled large-eddy simulation of turbulent boundary layers with mean-flow three-dimensionality. *AIAA J.*, 59:1707–1717, 2021.
- H. Choi and P. Moin. Grid-point requirements for large eddy simulation: Chapman’s estimates revisited. *Phys. Fluids*, 24:011702, 2012.
- D. Chung and D. I. Pullin. Large-eddy simulation and wall modelling of turbulent channel flow. *J. Fluid Mech.*, 631:281–309, 2009.
- G. N. Coleman, J. Kim, and P. R. Spalart. A numerical study of strained three-dimensional wall-bounded turbulence. *J. Fluid Mech.*, 416:75–116, 2000.
- G. N. Coleman, C. L. Rumsey, and P. R. Spalart. Numerical study of a turbulent separation bubble with sweep. *J. Fluid Mech.*, 880:684–706, 2019.
- P. A. Davidson. *Turbulence: an introduction for scientists and engineers*. Oxford university press, 2015.
- J. W. Deardorff. The numerical study of three dimensional turbulent channel flow at large Reynolds numbers. *J. Fluid Mech.*, 41:453–480, 1970.
- D. B. Degraaff and J. K. Eaton. Reynolds-number scaling of the flat-plate turbulent boundary layer. *J. Fluid Mech.*, 422:319–346, 2000.
- F. M. Denaro. On the relevance of the type of contraction of the germano identity in the new integral-based dynamic smagorinsky model. *Comput. Fluids*, 72:30–45, 2013.
- D. M. Driver and S. K. Hebbar. Three-dimensional shear-driven boundary layer flow with streamwise adverse pressure gradient. *AIAA J.*, page 3661, 1988.
- G. Eitel-Amor, R. Orlu, and P. Schlatter. Simulation and validation of a spatially evolving turbulent boundary layer up to $re_\theta = 8300$. *Int. J. Heat. Fluid. Fl.*, 47:57–69, 2014.
- H. H. Fernholz and P. J. Finley. The incompressible zero-pressure-gradient turbulent boundary

- layer: An assessment of the data. *Prog. Aerospace Sci.*, 32:245–311, 1996.
- K. Flack and J. Johnston. Near-wall flow in a three-dimensional turbulent boundary layer on the endwall of a rectangular bend. *32nd Aerospace Sciences Meeting and Exhibit*, page 405, 1994.
- M. Fowler, T. A. Zaki, and C. Meneveau. A lagrangian relaxation towards equilibrium wall model for large eddy simulation. *J. Fluid Mech.*, 934:A44, 2022.
- W. Gao, W. Zhang, W. Cheng, and R. Samtaney. Wall-modelled large-eddy simulation of turbulent flow past airfoils. *J. Fluid Mech.*, 873:174–210, 2019.
- M. Germano, U. Piomelli, P. Moin, and W. Cabot. A dynamic subgrid-scale eddy viscosity model. *Phys. Fluids*, 3:1760, 1991.
- S. Ghosal. An analysis of numerical errors in large-eddy simulations of turbulence. *J. Comput. Phys.*, 125:187–206, 1996.
- S. Ghosal, T. S. Lund, P. Moin, and K. Akselvoll. A dynamic localization model for large-eddy simulation of turbulent flows. *J. Fluid Mech.*, 286:229–255, 1995.
- K. Goc, S. T. Bose, and P. Moin. Wall-modeled large-eddy simulation of aircraft in landing configuration. *Annual Research Briefs in Center for Turbulence Research*, Stanford University, pages 3–14, 2019.
- K. Goc, S. T. Bose, and P. Moin. Large eddy simulation of the nasa high-lift common research model. *AIAA SciTech*, pages 2022–1556, 2022.
- K. A. Goc, O. Lehmkuhl, G. I. Park, S. T. Bose, and P. Moin. Large eddy simulation of aircraft at affordable cost: a milestone in computational fluid dynamics. *Flow*, 1, 2021.
- J. Graham, K. Kanov, X. I. A. Yang, M Lee, N. Malaya, C. C. Lalescu, R. Burns, G. Eyink, A. Szalay, R. D. Moser, and C. Meneveau. A web services accessible database of turbulent channel flow and its use for testing a new integral wall model for les. *J. Turbul.*, 17(2):181–215, 2016.
- G. Grötzbach. Direct numerical and large eddy simulation of turbulent channel flows. *Encyclopedia of fluid mechanics*, 6:1337–1391, 1987.
- W. R. Hawthorne. Secondary circulation in fluid flow. *Proc. R. Soc. Lond. A*, 206:374–387, 1951.
- I. Hayat and G. I. Park. Numerical implementation of efficient grid-free integral wall models in unstructured-grid les solvers. *arXiv preprint arXiv:2111.02542*, 2021.
- I. Hayat and G. I. Park. Efficient spectral implementation of ode wall model and the extension of integral wall model to unstructured les solvers. *J. Comput. Phys.*, 487:112175, 2023.

- S. Hickel, E. Touber, J. Bodart, and J. Larsson. A parametrized non-equilibrium wall-model for large-eddy simulations. *Proceedings of the Summer Program 2012, Center for Turbulence Research, Stanford Univ., Stanford, CA*, pages 229–240, 2012.
- J. H. Horlock and B. Lakshminarayana. Secondary flows: theory, experiment, and application in turbomachinery aerodynamics. *Ann. Rev. Fluid Mech.*, 5:247–280, 1973.
- S. Hoyas and J. Jimenez. Scaling of the velocity fluctuations in turbulent channels up to $re_\tau = 2003$. *Phys. Fluids*, 18:011702, 2006.
- R. Hu, X. Yang, and X. Zheng. Wall-attached and wall-detached eddies in wall-bounded turbulent flows. *J. Fluid Mech.*, 885:A30, 2020.
- X. Hu, I. Hayat, and G. I. Park. Wall-modelled large-eddy simulation of three-dimensional turbulent boundary layer in a bent square duct. *J. Fluid Mech.*, 960:A29, 2023.
- P. S. Iyer and M. R. Malik. Wall-modeled les of flow over a gaussian bump. *AIAA SciTech*, pages 2021–1438, 2021.
- J. Jiménez and R. D. Moser. Les: where are we and what can we expect? *AIAA J.*, 38:605–612, 2000.
- J. Johnston and K. Flack. Review—advances in three-dimensional turbulent boundary layers with emphasis on the wall-layer regions. *J. Fluids Eng.*, pages 219–232, 1996.
- J. P. Johnston. On the three-dimensional turbulent boundary layer generated by secondary flow. *J. Basic Eng.*, 82:233–246, 1960.
- S. Kawai and K. Asada. Wall-modeled large-eddy simulation of high reynolds number flow around an airfoil near stall condition. *Comput. Fluids*, 85:105–113, 2013.
- S. Kawai and J. Larsson. Wall-modeling in large eddy simulation: Length scales, grid resolution, and accuracy. *Phys. Fluids*, 24:015105, 2012.
- S. Kawai and J. Larsson. Dynamic non-equilibrium wall-modeling for large eddy simulation at high reynolds numbers. *Phys. Fluids*, 25:015105, 2013.
- Y. Khalighi, J. W. Nichols, F. Ham, S. K. Lele, and P. Moin. Unstructured large eddy simulation for prediction of noise issued from turbulent jets in various configurations. *17th AIAA/CEAS Aeroacoustics Conference 2011 (32nd AIAA Aeroacoustics Conference)*, 101:2886, 2011.
- M. Klein, A. Sadiki, and J. Janicka. A digital filter based generation of inflow data for spatially developing direct numerical or large eddy simulations. *J. Comput. Phys.*, 186:652–665, 2003.
- J. Larsson. Simple inflow sponge for faster turbulent boundary-layer development. *AIAA J.*, 59:

1–3, 2021.

- J. Larsson, S. Kawai, J. Bodart, and I. Bermejo-Moreno. Large eddy simulation with modeled wall-stress: recent progress and future directions. *Mech. Eng. Rev.*, 3:15–00418, 2016.
- Y. Li, E. Perlman, M. Wan, Y. Yang, C. Meneveau, R. Burns, S. Chen, A. Szalay, and G. Eyink. A public turbulence database cluster and applications to study lagrangian evolution of velocity increments in turbulence. *J. Turbul.*, 9:No. 31, 2008.
- D. K. Lilly. A proposed modification of the germano subgrid-scale closure method. *Phys. Fluids*, 4: 633, 1992.
- H. S. Littell and J. K. Eaton. Experimental investigation of the three-dimensional boundary layer on a rotating disk. *Turbulent Shear Flows 8*, pages 403–414, 1993.
- R. P. Lohmann. The response of a developed turbulent boundary layer to local transverse surface motion. *J. Fluids Eng.*, 98:354–363, 1976.
- A. Lozano-Durán and H. J. Bae. Error scaling of large-eddy simulation in the outer region of wall-bounded turbulence. *J. Comput. Phys.*, 392:532–555, 2019.
- A. Lozano-Durán, M. G. Giometto, G. I. Park, and P. Moin. Non-equilibrium three-dimensional boundary layers at moderate reynolds numbers. *J. Fluid Mech.*, 883:A20, 2020.
- A. Lozano-Durán, S. T. Bose, and P. Moin. Performance of wall-modeled les with boundary-layer-conforming grids for external aerodynamics. *AIAA J.*, pages 1–20, 2021.
- T. S. Lund. The use of explicit filters in large eddy simulation. *Compos. Math.*, 46:603, 2003.
- I. Marusic and J. P. Monty. Attached eddy model of wall turbulence. *Ann. Rev. Fluid Mech.*, 51: 49–74, 2019.
- C. Meneveau and J. Katz. Scale-invariance and turbulence models for large-eddy simulation. *Ann. Rev. Fluid Mech.*, 32:1–32, 2000.
- C. Meneveau, T. S. Lund, and W. H. Cabot. A lagrangian dynamic subgrid-scale model of turbulence. *J. Fluid Mech.*, 319:353–385, 1996.
- J. Meyers and P. Sagaut. Is plane-channel flow a friendly case for the testing of large-eddy simulation subgrid-scale models? *Phys. Fluids*, 19:048105, 2007.
- A. Misra and D. I. Pullin. A vortex-based subgrid stress model for large-eddy simulation. *Phys. Fluids*, 9(8):2443–2454, 1997.
- Parviz Moin, Kyle Squires, W Cabot, and Sangsan Lee. A dynamic subgrid-scale model for com-

- pressible turbulence and scalar transport. *Physics of Fluids A: Fluid Dynamics*, 3(11):2746–2757, 1991.
- Y. Morinishi and O. V. Vasilyev. A recommended modification to the dynamic two-parameter mixed subgrid scale model for large eddy simulation of wall bounded turbulent flow. *Phys. Fluids*, 13: 3400, 2001.
- R. D. Moser, J. Kim, and N. N. Mansour. Direct numerical simulation of turbulent channel flow up to $re_\tau = 590$. *Phys. Fluids*, 11:943–945, 1999.
- H Owen, G. Chrysokentis, M. Avila, D. Mira, G. Houzeaux, R. Borrell, J. C. Cajas, and O. Lehmkuhl. Wall-modeled large-eddy simulation in a finite element framework. *Int. J. Numer. Methods Fluids*, 92:20–37, 2020.
- G. I. Park. Wall-modeled large-eddy simulation of a high reynolds number separating and reattaching flow. *AIAA J.*, 55:3709—3721, 2017.
- G. I. Park and P. Moin. An improved dynamic non-equilibrium wall-model for large eddy simulation. *Phys. Fluids*, 26:015108, 2014.
- G. I. Park and P. Moin. Numerical aspects and implementation of a two-layer zonal wall model for les of compressible turbulent flows on unstructured meshes. *J. Comput. Phys.*, 305:589–603, 2016a.
- G. I. Park and P. Moin. Space-time characteristics of wall-pressure and wall shear-stress fluctuations in wall-modeled large eddy simulation. *Phys. Rev. Fluids*, 1:024404, 2016b.
- N. Park and K. Mahesh. Reduction of the germano-identity error in the dynamic smagorinsky model. *Phys. Fluids*, 21:065106, 2009.
- V. C. Patel. Calibration of the preston tube and limitations on its use in pressure gradients. *J. Fluid Mech.*, 23:185–208, 1965.
- J. Patterson, R. Balin, and K. Jansen. Assessing and improving the accuracy of synthetic turbulence generation. *J. Fluid Mech.*, 906:R1, 2021.
- E. Perlman, R. Burns, Y. Li, , and C. Meneveau. Data exploration of turbulence simulations using a database cluster. *Proceedings of the 2007 ACM/IEEE Conference on Supercomputing*, SC07: 1–11, 2007.
- U. Piomelli and E. Balaras. Wall-layer models for large-eddy simulations. *Ann. Rev. Fluid Mech.*, 34:349–374, 2002.
- U. Piomelli, J. Ferziger, P. Moin, and J. Kim. New approximate boundary conditions for large eddy simulations of wall-bounded flows. *Phys. Fluids A*, 1:1061–1068, 1989.

- U. Piomelli, A. Rouhi, and B. J. Geurts. A grid-independent length scale for large-eddy simulations. *J. Fluid Mech.*, 766:499–527, 2015.
- T. J. Poinso and S. K. Lele. Boundary conditions for direct simulations of compressible viscous flows. *J. Comput. Phys.*, 101:104–129, 1992.
- S. B. Pope. *Turbulent flows*. Cambridge University Press, 2000.
- S. B. Pope. Ten questions concerning the large-eddy simulation of turbulent flows. *New J. Phys.*, 6:35, 2004.
- C. Rapp and M. Manhart. Flow over periodic hills: an experimental study. *Exp. Fluids*, 51:247–269, 2011.
- S. Rezaeiravesh, T. Mukha, and M. Liefvendahl. Systematic study of accuracy of wall-modeled large eddy simulation using uncertainty quantification techniques. *Comput. Fluids*, 185:34–58, 2019.
- C. L. Rumsey. The nasa juncture flow test as a model for effective cfd/experimental collaboration. *AIAA J.*, page 3319, 2018.
- R. Sandberg. Numerical investigation of turbulent supersonic axisymmetric wakes. *J. Fluid Mech.*, 702:488–520, 2012.
- P. Schlatter, Q. Li, G. Brethouwer, A. V. Johansson, and D. S. Henningson. Simulations of spatially evolving turbulent boundary layers up to $re_\theta = 4300$. *Int. J. Heat. Fluid. Fl.*, 31:251–261, 2010.
- U. Schumann. Subgrid scale model for finite difference simulations of turbulent flows in plane channels and annuli. *J. Comput. Phys.*, 18:376–404, 1975.
- W. R. Schwarz and P. Bradshaw. Turbulence structural changes for a three-dimensional turbulent boundary layer in a 30° bend. *J. Fluid Mech.*, 272:183–210, 1994.
- O. Sendstad. The near wall mechanics of three-dimensional turbulent boundary layers. *Tech. Rep. Thermo Sci. Div. Mech. Eng. Stanford University*, TF 57, 1992.
- J. A. Sillero, J. Jiménez, and R. D. Moser. Two-point statistics for turbulent boundary layers and channels at reynolds numbers up to $\delta^+ = 2000$. *Phys. Fluids*, 26(10):105109, 2014.
- J. Slotnick, A. Khodadoust, J. Alonso, D. Darmofal, W. Gropp, E. Lurie, and D. Mavriplis. Cfd vision 2030 study: a path to revolutionary computational aerosciences. *Tech. Rep.*, NASA:CR–2014–21817,, 2014.
- P. R. Spalart. Theoretical and numerical study of a three-dimensional turbulent boundary layer. *J. Fluid Mech.*, 205:319–340, 1989.

- H. B. Squire and K. G. Winter. The secondary flow in a cascade of airfoils in a nonuniform stream. *J. Aeronaut. Sci.*, 18:271, 1951.
- Y. Tamaki and S. Kawai. Wall-modeled les of transonic buffet over nasa-crm using cartesian-grid-based flow solver ffvhc-ace. *AIAA SciTech*, pages 2023–0429, 2023.
- S. Toosi and J. Larsson. The germano identity error and the residual of the les governing equation. *J. Comput. Phys.*, 443:110544, 2021.
- A. W. Vreman. An eddy-viscosity subgrid-scale model for turbulent shear flow: Algebraic theory and applications. *Phys. Fluids*, 16:3670, 2004.
- L. Wang, R. Hu, and X. Zheng. A comparative study on the large-scale-resolving capability of wall-modeled large-eddy simulation. *Phys. Fluids*, 32:035102, 2020.
- M. Wang and P. Moin. Dynamic wall modeling for large-eddy simulation of complex turbulent flows. *Phys. Fluids*, 14:2043, 2002.
- M. P. Whitmore, K. P. Griffin, S. T. Bose, and P. Moin. Large-eddy simulation of a gaussian bump with slip-wall boundary conditions. *Annual Research Briefs in Center for Turbulence Research*, Stanford University, pages 45–58, 2021.
- H. H. A. Xu, A. Towne, X. I. A. Yang, and I. Marusic. Pressure power spectrum in high-reynolds number wall-bounded flows. *Int J Heat Fluid Flow*, 84:108620, 2020.
- X. I. Yang and K. P. Griffin. Grid-point and time-step requirements for direct numerical simulation and large-eddy simulation. *Phys. Fluids*, 33:015108, 2021.
- X. I. A. Yang and S. T. Bose. A physical basis of the slip-wall model for wall- modeled large-eddy simulations. *In 10th International Symposium on Turbulence and Shear Flow Phenomena*, 2017.
- X. I. A. Yang, J. Sadique, R. Mittal, and C. Meneveau. Integral wall model for large eddy simulations of wall-bounded turbulent flows. *Phys. Fluids*, 27:025112, 2015.
- X. I. A. Yang, G. I. Park, and P. Moin. Log-layer mismatch and modeling of the fluctuating wall stress in wall-modeled large-eddy simulations. *Phys. Rev. Fluids*, 2:104601, 2017.